Petrology and metamorphic evolution of the ultramafic rocks in the Eoarchean Isua supracrustal belt: Implications to Archean geodynamics

Dissertation

Petrology and metamorphic evolution of the ultramafic rocks in the Eoarchean Isua supracrustal belt: Implications to Archean geodynamics

Graduate School of
Natural Science & Technology
Kanazawa University

Division of Natural System

Student ID: 1724062014
Name: Juan Miguel Ramirez GUOTANA
Chief Supervisor: Prof. Tomoaki Morishita

June 2020

TABLE OF CONTENTS

LIST OF FIGURES AND TABLES

ABSTRACT

The Archean Eon marks the onset of the cooling of the Earth. It was during the Archean Eon that crust started strengthening of the crust, ocean formed, transition to plate tectonics and emergence of life. The early Earth associated mantle and lithosphere still remain enigmatic due to limited preserved intact geological records. Contemporary plate tectonics could not have operated in the past due to the higher mantle temperature. It has been challenging to discover the most intact pieces of the early Earth preserved today for geodynamic reconstructions. Precambrian rocks some of which are dated as Archean are exposed in Greenland and form part of the North Atlantic Craton (NAC). The main exposure of the NAC is along the SW portion of Greenland which consists of Eo- to Neoarchean orthogneiss which includes the Eoarchean Itsaq gneiss complex. The Isua supracrustal belt (ISB), located within the Itsaq gneiss complex, is a fragment of sedimentary and volcanic succession intruded by tonalities and granites. Ultramafic rocks occur as discontinuous enclaves within the supracrustal assemblage. The affinity of the ultramafic rocks is still unclear. The ultramafic bodies in the western limb of ISB (Lens A and Lens B) that were interpreted to have lesser effects of metamorphism and deformation are the focus of this study. In Lens B, Ti-rich humite-type minerals ($nM_2SiO_4 \cdot M_{1-x}(OH,F)_{2-2x}Ti_xO_{2x}$) such as titanian chondrodite (Ti-Chn) and titanian clinohumite (Ti-Chu) occur as accessory phases in these ultramafic rock bodies forming patches within olivine. The host olivine contains abundant magnetite inclusions. The high forsterite content (Fo=96-98) and variable MnO and NiO of the host olivine indicate a metamorphic origin as a result of deserpentinization rather than primary igneous features. Recent experimental works suggest a 2.6 GPa pressure stability condition for Ti-Chn co-existing with olivine. The intergrowth relationship between Ti-Chn and Ti-Chu formed as a result of breakdown during decompression. The discrete Ti-Chu grains suggest a retrograde path from high-pressure (2.6 GPa) to lower pressure (1 GPa) within the antigorite stability field (630-660°C). The overall petrological and geochemical features of the 3.8-3.7 Ga ISB Lens B ultramafic rocks reached eclogite facies conditions following deserpentinization. The exact timing of the high-pressure metamorphic event is not clear. However, the high-pressure metamorphic imprints are not reflected in the surrounding amphibolites. It suggests that the high pressure metamorphism occurred younger than the previously established metamorphic events (3.74 and 2.87 Ga) characterized by temperatures above 610°C, 480 to 550°C and a minimum pressure of 6 kbar due to the presence of kayanite in the domain where the ultramafic lenses are exposed.

The southern Lens A (south of Lens B) exhibits contrasting textural and geochemical signatures (Fo=89-92 and less varying MnO and NiO contents) suggesting weaker metamorphic imprints. The formation of spinel-clinopyroxene symplectites in olivine in Lens A can be explained by subsolidus elemental diffusion form host olivine or by dehydrogenation-oxidation of hydrous olivine and possibly humite layers in olivine.

The Eoarchean Lens B metadunites exhibit features suggestive of HP metamorphism followed by retrograde metamorphism, which are petrological features that can be explained by deep burial followed by rapid exhumation, comparable to modern subduction zone channels, though the extent of actual subduction remains enigmatic. On the contrary, Lens A shows minimal metamorphic imprints and more igneous features. Studies on primary igneous features of ultramafic rocks can be more focused on Lens A. The contrast observed between the two lenses difference in composition and texture compared to Lens B suggesting difference in the P-T path or exhumation history.

1. INTRODUCTION

1.1.The Early Earth: Geodynamics and Archean geologic records

The Earth started cooling during the Archean Eon (4.6 Billion to 2.5 Million years ago) which lead to the strengthening of the crust, formation of oceans, plate tectonics and emergence of life (Wilde et al., 2001; Smithies et al., 2003; Dilek and Furnes, 2013; Noffke et al., 2013). The early Earth associated mantle and lithosphere still remain cryptic due to the paucity of intact geologic records that are free from deformation and chemical modification. Modern-style plate tectonics could not have operated in the past due to the higher mantle temperature (Hadean-Archean: ~200-250°C; Archean-Proterozoic: ~100-200°C) (Nisbet and Fowler, 1983; Abbott et al., 1994; Sizova et al., 2010). Early Earth geodynamics is characterized by "squishy lid" tectonics (Hadean-Archean) and a transition phase (Archean to Proterozoic) before modern-style plate tectonics (Gerya, 2019). The challenge lies in discovering and validating the oldest geologic clues to reconstruct the early Earth geodynamics. In searching for such clues, certain areas in the world preserve the oldest geologic records and have been the subject of interest (Fig. 1).

The mantle during the Hadean-Archean eon (ca. 3 Ga) was about 200-250°C higher than present-day temperature. The lithosphere was mainly formed by tectonomagmatic differentiation (Sizova et al., 2010). Unstable portions of the crust are removed by eclogite dripping and delamination. Recycling of lithosphere is mainly driven by plume- and impact-induced delamination/subduction (Gerya et al., 2015). The period from Hadean-Archean is characterized by a period of crust and lithosphere growth followed by a removal phase due to the weak nature of the lithosphere and high mantle temperature (squishy-lid tectonics) (Gerya, 2019). Transitional tectonics is proposed to have occurred during the Archean-Proterozoic (3Ga-1Ga) wherein squishy-lid tectonics evolved developed towards plate-tectonic-like. The mantle is still hotter (100-200°C) than present-day and plume-induced subduction was most likely common (Fischer and Gerya, 2016). Modern-style plate tectonics operated at ca. 1-0.5 Ga as a result of the cooling mantle, mosaic of rigid plates, the rise of continents and increased erosion that provided lubrication along trenches for subduction (Sobolev and Brown, 2019).

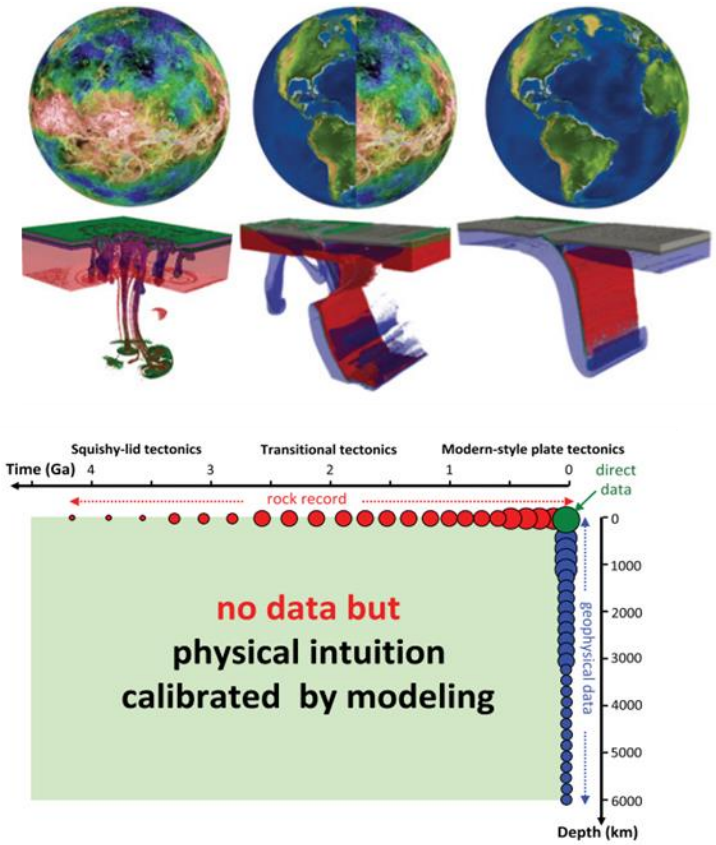

Figure 1. The evolution of geodynamic models of the Earth (top) and a graph showing the depth and age relationship of available data in constraining the models (adopted from Gerya, 2019).

1.2. Archean subduction fingerprinting

Plate tectonics is the horizontal movement of the stabilized lithospheric plates over a convecting mantle towards subduction zones wherein it sinks back to the mantle (Wilson, 1965; Cox, 1986; Stern, 2007). Subduction provides force in driving plate tectonics from the gravitational pull of the dense slabs (Forsyth and Uyeda, 1975). The formation of continental crust and recycling crustal materials to the mantle is attributed to subduction which contributes to the compositional structure of the Earth (Hawkesworth et al., 1993; Davidson and Arculus, 2006; Rupke et al., 2004; Herman and Spandler, 2008).

The onset of plate tectonics has been the focus of several studies. Plate tectonics and subduction zone processes documented in the oldest rock records from the Archean are interpreted based on the features related to modern analogs (Stern, 2007). Subduction zone markers can be classified into geochemical, metamorphic and structural markers. Geochemical markers are from igneous rocks with arc signature (e.g. Miyashiro, 1974;

Tatsumi, 2005). The presence of high-pressure metamorphic rocks such as blueschist to eclogite facies rocks and paired metamorphic belt are considered as metamorphic subduction zone markers (Dewey and Bird, 1970; Miyashiro, 1972). The structural marker includes accretionary wedges and associated thrust planes (Coney et al., 1980). These features are recognized from Archean records; however, there is still an ongoing discussion on how to interpret such features.

In looking for subduction clues, preserved Archean cratons and shields have been explored. The oldest known Earth materials are minerals which were the basis of the isotopic age delineating the Archean Eon. Zircon grains which yielded isotopic age of 4.2-4.4 Ga (Jack Hills zircons) were found in sedimentary rocks in Western Australia (Harrison et al., 2005). The oldest known rock on Earth is the volcanic deposits metamorphosed to amphibolite facies that forms part of the Nuvvuagittuq greenstone belt in Quebec, Canada (4.28 billion-year-old) (O'Neil et al., 2008). The Acasta gneiss in northwestern Canada preserves a single relict zircon grain yielding 4.0 Ga age and the second oldest (Bowring et al., 1989). Greenland also preserves a 3.85 Ga volcanic-sedimentary lithologic package interpreted to be an ancient accretionary wedge (Nutman et al., 1996a).

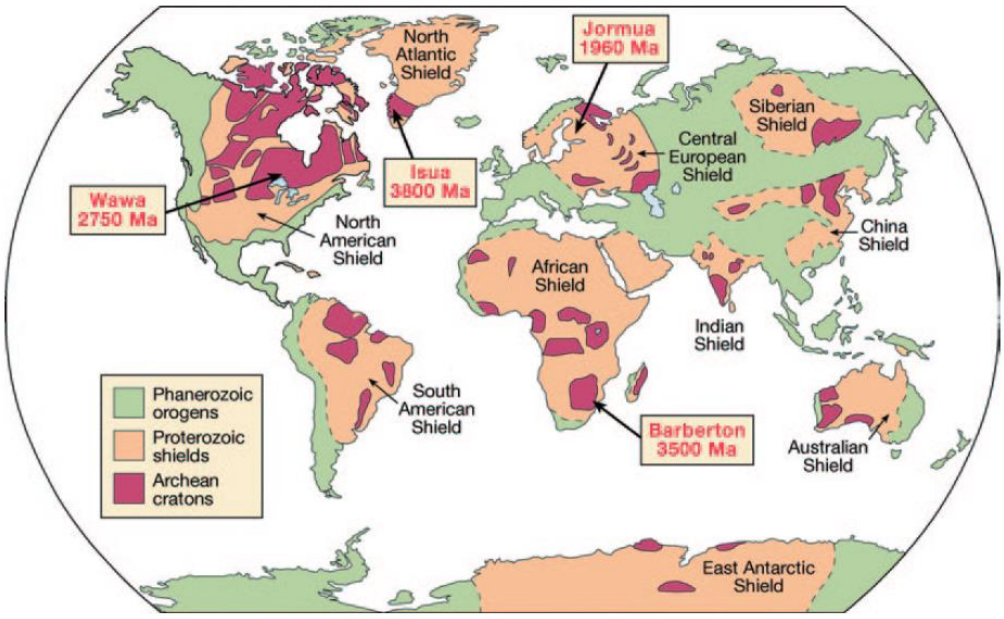

Figure 2. Global map showing the distribution of Precambrian shields and cratons (map adopted from Marshak, 2005).

1.3. Ultramafic rocks in Isua Supracrustal Belt

Archean crust (exposed and buried) constitutes an area of about 15,476,000 km^2 which is about 15% of the preserved Precambrian crust (Goodwin, 1991) (Fig. 2). A complex and multiple suturing events built the Archean and Proterozoic cratons forming a continental lithosphere in Canada, Greenland and NW Europe (Balling, 2000). Precambrian rocks some of which are dated as Archean are exposed in Greenland and form part of the North Atlantic Craton (NAC). The main exposure of the NAC is along the SW portion of Greenland which consists of Eo- to Neoarchean orthogneiss which includes the Eoarchean Itsaq Gneiss complex (Nutman et al., 1996a). The Itsaq gneiss complex forms part of the Akulleq Terrane (3880–3660 Ma) in southern West Greenland. The Akia Terrane (3230–2980 Ma) and the Tasiusarsuaq (2920–2830 Ma) bound the Akulleq Terrane from north to south (Mcgregor et al., 1991; Nutman et al., 1996a). The Eoarchean Isua supracrustal belt is composed of igneous and sedimentary lithologic packages that are interpreted to have retained low strain and low alteration zones that are primary features (see summary in Nutman et al., 1996b, 2020; Complex et al., 1999) despite polyphase metamorphism and deformation (Boak and Dymek, 1982; Rose et al., 1996).

The Isua supracrustal belt (ISB) is a 35-km arcuate belt located within the Eoarchean terranes which are composed of 3.9-3.6 Ga Amitsoq gneiss and 2.8 Ga Ikkattoq gneiss. In some areas, low-strain and alteration-free pillow lavas are exposed suggesting that original lithological relationship and chemical features can still be observed in the ISB (Appel et al., 1998). Several trains of discontinuous ultramafic bodies are exposed within the ISB and the origin of these ultramafic rocks is still enigmatic with varying interpretations. The ISB ultramafic rocks have been interpreted as metamorphosed olivine+pyroxene protoliths from the mantle (Friend and Nutman, 2011), cumulates (Szilas et al., 2015) or layered intrusion (Rollinson, 2007). The ultramafic bodies that show the least deformation and chemical modification are exposed in the eastern portion of the western limb of the ISB. These bodies are referred to as Lens A and Lens B (Fig. 3) by Friend and Nutman (2011). The exact origin of the ultramafic bodies has been interpreted in various ways.

Almost all of the lithologies in the ISB are affected by pervasive metasomatism which heavily imprinted the protoliths (Rosing, 1989; Rose et al., 1996). In this study, detailed examination of the metamorphic features and P-T paths of these rocks are investigated which could provide clues on its origin.

1.4. Metamorphism in ISB

Several metamorphic studies done in ISB focused on the surrounding metabasites and metapelites (Boak and Dymek, 1982; Komiya et al., 2002). The detailed study of the garnet morphology and composition suggest several growth generations. The eastern part of the western limb of the ISB falls under Domain IV. Several domains in the ISB (Domains II-V) record two garnet growths which correspond to metamorphic events (average age 3.74 Ga). Two domains (Domain II and IV) record a younger garnet growth. The younger garnet is linked to the 2.8 Ga metamorphic event (Gruau et al., 1996; Frei et al., 1999) which is both recorded in Domains III and IV also. Garnet-biotite pairs suggest that temperature conditions of above 610°C for the early metamorphic event (3.74 Ga) and a lower temperature range (550-570°C) for the younger metamorphic event (2.8 Ga). The pressure for the earlier metamorphism is constrained by the presence of kyanite in the sample which is around 6 kbar (Rollinson, 2002b).

Metamorphosed ultramafic rocks were reported and described by Dymek et al. (1988) from the southern train of the western limb of ISB. This study focuses on the metamorphic features and history of the ultramafic bodies (Lens A and B) on the northeastern portion of the western ISB.

Low-grade metamorphism of ultramafic rocks is typically dominated by serpentine minerals: lizardite, chrysotile and antigorite. Serpentine minerals replace olivine and pyroxene in the ultramafic rocks. The breakdown of serpentine at higher temperatures is marked by the appearance of secondary olivine, pyroxene and amphibole (Spear, 1993). The prograde assemblage is recognized by slight textural and compositional differences from the primary assemblage. Spinel, though regarded as resistant, also record metamorphism at various metamorphic grade (Barnes and Roeder, 2001). The dehydration of serpentine is also referred to as deserpentinization. Fluids released during deserpentinization also enhance the metamorphic reaction. Ultramafic rocks in the MgO-SiO_2-H_2O system have limited thermobarometric indicators. Accessory phases such as titanium-rich humite group of minerals have been recently described in detail in terms of PT stability (Shen et al., 2015). In the absence of garnet, such phases are very useful in reconstructing the PT history of ultramafic rocks.

1.5. Motivation and objectives

The origin of the ultramafic rocks in ISB has been a controversial topic on petrological studies in the ISB. This study focuses on the petrological and chemical features of the ultramafic rocks in ISB emphasizing on the metamorphism recorded by these rocks. Unraveling the metamorphic imprints will give clues on the possible magmatic features that will help resolve the origin of the IBS ultramafic rocks. This study specifically aims to:

- Characterize the ultramafic bodies in the western ISB
- Compare the petrologic and chemical composition of these ultramafic bodies
- Investigate the effects of deserpentinization
- Reconstruct the metamorphic PT path of the ISB ultramafic rocks
- Elucidate its implications in Archean metamorphism and tectonics

2. GEOLOGY

2.1. Geologic Setting

The Isua supracrustal (ISB) belt is a 35-km arcuate belt located within the Akulleq terrane which is composed of 3.88–3.66 Ga Amitsoq gneiss and 2.82 Ga Ikkattoq gneiss. The Isua supracrustal belt is subdivided into two terranes, an older 3.8Ga southern terrane and a younger 3.7 Ga northern terrane (Fig. 3). The two terranes are separated by a tectonic divide made up of felsic schist with zircon age of 3.94-3.74 Ga (Nutman and Friend, 2009). The terranes were assembled before 3660 Ma marked by the intrusion of the Inaluk dikes (Nutman and Friend, 2009). The ISB preserves one of the oldest submarine igneous sequences in the world. The ISB and surrounding supracrustal rocks (Akilia association) are intruded by the Amitsoq gneiss which forms part of the Itsaq gneiss complex (McGregor and Mason, 1977; Baadsgaard et al., 1984; Nutman et al., 1984; Harland et al., 1990). Some rocks in the Isua supracrustal belt preserve primary features which include basaltic extrusive and hypabyssal rocks associated with banded iron formation (BIF), chemical and clastic sediments. Well preserved sheeted dikes intruding the amphibolite+ultramafic rocks in the western limb of the ISB was reported by (Furnes et al., 2007). The ultramafic rocks in ISB can be generally classified into metadunite and metaperidotites and could be mantle residues, sills or cumulates. However, the exact affinity is still unclear. Felsic rocks are mainly granitoid intrusions but also include detrital sediments and volcaniclastic flows that are petrographically and geochemically similar to the surrounding Amitsoq gneiss. The Amitsoq gneiss also occurs as tectonically intercalated sheets with other supracrustal rocks in ISB (Furnes et al., 2009).

The ISB can also be subdivided into two units: 1) Undifferentiated amphibolites (UA) and 2) Garbenschiefer amphibolites (GA). The undifferentiated amphibolites preserve associated lithologies and structures that resemble an ophiolitic suite such as pillow lava, subparallel dikes, plagiogranite, gabbro and ultramafic rocks (Maruyama, 1991; Komiya et al., 1999; Furnes et al., 2007; Nutman et al., 2009). The Garbenschiefer amphibolites are mostly amphibole-garnet-biotite-chlorite schists with protoliths including volcanic and sedimentary rocks (Frei et al., 1999; Furnes et al., 2007). The geochemical signature of UA is comparable to igneous rocks with mid-ocean ridge basalt (MORB)-like composition with weak subduction imprint (elevated Th/Yb and Nb anomalies). The GA exhibits major and

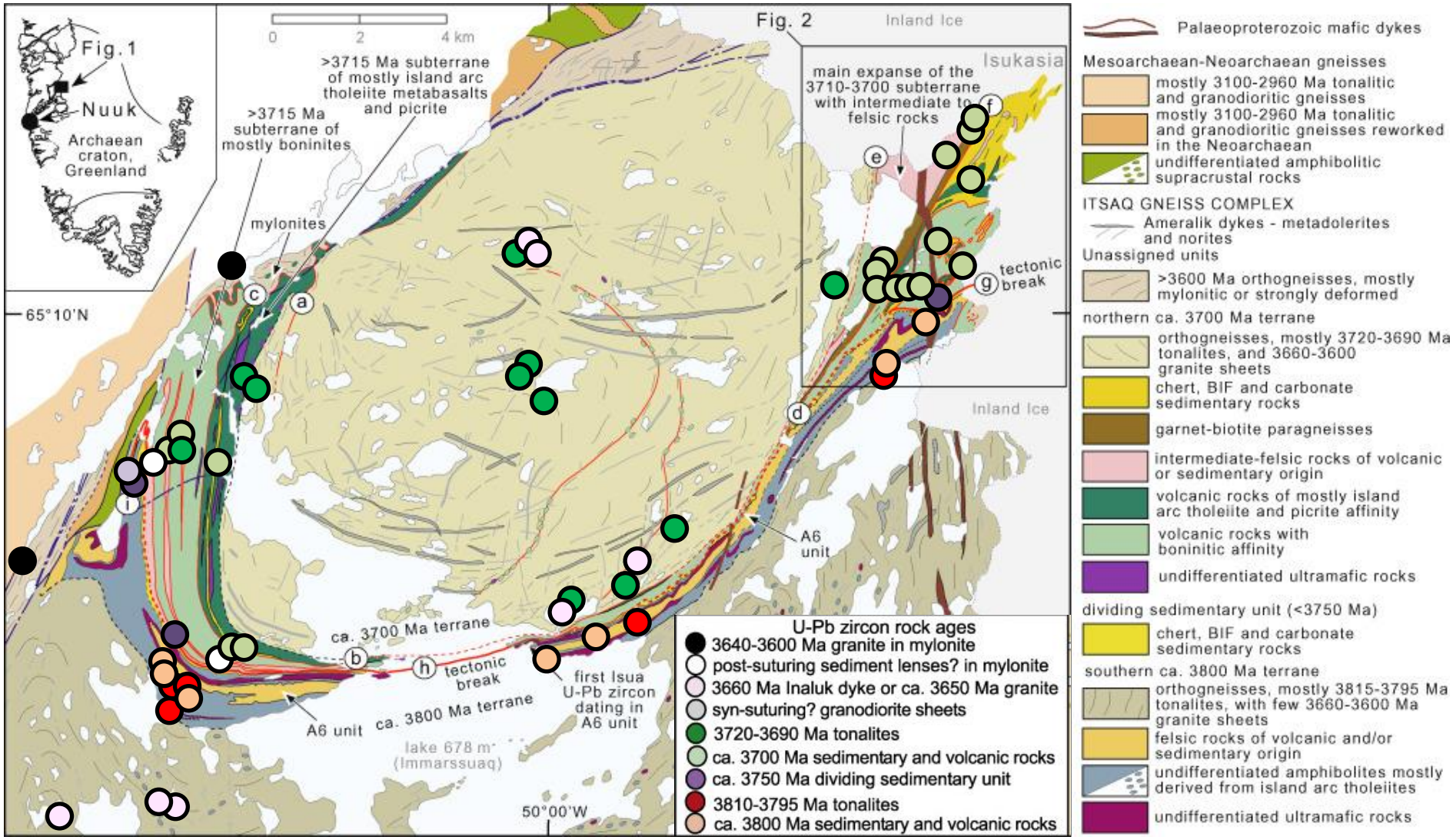

Figure 3. Generalized geologic map of the Isua supracrustal belt and surrounding Itsaq gneiss complex (map modified from Nutman and Friend, 2009).

trace-element composition similar to boninitic to island-arc tholeiite (IAT) magmatic rocks of SSZ-type ophiolites (Polat et al., 2002; Furnes et al., 2007).

2.3. ISB ultramafic rocks

Ultramafic rocks are exposed both in the eastern and western parts of the ISB. Most of the studies on the ultramafic rocks in ISB focused on the western limb in low-strain areas. The ISB ultramafic rocks have been interpreted as metamorphosed olivine+pyroxene protoliths from cumulates or sills mostly based on the ca. 3.80 Ga package of the western limb. In the southern portion of the western limb, olivine grains (Fo_{85-97}) are commonly intergrown with titanian clinohumite (Ti-Chu) and titanian chondrodite (Ti-Chn) (Dymek et al., 1988).

In the northeastern part of the western ISB limb, several ultramafic bodies that exhibit the least effects of chemical modification and deformation are exposed. These ultramafic bodies are referred to as Lens A and B (Friend and Nutman, 2011) (Fig. 4). The dunitic lenses are hosted within deformed, hydrated, carbonated ultramafic schists with fabrics comparable to the surrounding amphibolites (Friend and Nutman, 2011). The more intact dunite cores preserve structures that are oblique to the surrounding schists and mafic rocks. Lens A is the southern ultramafic body consists mainly of olivine (Fo_{91-92}), serpentine, chlorite and spinel. Lens B, in the northern part, has more complex assemblage with reported primary orthopyroxenes, secondary chlorite and humite group of minerals intergrown with olivine (Fo_{96-98}).

The origin of these ultramafic rocks has been the focus of previous studies (Rollinson, 2007; Friend and Nutman, 2011; Szilas et al., 2015; Kaczmarek et al., 2016). It was proposed that these are subarc mantle residues that are associated which are directly linked with the formation of the surrounding arc rocks. The HFSE depletion in the surrounding arc rocks is ascribed to the humite group of minerals HFSE enrichment (Friend and Nutman, 2011). B-type olivine fabric is also present in the ultramafic samples which are linked to mantle and suprasubdcution mantle wedge setting wherein such fabric can be found (Kaczmarek et al., 2016). The geochemistry and platinum-group of element composition of the ultramafic rocks show a correlation with the surrounding rocks and are akin to cumulate ultramafic rocks. These ultramafic rocks are also interpreted as cumulate equivalents of the surrounding boninites and basaltic rocks (Szilas et al., 2015). Spinel chemistry from some ultramafic samples is also comparable to the layered intrusion in the south of ISB (Rollinson, 2007).

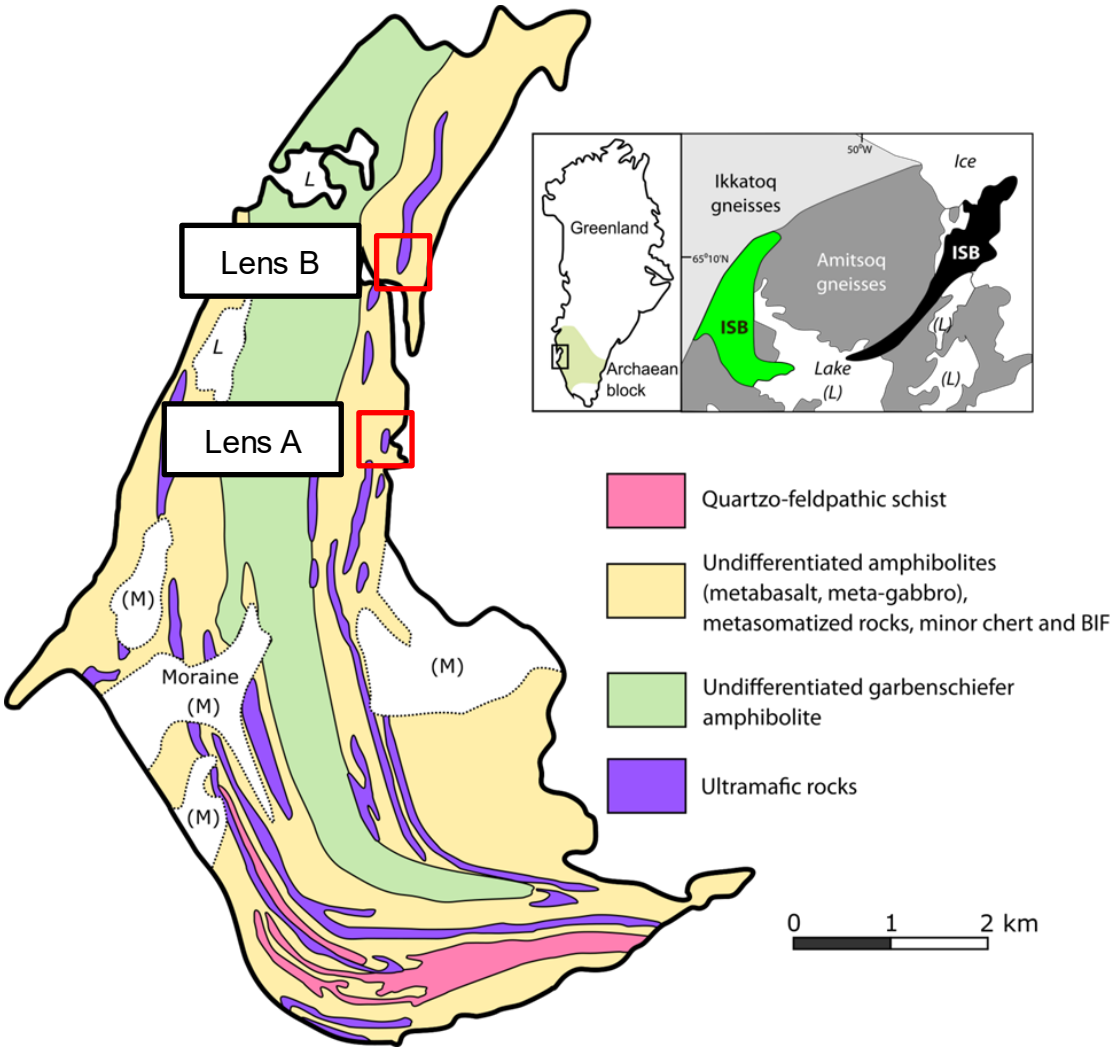

Figure 4. Detailed map of the western limb of the ISB showing the ultramafic lenses and surrounding metamorphosed mafic rocks modified from Friend and Nutman, 2011; Szilas et al., 2015.

2.4. Sample Locality

The samples in this study were collected in the northwestern limb of the ISB (Fig. 4), from the dunitic Lens B described by Friend and Nutman (2011). This ca. 130 x 680m dunite body exhibits varying degrees of serpentinization and is rimmed by talc-carbonate schist. The samples of this study will be referred to as metadunites hereafter due to the metamorphic origin of these rocks, which will be discussed in the following sections. Further south, Ti-Chn and Ti-Chu-bearing metadunite has also been reported, sharing general similar characteristics with the samples from and Lens B (Dymek et al., 1988).

3. ANALYTICAL METHODS

3.1. Petrography

Thin sections of representative samples from ISB Lens A and Lens B were prepared. Rock slabs from the hand specimen were cut. Lapping and polishing of rock slabs was done using 200, 400, 800, 1000 and 3000 SiC powder grits and the finally with a 1 µm diamond polishing solution. A Nikon Eclipse LV100 Pol polarizing petrographic microscope was used in the detailed observation of the thin sections.

3.2. Electron Probe Microanalysis

The major-element compositions of mineral phases were obtained using a JEOL JXA-8800 electron probe microanalyzer (EPMA) at the Kanazawa University (Fig. 5). The analyses were carried out using operating conditions of 20 kV accelerating voltage, 20 nA beam current, and a 3 µm beam diameter. The X-ray peaks and backgrounds of elements were analyzed for 20 and 10 seconds, respectively; except for Ni (30 and 15 seconds) Natural and synthetic standards were used for the analysis and results were corrected using ZAF (Z=atomic number, A=absorption, F=characteristic fluorescence) correction method using JEOL JXA-8800 software. Summary of major element compositions are presented in Tables 1, 3-10.

Figure 5. Jeol-JXA 8800 Electron probe micronalayzer at Kanazawa University.

3.3. Laser-ablation ICP-MS

A Laser Ablation Inductively Coupled Plasma Mass Spectrometry (LA-ICP-MS) (Agilent 7500S equipped with MicroLas Geolas Q-plus laser system; Agilent Technologies, Santa Clara, CA, US) at the Kanazawa University was used to analyze the concentrations of rare earth element (REE) and trace element compositions of major and minor phases (Fig. 6). An ablating spot size of 50 μm in diameter at a repetition rate of 6 Hz was used in each analysis point. External reference material was NIST SRM 612 and data reduction was facilitated using ^{29}Si as the internal standard, using the SiO_2 content obtained by EPMA. Summary of trace element composition is presented in Table 2.

Figure 6. Laser-ablation ICP-MS (Agilent 7500S equipped with MicroLas Geolas Q-plus laser system) at Kanazawa University.

3.4. Raman spectroscopy

The serpentine minerals were identified using micro-Raman system (HORIBA Jobin Yvon, LabRam HR800) equipped with a 532 nm Nd:YAG laser (Showa Optronics Co., Ltd, J100GS-16) and an Olympus BX41 optical microscope at the Kanazawa University.

Figure 7. Raman spectrometer at Kanazawa University (HORIBA Jobin Yvon, LabRam HR800).

3.5. Whole-rock XRF

The whole-rock compositions of representative Lens A and B metadunites were determined at the National Museum of Nature and Science in Tsukuba, Japan. The weathered and altered portions of the samples were removed and rocks slabs were made from representative samples (5x5x1cm). The rock slabs were subjected to grinding (200 grit size) to remove metal contamination induced by rock saw blades. The samples were washed using deionized water during a sonic bath and dried inside an oven. Each sample was coarsely crushed using a plastic hammer over a granite slab while wrapped with a thick plastic and kim towel to avoid contamination. The crushed samples were washed with deionized water and finally with acetone before drying in an oven overnight. The dried crushed samples were finely crushed using an alumina mortar and pestle. The finely crushed samples were powdered with a rapid pulverizer multi-beads shocker. The loss on ignition (L.O.I) values were determination was carried out by igniting 0.4000$\pm$0.0004 g of powdered samples at 1025ºC for 4 hours. The difference with the weight prior and after ignition determines the L.O.I. Glass beads were prepared containing lithium tetraborate flux (10 to 1 sample dilution). Pressed pellets (4.0-5.0g) were prepared using a 12-ton force for trace element geochemistry. The major and trace element compositions were measured using an X-ray fluorescence spectrometer (RIGAKU ZSX Primus II) following a method described in (Sano et al., 2011).

4. DESERPENTINIZATION AND HIGH PRESSURE (ECLOGITE-FACIES) METAMORPHIC FEATURES IN ISB LENS B

Lens B belongs to the few ultramafic lenses in the northeastern part of western ISB which are interpreted to have retained primary magmatic features (Friend and Nutman, 2011; Kaczmarek et al., 2016). The core of the ultramafic body Lens B is characterized by weakly altered dunite with a highly serpentinized outer body (Fig. 8). Ultramafic schist envelopes the dunitic lens. Lens B contains titanian chondrodite (Ti-Chn) and titanian clinohumite (Ti-Chu) as accessory phases. In this chapter, the metamorphic imprints on Lens B are discussed. The occurrence of humite group of minerals and the textural and chemical features of other phases suggest that Lens B reached high-pressure metamorphic conditions and several hydration and dehydration events.

4.1. Metamorphism of ultramafic rocks

Ultramafic rocks (>90% mafic minerals) occur mostly in the mantle and have been continuously subjected to melting, metasomatism and recycling which subsequently diversifies its composition (Downes, 2020). Ultramafic rocks exposed or brought to the surface could have originated as mantle residues after partial melting, cumulates, komatiitic volcanics or its derivatives.

The emplacement of ultramafic rocks in the crust involves mineralogical modification and deformation. The metamorphism upon emplacement could either form *allofacial* or *isofacial* ultramafic rocks. Allofacial ultramafic rocks may preserve original structure and mineralogy and due to slow equilibration, it may not or only partly reflect assemblage of the same metamorphic grade with the surrounding rocks (ophiolite complexes). Isofacial ultramafic rocks record P-T histories similar to the crustal host lithologies and may preserve minimal relic phases or structures (Evans, 1977; Bucher and Frey, 2002).

4.1.1. Serpentinization

Serpentinization is a hydrothermal alteration of low silica ultramafic rocks at a relatively low-temperature condition ($\leq$500°C). Hydration of olivine and pyroxene forms serpentine$\pm$brucite$\pm$magnetite. The process of serpentinization takes effect in various geologic settings: ocean floor, mid-ocean ridges and subduction zones (Evans, 2010).

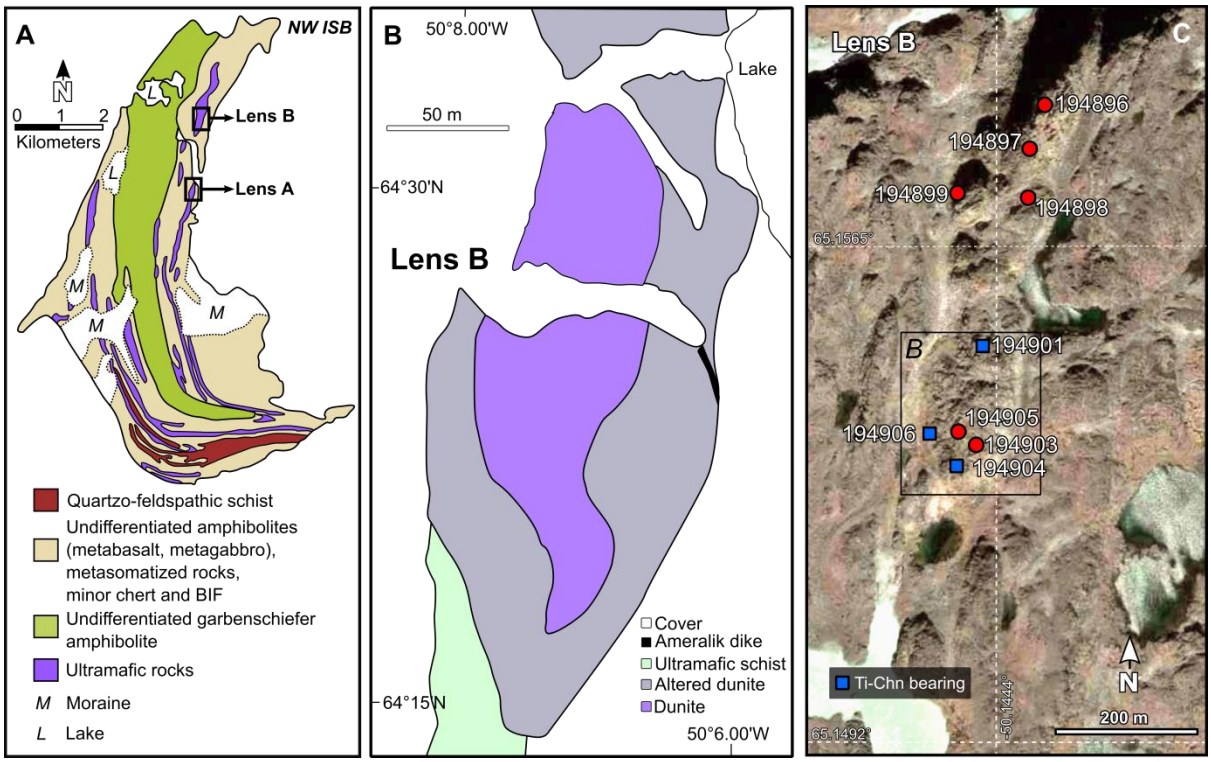

Figure 8. A) Map showing the location of Lens B in the western limb of the Isua supracrustal belt. B) Geologic map of Lens B from Friend and Nutman, 2011. C) Map showing the sampling locations in Lens B (Aerial image from Google Earth).

The hydration process of ultramafic rocks may uptake H_2O up to 13 wt. % (Ulmer and Trommsdorff, 1995).

Serpentinization is also responsible in introducing fluid mobile elements (FMEs) such as B, Sr and Cs Cs (Hattori and Guillot, 2003; Scambelluri et al., 2004). The stability of serpentine at higher pressure and depth (150 km) has been described by recent studies, thus, an important phase in transporting fluid and FMEs back to the mantle (Ulmer and Trommsdorff, 1995). Serpentine occurs in different types but more commonly as chrysotile, lizardite and antigorite. The identification of serpentine species is achieved by Raman spectroscopy or transmission electron microscopy but the minor chemical difference can also be observed. In the MHS system, serpentinization generally occurs in the following process:

$$2Mg_2SiO_4+3H_2O \rightarrow Mg_3Si_2O_5(OH)_4+Mg(OH)_2$$

(Forsterite) (Serpentine) (Brucite)

Serpentinization involves oxidation of iron, the formation of magnetite and the release of H^+. The formation of magnetite is more effective in the latter part of serpentinization and

relatively higher temperatures. At T~200°C, serpentinization produces Fe-rich brucite coupled with fewer magnetites. Samples serpentinized at temperatures between 200-300°C contain abundant magnetite. In both cases, H_2 is efficiently due to iron oxidation in serpentine (Klein et al., 2014). The release of H_2 is also an important part of serpentinization. The oxidation of Fe^{2+} to Fe^{3+} in olivine produces molecular hydrogen. The ferric iron is taken up by magnetite and other secondary silicate minerals such as serpentine, talc and tremolite (Evans, 2010). The formation of magnetite is more associated with the later stage of serpentinization after the breakdown of Fe-rich brucite (Bach et al., 2006).

Serpentine minerals have a general formula of $(Mg, Fe^{2+})_3Si_2O_5(OH)_4$. The stability field of serpentinites is generally challenging to evaluate due to the wide stability field (Evans, 2004). The three main serpentine types are lizardite, chrysotile and antigorite. Antigorite persists at higher-grade metamorphism and experimental works verify its stability at higher pressure conditions (Evans and Trommsdorff, 1978; Scambelluri et al., 1995; Padrón-Navarta et al., 2013; Debret et al., 2013b). Lizardite and chrysotile are more stable at lower grade metamorphism (Evans, 2004; Andréani et al., 2007). The assemblage antigorite+brucite is more stable than lizardite+chrysotile above 300°C during the transition from low- to high-grade metamorphism based on thermodynamic factors (Schwartz et al., 2013). In identifying specific serpentine varieties, transmission electron microscopy (TEM) and Raman spectroscopy are highly effective. The OH band obtained through Raman spectroscopy has been used to identify serpentine varieties.

There are several models in the stability fields of serpentine varieties (O'Hanley, 1996; Evans, 2004; Schwartz et al., 2013). The work of Schwartz et al., (2013) evaluated the PT stability of the serpentine bearing natural samples. The temperature stability is also constrained based on the surrounding/host metasediments which correlate to the serpentine varieties stable from low- to high temperature. The results of their work show that antigorite is absent at low-grade metamorphism in the sub-greenschist facies (P<0.4GPa, T- 200-300°C). The replacement of lizardite by antigorite occurs around 320°C starting from the lizardite grain boundaries and along with cores. The mesh-texture during replacement is typically preserved. Lizardite+antigorite are stable between 320-390°C (Fig.9). The addition of SiO_2 to lizardite and chrysotile also promotes antigorite stability (e.g. Evans, 2004).

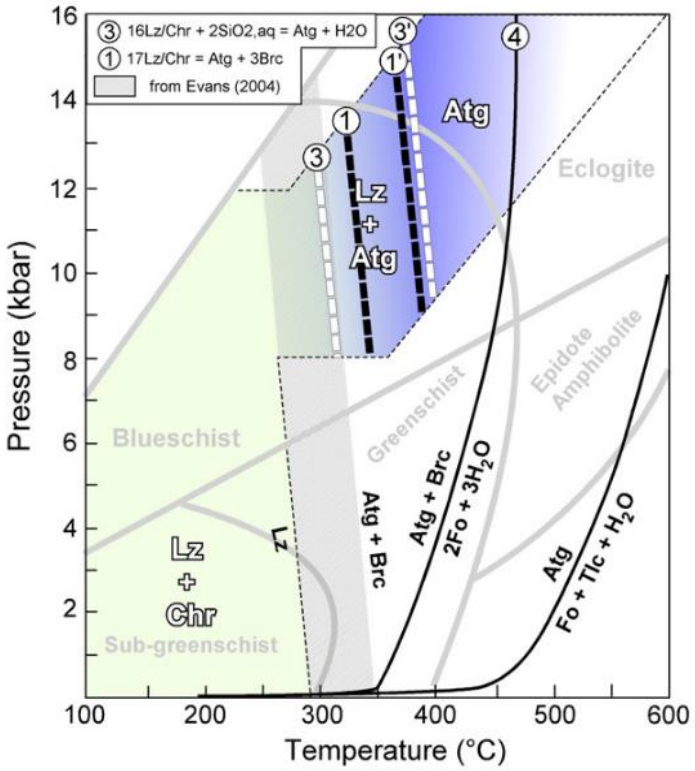

Figure 9. Phase diagram (after Schwartz et al., 2013) showing the stability fields of chrysotile, lizardite and antigorite (Evans, 2004). The univariant curve of serpentine dehydration is around 500°C.

4.1.2. Carbonation

CO_2 metasomatism of ultramafic rocks also forms carbonates and Fe-talc. The carbonation products are a function of the protolith composition, fluid CO_2 activity and temperature (Kelemen and Miller, 2004; Klein and McCollom, 2013). The CO_2 metasomatism of ultramafic rocks is associated with serpentinization. Experimental works of Klein and Garrido (2011) showed that mineral carbonation is more effective at low to moderate temperatures. In Ca-poor system, magnesite is the common carbonate phase formed and could be stable at higher temperatures. The source of fluids has been suggested to have an organic or magmatic origin while others also invoke a meteoric origin (Abu-Jaber and Kimberley, 1992; Kelemen and Matter, 2008). Aside from the Ca and Mg proportion in the metasomatising fluids, magnesite more commonly is the carbonate phase at temperatures between 400 to 500°C.

4.1.3. Deserpentinization

The formation of secondary or metamorphic olivine is associated with the dehydration-deserpentinization during serpentine breakdown at around 500°C (e.g. Arai, 1975; Vance and Dungan, 1977; Nozaka, 2005; Khedr and Arai, 2012; Plümper et al., 2012; Debret et al., 2013b). Petrographically, they may either occur as equigranular grain, veins or are sieved grains with inclusions (magnetite and/or sulfides). Olivine formed through such process has higher forsterite contents above 93, low-variable NiO and high MnO contents (Arai, 1975; Nozaka, 2003). Elements that are mobile under high fluid conditions such as B and Li also tend to be detectable in metamorphic olivine (McCaig et al., 2018). The abundance of opaque inclusions in olivine is an inherited feature from serpentinized protolith.

The prograde dehydration of serpentine has been described to have resulted from contact metamorphism (Trommsdorff and Evans, 1972; Arai, 1975; Vance and Dungan, 1977; Nozaka, 2005), Barrovian-type metamorphism (Evans, 1977) and subduction of serpentinized lithosphere (Hacker et al., 2003; Padrón-Navarta et al., 2011).

4.2. Humite-group of minerals as thermobarometric indicator

One challenge in studying metamorphism of ultramafic rocks in $MgO\text{-}SiO_2\text{-}H_2O$ system is the limited thermobarometric indicators. The titanian-rich variety of the humite group of minerals could be used in reconstructing the pressure-temperature path if garnet is absent in the samples.

Humite group of minerals has a general formula of $nM_2SiO_4 \cdot M_{1-x}(OH, F)_{2-2x}Ti_xO_{2x}$ (where M is occupied by divalent cations Mg, Fe, Mn, Ni, $x<1$, and $n = 1$ for norbergite, $n=2$ for chondrodite, $n=3$ for humite and $n=4$ for clinohumite). It forms a polysomatic series which is stoichiometrically collinear with olivine (Jones, 1969; Frost, 1975; Thompson, 1978; Fujino and Takeuchi, 1978; Ribbe, 1979; López Sánchez-Vizcaíno et al., 2005) Clinohumite and chondrodite varieties can accommodate a significant amount of Ti in the crystal structure. The titanian varieties of clinohumites and chondrodites occur as common accessory phases found in high-pressure and ultrahigh-pressure ultramafic rocks (Trommsdorff and Evans, 1980; Dymek et al., 1988; López Sánchez-Vizcaíno et al., 2005). Humites are also found in carbonates, however, they are F-rich and Ti-poor which is opposite to the composition observed in Isua humites. The OH partial substitution by F stabilizes humites at higher temperatures (Berman et al., 1986; Weiss, 1997; Aguinis et al., 2013). Several laboratory

experiments synthesized Ti-Chu and Ti-Chn at 29 and 77 kbar between 700 and 1200°C in the $MgO-SiO_2-H_2O$ system (Yamamoto and Akimoto, 1974) which is equivalent to about 70 and 120 km depth in the upper mantle (Aoki et al., 1976). In common subduction zone P-T paths, hydrous phases will break down and release water to the mantle wedge before the subducting slab reaches 600°C and 6 GPa (Kawamoto et al., 1996; Iwamori, 2004). In cold subducting slabs, the hydrous minerals can reach a greater depth which is different from warmer subducting slabs where these minerals break at lower pressure and loose water. Ti-Chu typically occurs as an accessory phase in ultramafic rocks. It is more likely found to be associated with antigoritic serpentinites (Möckel, 1969; Cimmino et al., 1979). Ti-Chu also varies as hydroxyl and fluorine rich types. Ti-Chn is less common than Ti-Chu.

4.3. Lens B sample description

Olivine porphyroblasts show two subdomains within grains: dusty and clear olivine. The dusty olivine is brownish and contains abundant opaque inclusions, mainly magnetite. The dusty olivine commonly occurs as cores of the prophyroblasts (Fig. 10 A-D). The clear olivines are devoid or contain a trace amount of opaque inclusions and envelopes the dusty olivine. The boundary between dusty and clear olivine is irregular.

Lizardite cuts both the dusty and clear olivine. Some lizardite veinlets contain abundant magnetite inclusion. Antigorite occurs as patches included within olivine, coarse blades around olivine porphyroblasts and as interlocking grains in the groundmass (Fig. 11 A-F). The coarse blades antigorite and groundmass antigorite are chemically similar while the inclusion antigorite has lower Al_2O_3 wt.% contents. Raman spectroscopy was used to confirm the serpentine species. In the Raman spectra, the coarse blades and interpenetrating serpentine in the groundmass show peaks that are typical of antigorite (229, 374, 1045, 3685 and 3709). The veins that cut the olivine show mostly lizardite peaks (690, 388, 3665, 3702) (Frezzotti et al., 2012; Petriglieri et al., 2015; González-Jiménez et al., 2017) (Fig. 14). Some veins cutting

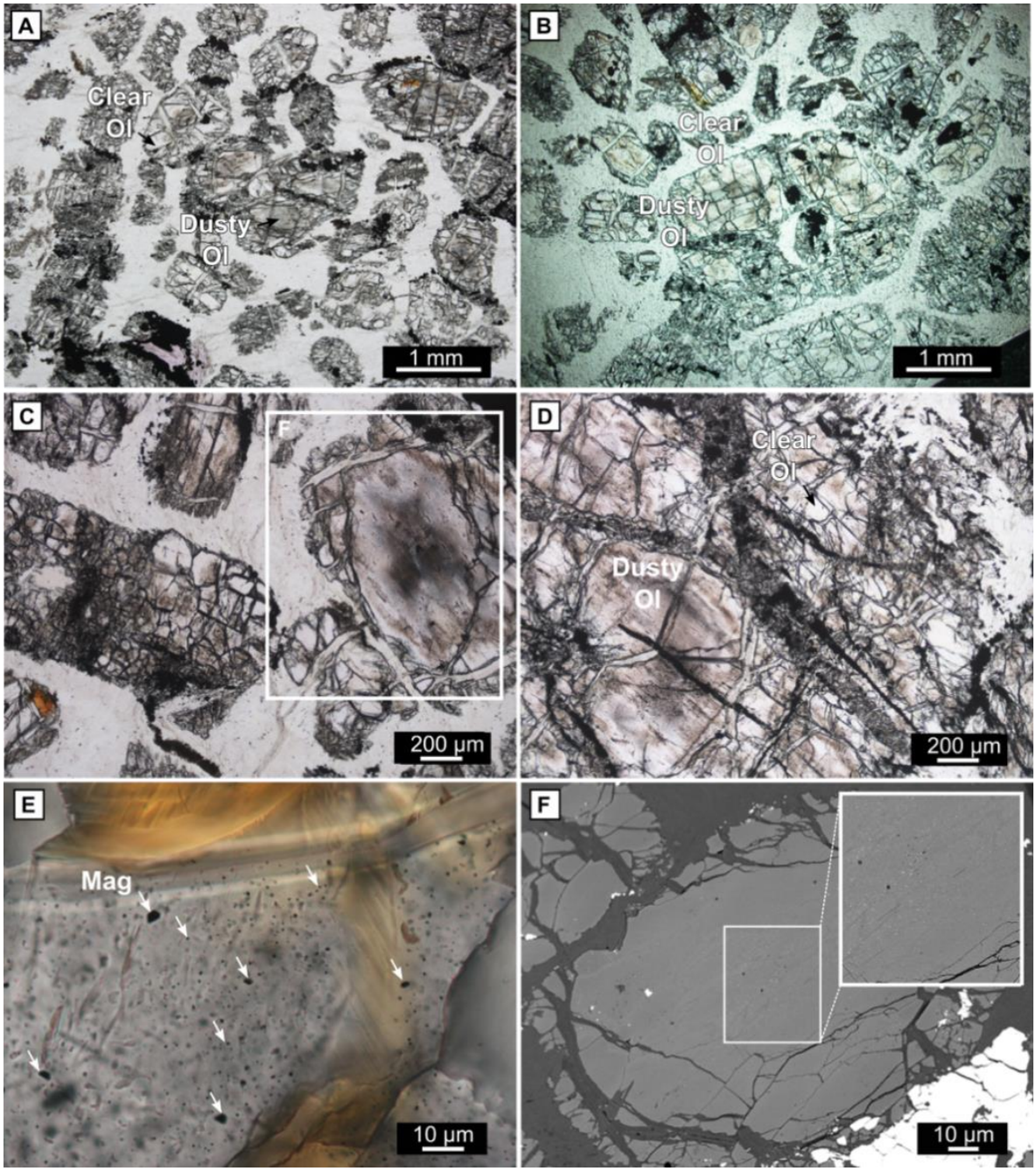

Figure 10. A-D) Olivine prophyroblasts in the ISB Lens B metadunites consist of a dusty olivine zone enveloped by clear olivine. E) The dusty olivine contains abundant opaque inclusions, mainly magnetite. F) Representative SEM image showing the dusty cores with abundant (bright spots) inclusions. The faint gray sinusoidal features correspond to cracks and subgrain boundaries in the dusty olivine.

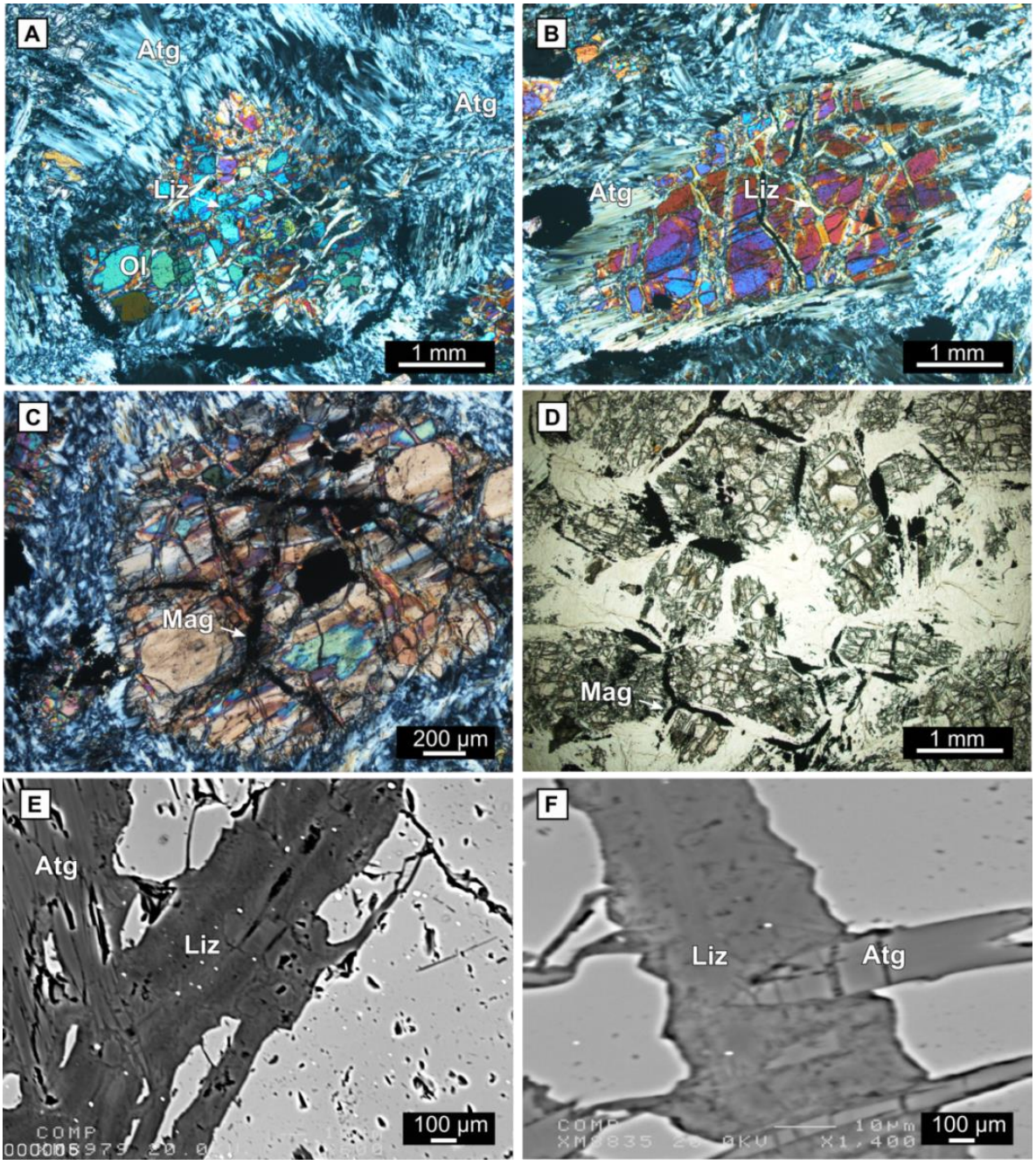

Figure 11. A-B) Antigorite occurs as coarse blades around olivine, interpenetrating groundmass and inclusion patches. C-D) Relic mesh boundaries are preserved by magnetite trails. E-F) Lizardite veins are cut by antigorite (coarse blades).

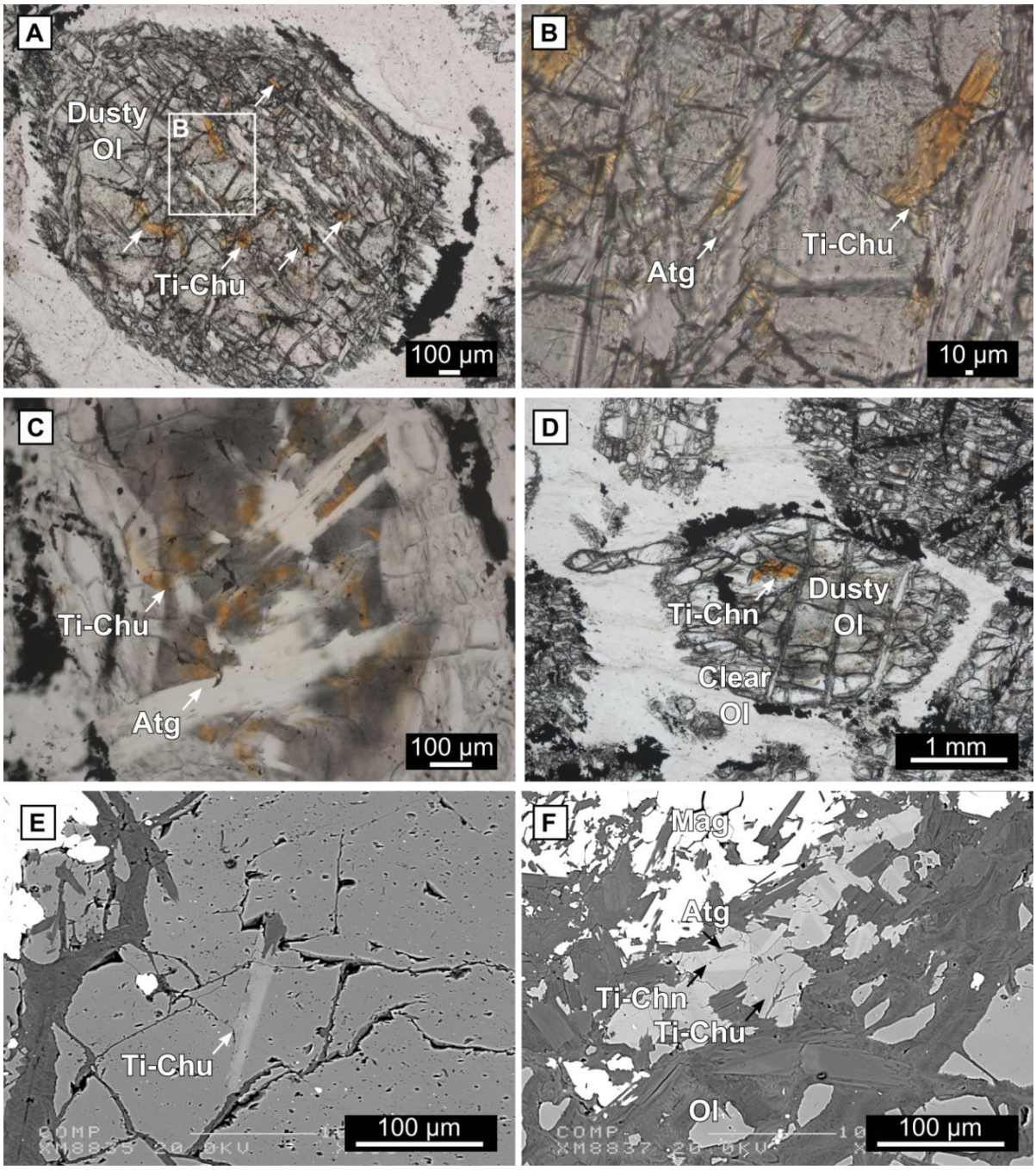

Figure 12. A-E) Representative photomicrographs of ISB Lens B humite group of minerals. Titanian clinohumite (Ti-Ch) and titanian chondrodite (Ti-Chn) are associated with dusty olivine and antigorite. F) Ti-Chu and Ti-Chn also occur as intergrown phases associated with olivine and antigorite.

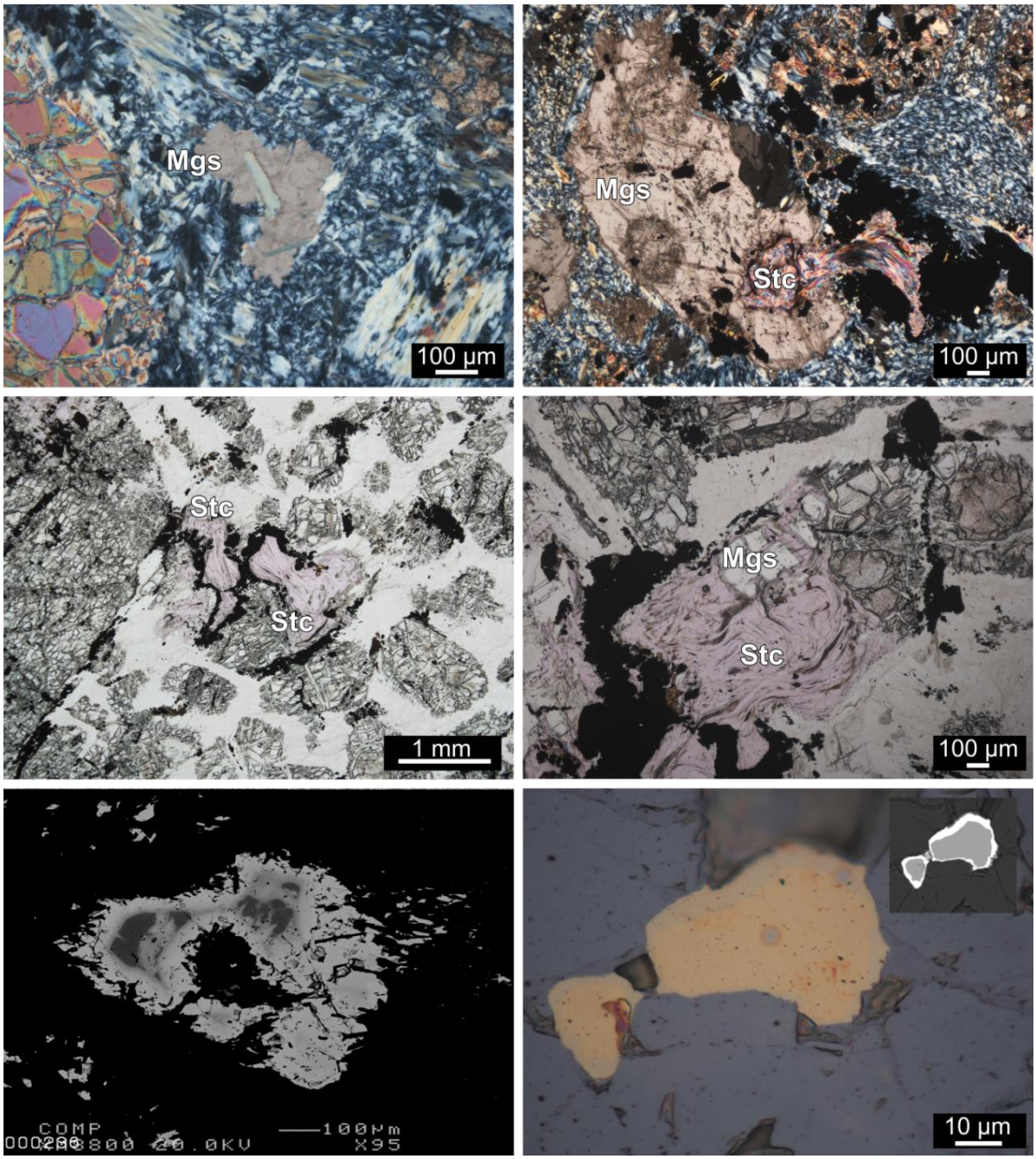

Figure 13. Representative photomicrographs and SEM images magnesite (Mgs), stichtite (Stc), relic spinel and Ni-rich sulfides.

the olivine show both antigorite and lizardite peaks. Brucite peak (441) was also observed in some lizardite veinlets. Some of the lizardite contains high concentrations of magnetite.

Titanian clinohumite (Ti-Chu) and titanian chondrodite (Ti-Chn) occur as accessory phases and are associated with the dusty olivine (Fig. 12 A-E). The humite-group of minerals is found as elongate grains in dusty olivine and antigorite. Ti-Chu and Ti-Chn show

intergrowth relationship in some portions. Relict chromite grains are heavily zoned with Cr-rich cores and feritchromite-magnetite rim. Magnesite replaces olivine and serpentine phases and preserves the original outline of the grain. Stichtites, Cr-hydrotalcites, replaces magnesite and are associated with spinel. Trace amounts of Ni-sulfides are also present (Fig. 13).

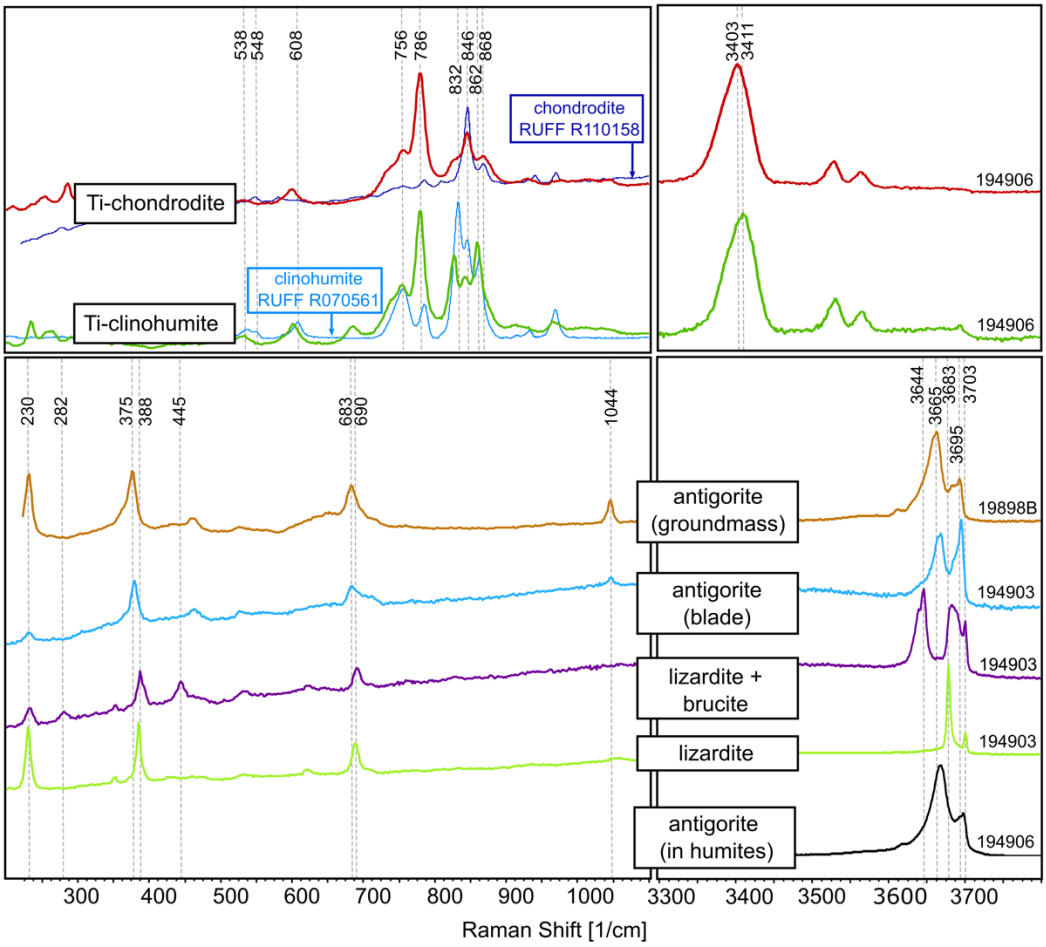

Figure 14. Raman spectra of humite-group minerals and serpentine in the ISB metadunites. Raman peaks from Frezzotti et al., 2012; Petriglieri et al., 2015; González-Jiménez et al., 2017. Raman spectra from RUFF database of chondrodite (R110158) and clinohumite (R070561) (Lafuente et al., 2016).

4.4. Results

4.4.1. Major-element mineral chemistry

Olivine is highly forsteritic (Fo=100*Mg/Mg+Fe^{2+}) ranging from 96-98. The clear olivine tends to be slightly more forsteritic than the dusty olivine. In terms of NiO and MnO contents, the dusty olivine (0.45-0.70, 0.18-0.59 wt. %) have higher values relative to the clear olivine (0.36-0.55, 0.08-0.25 wt. %) (Fig. 15). The CaO and Cr_2O_3 contents are

extremely low and below the detection limit. In some portions of the olivine, opaque inclusions are big enough to be analyzed the microprobe and were identified as magnetite (Table 1). The whole-rock Mg# (0.89-0.96) is lower than the olivine porphyroblasts (0.96-0.98) (Fig. 16).

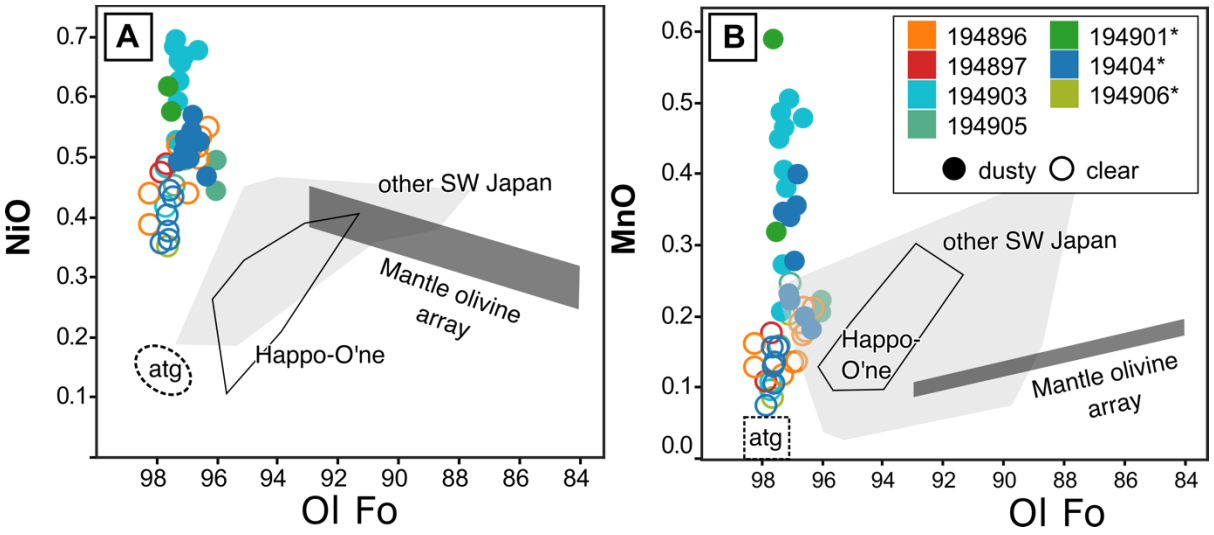

Figure 15. A-B) Olivine Mg# versus NiO wt% and MnO wt% of the ISB Lens B, metadunites fields from Happo-O'ne (Khedr and Arai, 2013) and other SW Japan metaperidotites (Ohsayama, Tari-Misaka and Yanomine) (Nozaka, 2003) are plotted for comparison.

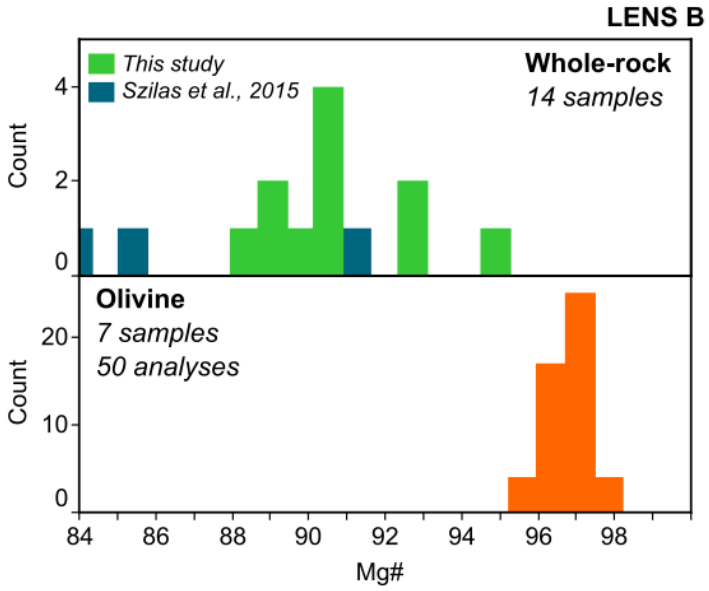

Figure 16. Histogram showing the comparison of whole-rock (This study and Szilas et al. 2015) and olivine Mg# of ISB-Lens B metadunites.

There is not much difference in the composition between the coarse antigorite blades around olivine porphyroblasts and those in the groundmass. The Al_2O_3 content of the blades (1.22-2.08 wt.%) is comparable to the groundmass (1.15-1.98 wt.%). However, the inclusion antigorite have much lower Al_2O_3 (0.17-0.52 wt.%). The Mg# of the antigorite range from 0.97-0.98. The Mg/Si is comparable among the antigorite types and ranges from 1.3-1.5. The NiO contents range from 0.13-0.32. The lizardite veinlets have lower Al_2O_3 contents, which are from below detection limit (b.d.l.) to 0.42 wt. %. The lizardite NiO contents range from 0.26-0.47 (Table 3-4).

The Lens B humite-group minerals are characterized by high TiO_2 contents (Ti-Chu=2.42-5.86 wt.%; Ti-Chn=7.72-9.22 wt.%; XTi=0.2-0.48) (Table 2). The XMg of the Ti-Chu and Ti-Chn are also very high similar to the host olivine, ranging from 0.97-0.98. The Lens B humite-group minerals are generally almost fluorine-free (Fig. 17 A-B) which is different from those occurring in the nearby Mesoarchean Ulamertoq peridotites (Nishio et al., 2019). In the XF versus XTi (a.f.u.), the Ti-Chu and Ti-Chn deviate away from the $TiO_2Mg_{-1}F_{-2}$ exchange vector (Fig. 17 A-B). There is also variation in the TiO_2 contents (TiO_2=2.4-3.4 wt.%) and a negative correlation with respect to the SiO_2 contents (SiO_2=38.5-36.8 wt.%).

Magnesite has MgO contents between 38.51-39.23 wt. % and FeO contents ranging from 0.62-1.56 wt. % (Table 7). Most of the spinels are magnetites, however, some grains preserve a Cr-rich core. The Cr# increase and Mg# decrease from core (0.74, 0.429) to rim (0.98, 0.26). The Fe^{3+} contents also increase from the core (0.15) to the rim (1.95) (Table 6).

4.4.2. Trace-element mineral chemistry

The chondrite-normalized rare earth element (REE) patterns show elevated heavy REE (HREE) relative to light- and middle- REEs. Negative Eu is present in the samples. The ISB olivines have higher LREEs relative to representative DMM olivine (Workman and Hart, 2005) and other mantle olivine represented by Gakkel Ridge harzburgites and lherzolites (Fig. 18). It is also interesting to note that the olivine show detectable amounts of B, Li and other FMEs (U, Pb, Sr, Cs and Ba) (Fig. 19).

In chondrite-normalized trace and rare-earth element diagrams, the humite-group minerals show enrichment in Ti, Nb, Ta, and Zr. The Isua Ti-Chu and Ti-Chn show elevated LREE and HREE patterns with distinctly low concentrations of MREE (Fig. 17C) (Table 5).

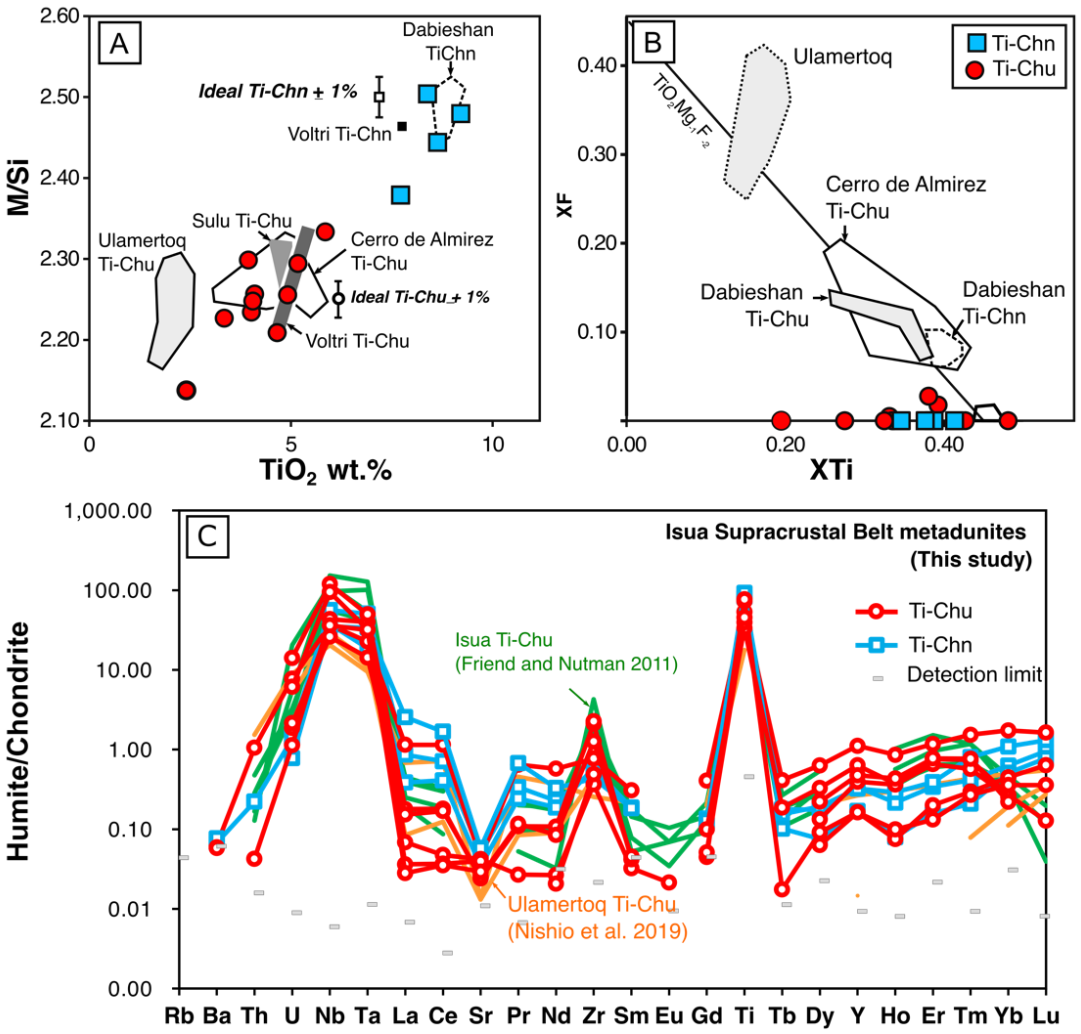

Figure 17. A-B) Major-element variation diagrams of humites in the ISB Lens B. Fields for Sulu (Yang, 2003), Ulamertoq (Nishio et al., 2019), Cerro de Almirez (López Sánchez-Vizcaíno et al., 2005), Dabieshan (Chen et al., 2013) and Voltri massif (De Hoog et al., 2014) are plotted for comparison. C) Chondrite normalized trace element concentrations of Isua humites. Trace-element data of Ulamertoq (Nishio et al., 2019) and Isua (Friend and Nutman, 2011) are plotted for comparison. Chondrite normalizing values are from (Sun and McDonough, 1989).

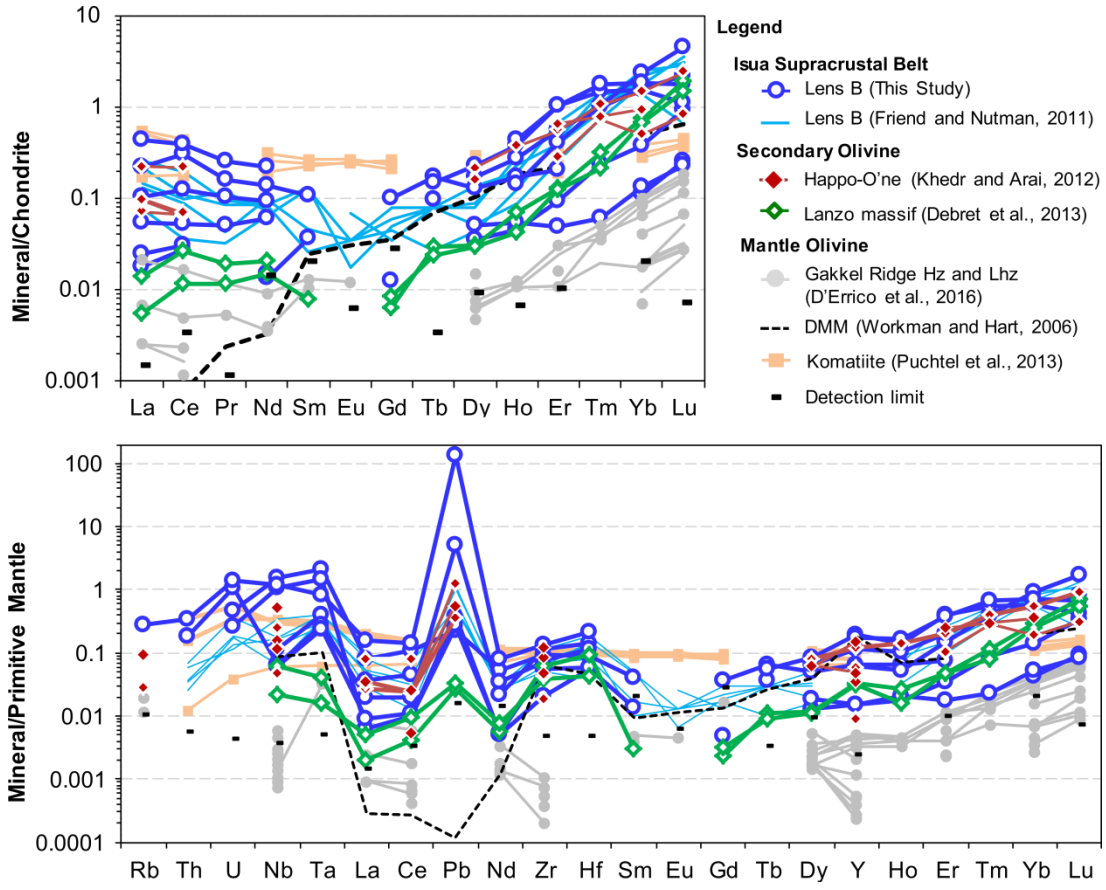

Figure 18. Chondrite and Primitive mantle normalized REE and multi-element patterns of Lens B olivine compared to other secondary olivines (Khedr and Arai, 2012; Debret et al., 2013a), mantle olivine (Gakkel Ridge harzburgites and lherzolites) (D'Errico et al., 2016) and olivine from komatiite olivine. Lens B olivine data from Friend and Nutman, 2011 are plotted for comparison. Normalizing values are from McDonough and Sun, 1995.

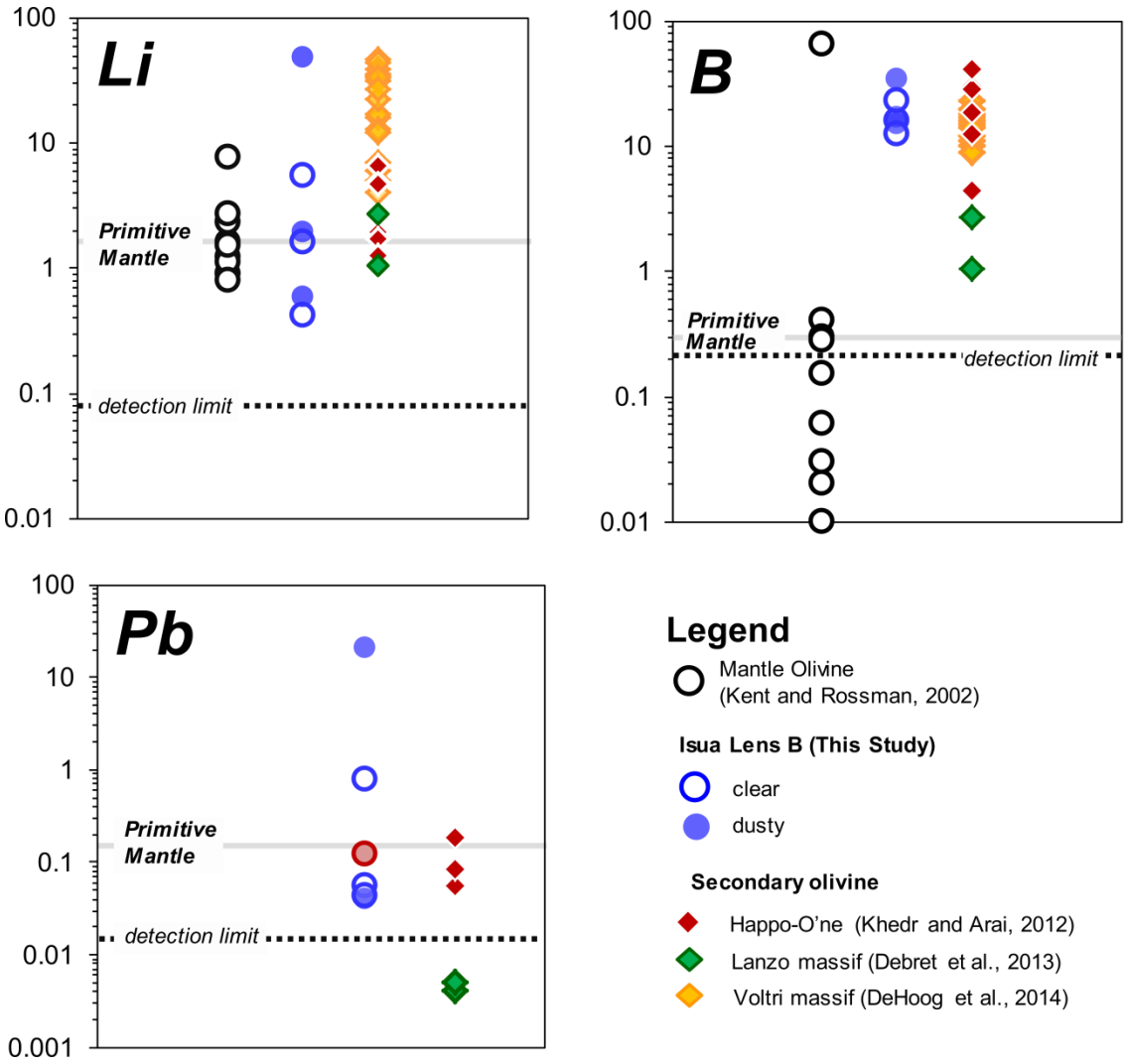

Figure 19. Fluid mobile elements (Li, B and Pb) are enriched in the Lens B olivine compared to mantle olivine (Kent and Rossman, 2002) and are comparable to other secondary olivines (Khedr and Arai, 2012; Debret et al., 2013a; De Hoog et al., 2014). Primitive mantle values are from (McDonough and Sun, 1995).

4.5. Discussion

4.5.1. Secondary olivine

The petrographic features of the olivine suggest a metamorphic origin such as an abundance of opaque inclusions and several generations of olivine characterized by overgrowth of clear olivine around dusty olivine. The extremely magnesian, highly variable NiO and MnO contents are typical characteristics of metamorphic olivine formed through deserpentinization. The enrichment of fluid mobile elements which is more obvious with boron and elevated HREE and HFSE contents are also typical of secondary olivine

(Scambelluri et al., 2004; Garrido et al., 2005; Khedr and Arai, 2012). The texture and composition of the Lens B metadunites olivine indicate a secondary origin.

4.5.2. Ti-Chu and Ti-Chn as high-pressure metamorphism marker in the ISB Lens B metadunites

Petrological experiments carried out on MgO-SiO_2-H_2O (MSH) system demonstrate the close association of humite, olivine and serpentine in prograde and retrograde metamorphism and the introduction of Ti into the system initiate such reactions (Shen et al., 2015). Ti-Chu breaks down at around 600°C within pressure conditions of <1GPa. The stability of Ti-Chu coincides with the antigorite stability field, however, fluorine stabilizes humites at 300°C higher (Grützner et al., 2017). The breakdown reaction of humite extends to lower pressure and higher temperature (<6.0GPa, Weiss, 1997) with higher Ti contents. Pyroxenes affect humite stability which expands to higher temperatures (Shen et al., 2015), however, pyroxene is absent in our samples. In a fluorine-free system, the higher pressure phase Ti-Chn is stable at 2.6 GPa below 700°C in an F-free system (Ti-Chn+Atg+Ol=Ti-Chu+H_2O). Intergrown Ti-Chu and Ti-Chn are also present in other HP serpentinites (e.g. Voltri Massif, Italy and Zermatt-Sass in the Western Alps) which is indicative of breakdown at 2.6 GPa below 700°C as suggested by experiments (González-Jiménez et al., 2017). In a Ti-rich system, the decomposition of Ti-Chu to Ti-Chn results in the formation of ilmenite (Ti-Chn+Atg=Ti-Chu+Ilm/Rt+H_2O). Ilmenite is absent in our sample set.

The lower pressure limit of Ti-Chn is around 620°C and 2.5 GPa and above ~700°C it is unstable (Shen et al., 2015). The lower pressure limit is characterized by Ti-Chn mantled by Ti-Chu. It was also observed that Ti-Chu has minimal participation in the Ti-Chn formation and could be stable at a wider range of P and T. In Ti-rich system characterized by the presence of Ti-rich oxides (rutile/ilmenite), the stability of Ti-Chn is lower at around 1.6 GPa before breakdown to Ti-Chu+Ti-oxides (Shen et al., 2015). Other localities with Ti-Chu and Ti-Chn association include Buell Park Kimberlite, Arizona, USA (Aoki et al., 1976; Smith, 1977); Dabieshan UHP Belt, China (Hermann et al., 2007) and in Isua supracrustal belt, Western Greenland (Dymek et al., 1988). Intergrown Ti-Chn and Ti-Chu are also found in the Fe-Ti gabbros in the Voltri Massif (Scambelluri and Rampone, 1999; Scambelluri et al., 2001). The Ti-rich humites are closely associated with diopside, chlorite and antigorite in the ultramafic rocks in Tianshan, China. Clinopyroxene is the main source of Ti with minor contributions from spinel in Tianshan ultramafics (Shen et al., 2015). The transition from Al-

diopside to diopside released the Ti to form Ti-Chu and Ti-Chn which is thought to have taken place during fluid-induced recrystallization of clinopyroxene which is attributed to the olivine crystallization at the expense of brucite (Scambelluri and Rampone, 1999).

In the Isua metadunites, Ti-Chn is commonly intergrown with Ti-Chu. The intergrowth relationship could suggest the instability of Ti-Chu during retrograde metamorphism and subsequent reaction with olivine and antigorite to form Ti-Chu. It was observed though that Ti-Chn reacts away at 2.5 GPa and below. It is, however, possible to form Ti-Chu from Ti-Chn in a Ti-rich system (presence Ti-rich phases) at lower pressure conditions (below 2.5 GPa) (Fig. 20). The abundance of magnetite replacing the chrome spinel is considered as the Ti source that formed the Ti-rich humites.

4.6. Metamorphic history

4.6.1. Early serpentinization

The protolith of Lens B is inferred based on the present mineral assemblage and composition. The dunitic protolith underwent hydration during an early serpentinization event forming serpentine and magnetite. The magnetite trails within olivine porphyroblasts are interpreted as relict mesh textures. The serpentinization and formation of magnetite are associated with lower-grade metamorphism around greenschist facies (Evans, 2008).

4.6.2. Prograde metamorphism

The prograde event caused deserpentinization and formation of the dusty olivine. The dehydration and fluids released could have mobilized Ti to form Ti-rich humite group of minerals. The humite group minerals are closely associated with the dusty olivine. The clear olivine overgrowth is also a part of this prograde event. The fluctuation of fluid infiltration and high-temperature serpentinization forming magnetite-free antigorite could have preceded the clear olivine formation. Several generations of intergrown olivine are also observed in the metamorphosed serpentinites from Cerro del Almirez, SE Spain (Trommsdorff et al., 1998).

The zonation observed in Cr-spinel with increasing Fe^{3+} from core to rim is also comparable to the typical alteration from low-grade to upper amphibolite facies with increasing ferric iron contents from low- to high- grade (Barnes and Roeder, 2001).

4.6.3. Later retrograde stage

Olivine porphyroblasts are cut by lizardite veinlets and these are in turn cut by coarse antigorite blades around the porphyroblasts. The texture suggests that the antigorite blades postdate the lizardite veinlets. The groundmass and blade antigorite are compositionally similar and could have formed around the same time. The antigorite patch inclusions have lower Al content and are closely associated with the dusty olivine. The inclusion patch could have formed at an earlier serpentinization event and relatively lower temperature. The Al content of antigorite stabilizes it at higher temperatures due to Tschermak's substitution (Padrón-Navarta et al., 2013).

The stability of lizardite and antigorite overlaps in temperatures between 320 and 390 390°C (>9 kbar) while above it antigorite is the only stable serpentine type. The addition of SiO_2 enables the conversion of antigorite at the lower end of the temperature ranges (Evans, 2004). The carbonation releases SiO_2 that could also be utilized in the formation of antigorite in this younger serpentinization event. The carbonation could have occurred twice replacing direct olivine porphyroblasts as shown in the magnesite pseudomorph after olivine and irregular magnesite replacing antigorite blades in the groundmass.

4.7. Timing of HP metamorphism

The exact timing of the high-pressure metamorphic event is not clear. However, metamorphic studies on garnets from metapelites in the western limb of ISB suggest that there are two main metamorphic events at approximately 3.74 Ga and c. 2.8 Ga. The earlier metamorphic event was characterized by temperatures above 610°C (Rollinson, 2002). A younger metamorphic event around 2.8 Ga was recorded with temperature between 480 to 550°C. The presence of kyanite limits the pressure of at least 6 kbar. The high-pressure conditions in the ultramafic rocks are not reflected in the surrounding amphibolite facies metamorphic rocks. This could suggest that the high-pressure metamorphism is younger than the two prominent metamorphic events in the area.

4.8. Implications for Archean metamorphism

Crust being buried by subduction-like processes or crustal thickening will be subjected to granulite facies conditions before reaching eclogite facies due to higher temperature conditions (Bjørnerud and Austrheim, 2004). Shallower slab dehydration is more likely the norm during the Archean. Hotter Archean slab temperature would have been dehydrated

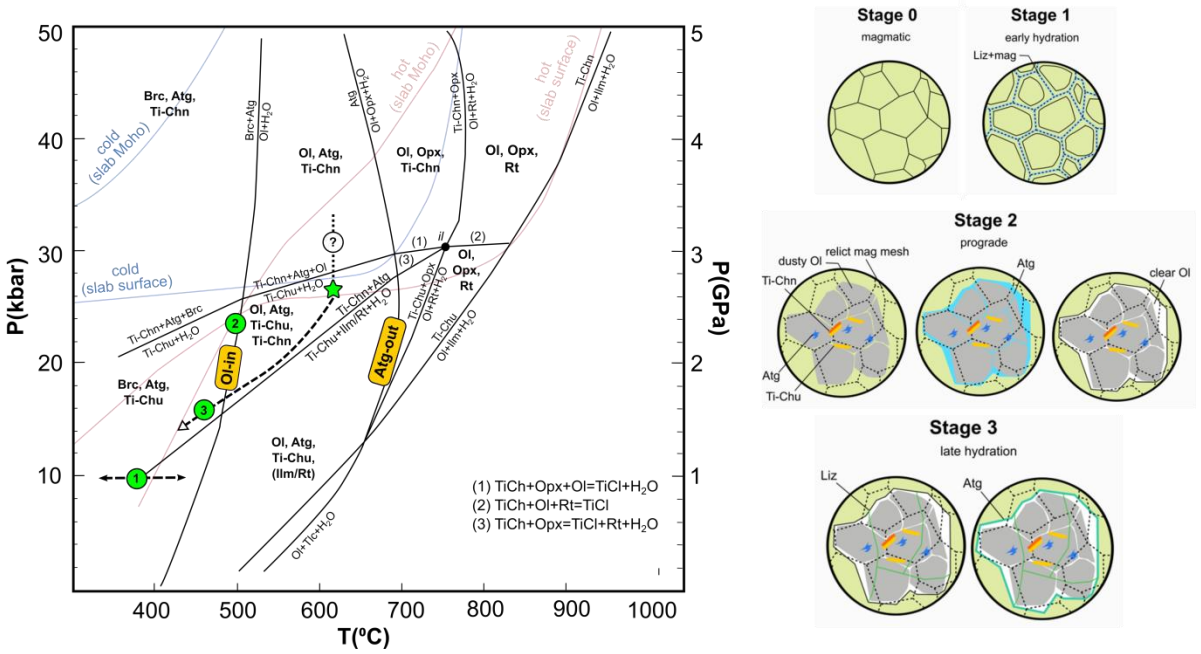

Figure 20. P-T diagram of Ti-Chn and Ti-Chu (modified from Shen et al., 2015) showing the metamorphic P-T path of ISB Lens B metadunites which involves different stages of hydration and dehydration.

before it sinks to the mantle. The high geothermal gradient during the Archean would have dehydrated at a shallow depth before reaching eclogite pressure conditions. Hence, eclogite formation in the Archean would have undergone higher temperature metamorphic facies compared to its modern counterparts. Modern subduction zones typically undergo blueschist before proceeding to eclogite (LowT/HP). Archean low dP/dT rocks record hotter geotherms relative to modern-day analogues due to higher geothermal gradient (e.g. van Hunen and Moyen 2012). The presence of Ti-Chn in Lens B metadunites suggests metamorphism at relatively high-pressure conditions. This high-pressure condition could be attributed to tectonic burial and subsequent exhumation. Although modern-day subduction zone processes have been unlikely to occur during the Archean time, the formation of new crust coupled with shallow subduction or crustal thickening would have operated in the past (Salters and Stracke, 2004; van Hunen and Moyen, 2012). Ultramafic rocks recording higher pressure PT path (allofacial) relative to the host rocks is also observed in other terranes containing ultramafic enclaves (e.g. Svartberget peridotite body, Vrijmoed et al., 2006; Kokchetav Massif, Kazakhstan, Hacker et al. 2003). Hence, Eoarchean ultramafic enclaves exhibit effectiveness in providing clearer evidence of high P metamorphic conditions than the

associated felsic crust. The combined petrologic and geochemical features of Lens B metadunites demonstrate that some Eoarchean crust attained eclogite-facies conditions.

4.9. Summary

The Lens B metadunites olivine texture and composition of the, within the Eoarchean Itsaq gneiss terrane, suggest a metamorphic origin with high Fo contents and varying NiO and MnO contents which are incomparable to typical mantle olivine. The presence of dusty and clear olivine types suggest two generations of olivine and complex metamorphic history. The metadunite protoliths underwent early serpentinization followed by subsequent prograde metamorphism forming inclusion-rich olivine and Ti-Chu/Ti-Chn that probably reached high-pressure conditions (~1.6-2.6 GPa; <650°C) to stabilize Ol+Atg±Ti-Chn±Ti-Chu. A high-temperature hydration-dehydration event is required to explain the formation of the clear olivine. Late serpentinization formed lizardite cutting both types of olivine and was replaced by coarse antigorite blades around the olivine porphyroblasts. The Eoarchean metadunites studied here exhibit features suggestive of HP metamorphism followed by retrograde metamorphism, which are petrological features that can be explained by deep burial followed by rapid exhumation, comparable to modern subduction zone channels, though the extent of actual subduction remains enigmatic.

5. SYMPLECTITE EXSOLUTIONS WITHIN LENS A OLIVINE

The vermicular intergrowth of more than one phase within a host of different composition is referred to as symplectites (Kushiro and Yoder Jr, 1966). The presence of symplectites in olivine could occur as oriented needle-like inclusions or as patchy domains (Khisina and Lorenz, 2015). Symplectites in olivine occur as spinel-pyroxene intergrowths containing elements that are typically present as trace amounts such as Cr, Ca, Al, Ti, V and Mn, some of which in high-valence state (e.g. $Cr^{3+}$and Fe^{3+}). Oriented needle-like and coarse patches varieties of these symplectites within olivines are found in terrestrial and extraterrestrial rocks including meteorites, dunites, troctolites and basalts (Moseley, 1984; Khisina and Lorenz, 2015). Symplectite formation is linked to the melt SiO_2 activity, temperature, pressure and oxygen fugacity (Markl et al., 2001).

Oriented spinel-pyroxene symplectites are present within the olivine of Lens A dunites located in the western limb of the Eoarchean Isua supracrustal belt (ISB) (Fig. 21). In this chapter, to the extent of our knowledge, we describe in detail for the first time the occurrence and possible origin of these symplectites in Lens A dunites. The petrological features and mineral chemistry of Lens A assemblage also contrasts with northern Lens B.

5.1. Mechanisms of formation of symplectites in olivine

The mechanisms involved in the formation of symplectites in olivine include: olivine interaction with residual and infiltrating melt (Bell et al., 1975; Elardo et al., 2012), diffusional metasomatism (Field, 2008), subsolidus precipitation (Ashworth and Chambers, 2000; Mikouchi et al., 2000; Khisina et al., 2008) and dehydrogenation-oxidation (Hwang et al., 2008; Yufeng et al., 2010; Khisina and Lorenz, 2015). Some of the symplectitic exsolutions are found in HP-UHP metamorphic rocks such as in olivine in garnet peridotites (Zhang et al., 1999) and some lower mantle inclusions in the diamond found in garnet lherzolites hosted by eclogites (Brenker et al., 2002).

The reaction of olivine with residual or infiltrating melt is commonly represented by clusters and masses along grain boundaries and as inclusions within the olivine (Bell et al., 1975). The reaction also proceeds from melt pathways along grain boundaries inward to the olivine (Elardo et al., 2012). Symplectites formed by diffusional metasomatism are characterized by reaction with adjacent phases such as pyroxenes (Field, 2008). The aforementioned models form symplectites occurring as patchy blebs and masses. The subsolidus precipitation and dehydrogenation-oxidation are more appropriate mechanisms in

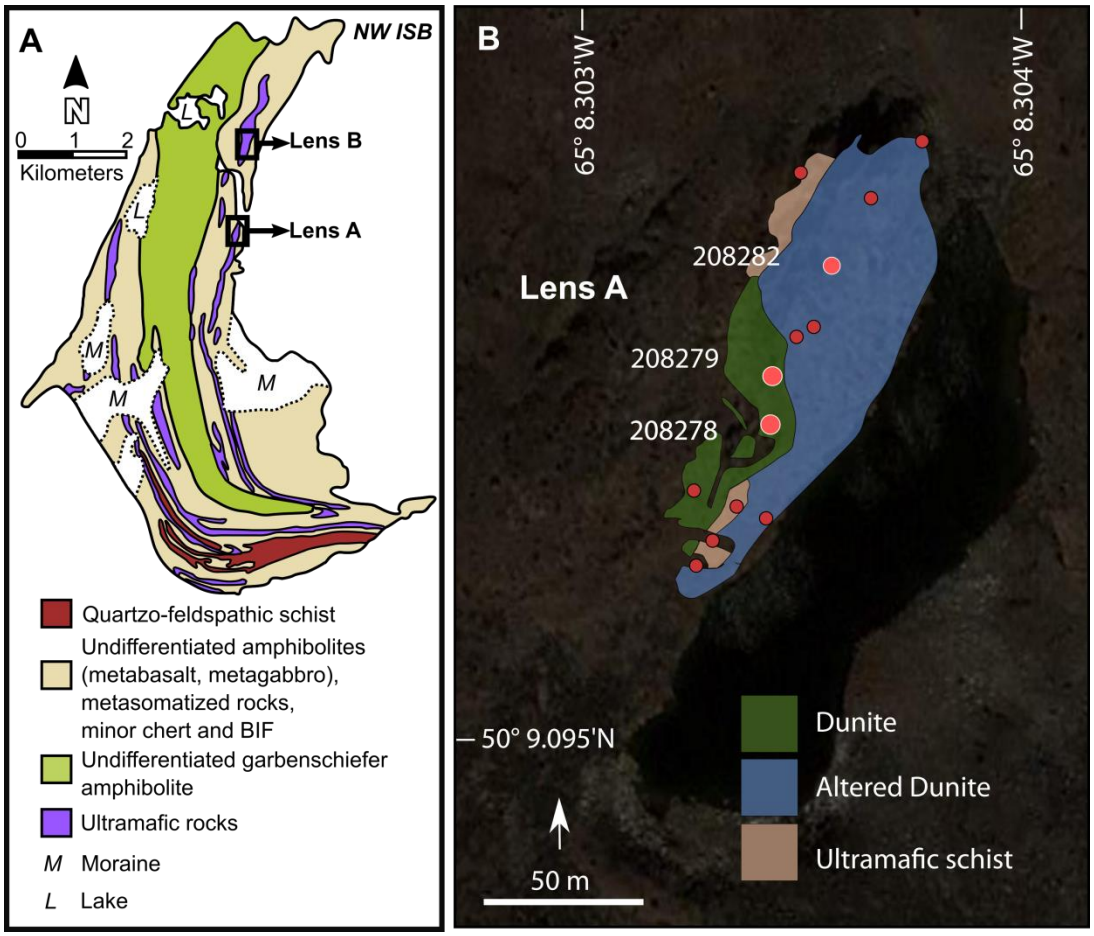

Figure 21. A) Map showing the location of Lens A in the western limb of the Isua supracrustal belt. B) Sampling location plotted on the geologic map of Lens A adopted from Friend and Nutman, 2011 (Aerial image from Google Earth).

explaining needle-like oriented symplectites. These symplectites exhibit a topotaxic relationship with the olivine host. The subsolidus precipitation involves the exsolution of Fe^{3+} and Cr^{3+} during cooling which produces spinel and silica (Moseley, 1984). The silica reacts with the olivine host to form pyroxene. The formation of clinopyroxene depends on the Ca content of the host olivine (Moseley, 1984; Ashworth and Chambers, 2000; Mikouchi et al., 2000). The dehydrogenation-oxidation reaction is a more composite mechanism similar to the previous model which involves the presence of OH in the host olivine (Hwang et al., 2008; Yufeng et al., 2010; Khisina and Lorenz, 2015).

5.1.1. Dehydrogenation and oxidation model

Olivine can accommodate ”water” (OH^- and H_2O) in their structure as structurally incorporated protons (Bell and Rossman, 1992). The olivine OH^- content is controlled by

pressure and H_2O content of the melt and its incorporation can be ascribed to the incorporation of water from a hydrous melt (Markl et al., 2001).

The incorporation of OH^- causes cation vacancy in the crystal structure forming point defects of hydrous olivine or humites (Khisina and Wirth, 2002; Churakov et al., 2003). Hydrous olivine occurs as needle-like or planar inclusions whereas humites are oriented along (100) and (001). These OH-bearing phases serve as precursor phases of the oriented symplectites. Physical-chemical changes can lead to proton removal incorporated with nominally anhydrous minerals (Skogby, 2006). Dehydrogenation is the release of structurally incorporated protons and is coupled with oxidation of transition metals (Hwang et al., 2008). Hydrogen is released from the crystal structure during dehydrogenation and unbound oxygen is compensated by the oxidation of Fe and/or Cr. The increase in the electrochemical potential of oxygen after hydrogen loss drives the cation diffusion (Hwang et al., 2008; Khisina et al., 2013). Cation diffusion ($Mg_{precursor} \leftrightarrow Ca_{olivine}$ and $Mg_{precursor} \leftrightarrow Cr_{olivine}$) between the host olivine and precursor phase also contributes to the symplectite formation as evidenced by concentration profiles from lunar olivine (Khisina et al., 2013) (Fig. 22).

Dehydrogenation is associated with high-temperature decompression, an increase in oxygen fugacity, water redistribution caused by dry melt interaction (Khisina and Lorenz, 2015). The hydrous olivine and humite point defects form oriented inclusions in olivine and could serve as precursor phase to be replaced by spinel-clinopyroxene symplectites. Oriented symplectites formation can be explained by the discussed dehydrogenation of OH^- point defect and subsequent formation of more than one phase.

5.2. Sample description

Ultramafic lenses (Lens A and B) in the western limb of ISB are interpreted to have been least affected by deformation and chemical modifications as discussed in the previous chapter. The southern ultramafic body, Lens A, is dunitic with a lesser altered inner body and rimmed by ultramafic schist (Fig. XX). Lens A has a simpler mineral assemblage which is primarily composed of olivine, serpentine and spinel. Dunites from Lens A consist of fine- to coarse-grained olivine and are weakly serpentinized. The coarse olivines are commonly elongate and measure up to more than 1 cm in its longer axis. Olivine grains are brownish and oriented spinel-clinopyroxene symplectites within olivine are present in the representative Lens A dunites (Fig. 23 a-d). The symplectite exsolutions occur as dendritic platelets that are oriented in at least one direction. Antigorite is the main serpentine phase

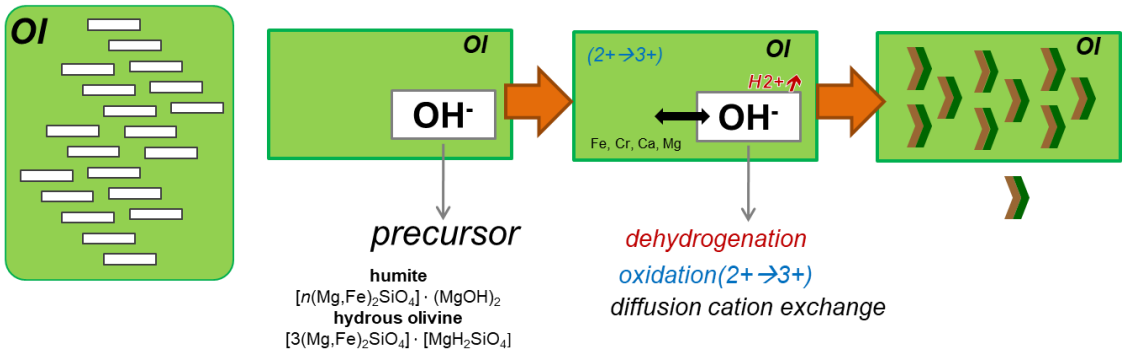

Figure 22. Dehydrogenation and oxidation model in olivine (Hwang et al., 2008; Khisina and Lorenz, 2015).

occurring as coarse blades around olivine, inclusions and interlocking groundmass. Relic discrete spinel grains show zonation which is related to compositional variation due to alteration. Minor amounts of amphiboles are also found as inclusion within olivine.

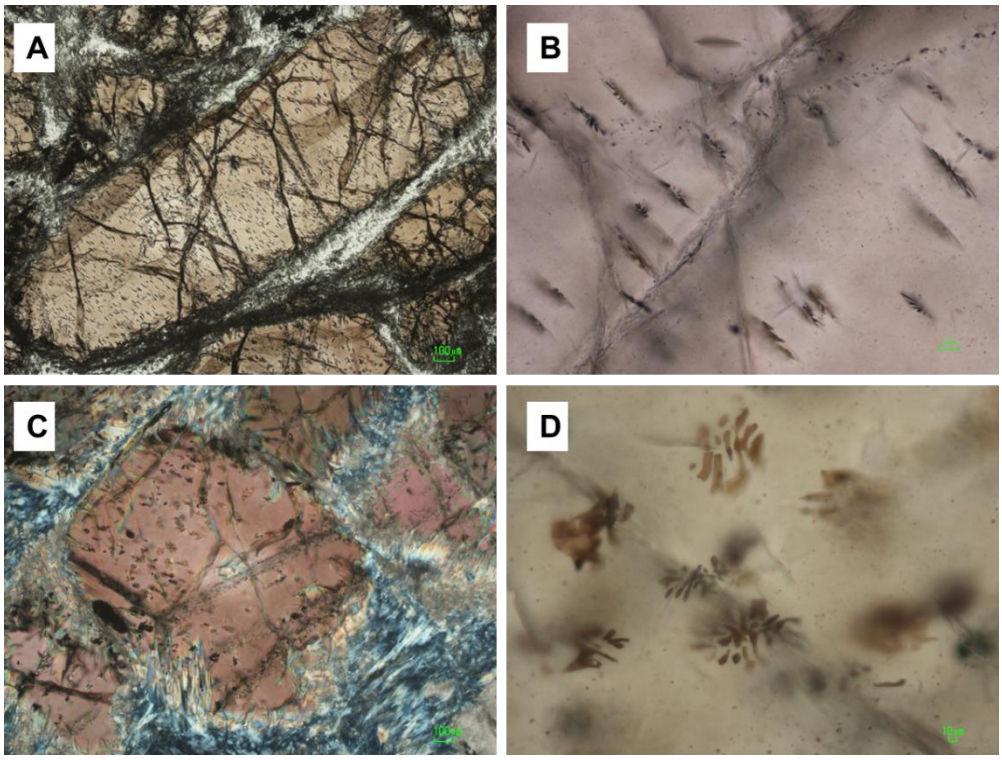

Figure 23. Representative photomicrographs of Lens A dunitic rocks. The coarse olivine grains are brownish and contain abundant oriented Cr-spinel-diopside symplectite inclusions.

5.3. Mineral chemistry

Major element mineral chemistry was determined using an electron microprobe analyzer (Chapter 3). The forsterite content (100xMg/Mg+Fe^{2+}) of the olivine ranges from 89-92 (Fig. 24). The NiO and MnO contents range from 0.45-0.61 wt.% and 0.1-0.2 wt.%, respectively (Table XX). Portions away from the clinopyroxene-spinel symplectites yielded olivine CaO contents ranging from 0.01-0.2 wt.%. The average Ca and Cr contents of the olivine were determined by analyzing the entire grains by a series of LA-ICPMS points (Fig. 25). The results yielded an average of 1200 ppm for Ca and 553 ppm for Cr. The silicate phase in the symplectites is diopside (Mg#=0.94-0.97; $Wo_{43.27-49.37}$, $En_{48.95-53.06}$, $Fs_{1.68-3.67}$). The spinel phase in the symplectite is too small to be analyzed by microprobe to determine the exact composition, however, analyses detected Fe, Cr, Mg (Cr_2O_3=5.50 wt.%, FeO=9.82 wt.% and MgO=28.81 wt.%) and will be referred to as Cr-spinel hereafter. Serpentine is mainly antigorite with Mg# (=Mg/Mg+Fe^{2+}) ranging from 0.92-0.96 and Al_2O_3 content between 0.96-2.67 wt.%. The Mg/Si values range from 1.31-1.32.

Spinel cores have lower Cr# (=Cr/Cr+Al) and higher Mg# than the rim. Cores are characterized by Cr# ranging from 0.72-0.74 while the rim portion ranges from (0.98-1.0). Spinel core Mg# ranges from 0.22-0.27 while the rim portion is between 0.02-0.09. The Fe^{3+} content of the core is lower (0.12-0.13) than the rim portion (0.64-1.86) (Fig. 26).

5.4. Discussion

5.4.1. Comparison with Lens B, more igneous features

The whole-rock composition of Lens A and Lens B shows strong similarities (Fig. 26-27). The Cr# of the spinel cores are also similar (0.74). However, the Mg# of Lens A spinel cores (0.22-0327) is lower than the spinel in Lens B (0.43). Olivine composition is also different comparing Lens A and B. The olivine in Lens B are highly forsteritic (96-98) and have higher NiO and MnO contents. This is in contrast with Lens A having lower forsterite contents, NiO and MnO contents. The metamorphic olivine signature in Lens A is not evident unlike Lens B which suggest that the former preserve more primary igneous features.

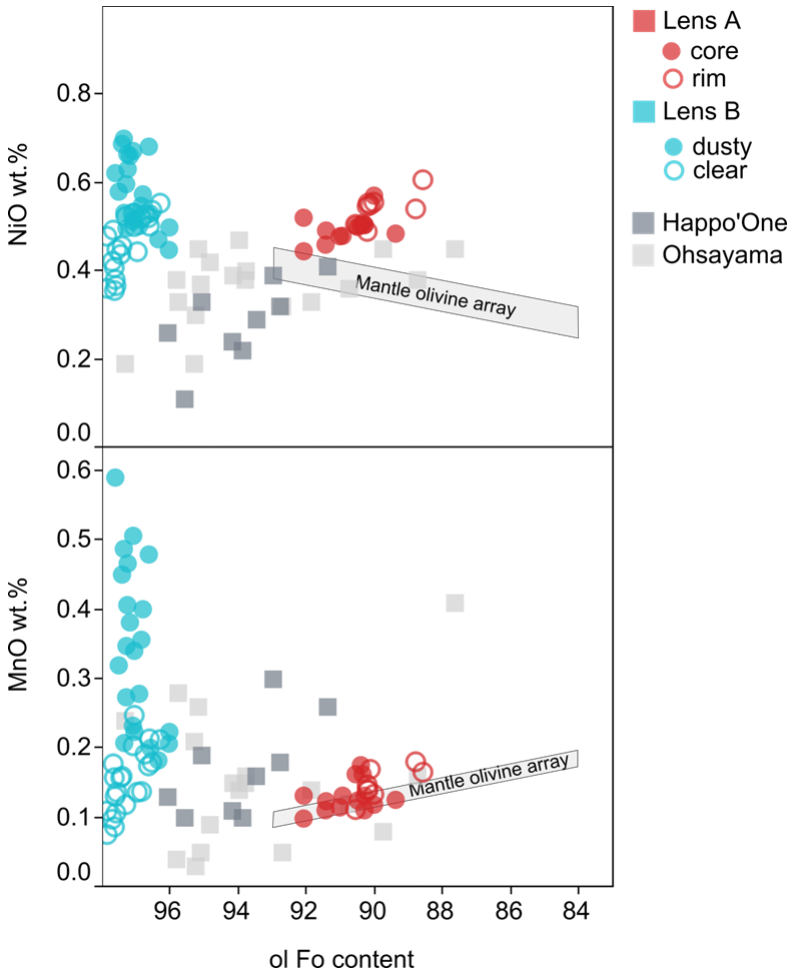

Figure 24. Olivine Mg# versus MnO wt.% and NiO wt% of Lens A samples. Olivine composition of Lens B and other secondary olivine from Happo-O'ne (Khedr and Arai, 2013) and other SW Japan metaperidotites (Ohsayama, Tari-Misaka and Yanomine) (Nozaka, 2003) are plotted for comparison.

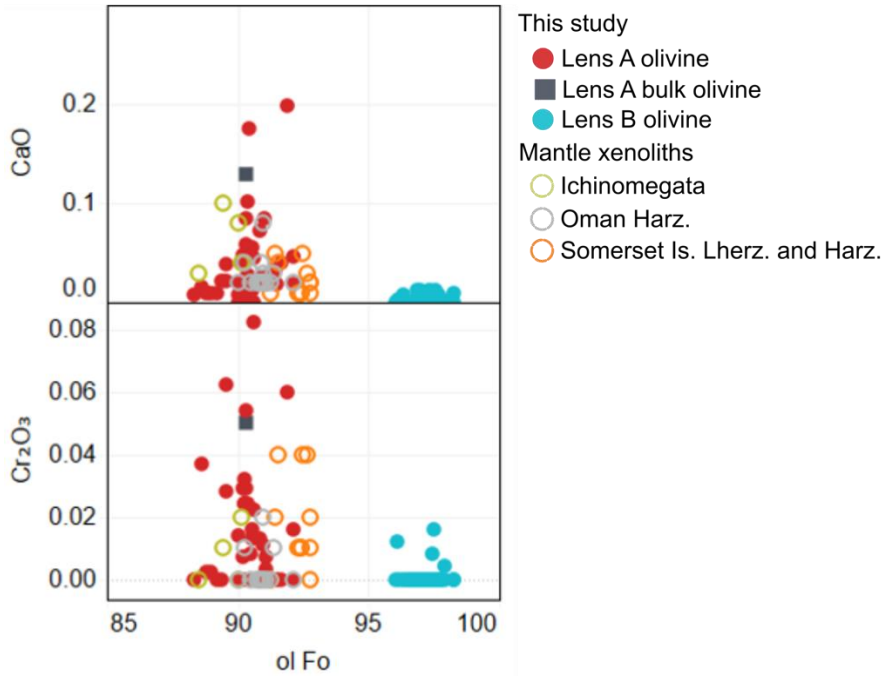

Figure 25. Fo content plotted against CaO and Cr_2O_3 of olivine in the Lens A dunitic samples compared to mantle xenolith olivine from other areas (Takahashi, 1980; Schmidberger and Francis, 1999; Hanghøj et al., 2010).

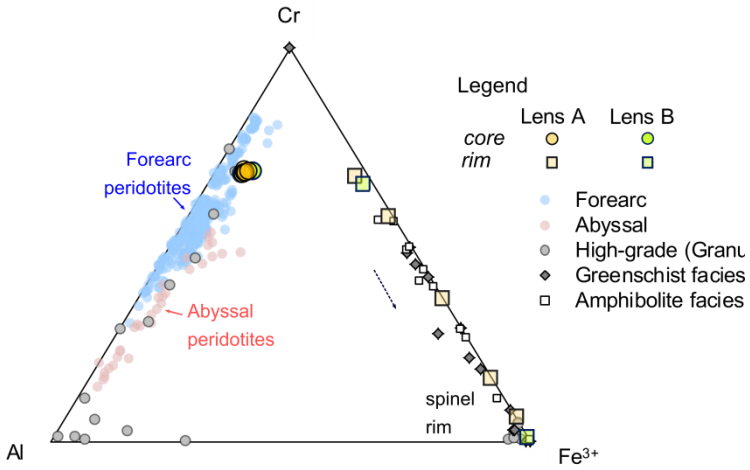

Figure 26. Cr-Fe^{3+}-Al ternary plot for the Lens A spinel composition compared with Lens B spinel and other primary and metamorphic spinel. Composition of spinels from forearc (Ishii et al., 1992), abyssal (Dick and Bullen, 1984) and various metamorphosed rocks (Barnes and Roeder, 2001) are plotted for comparison.

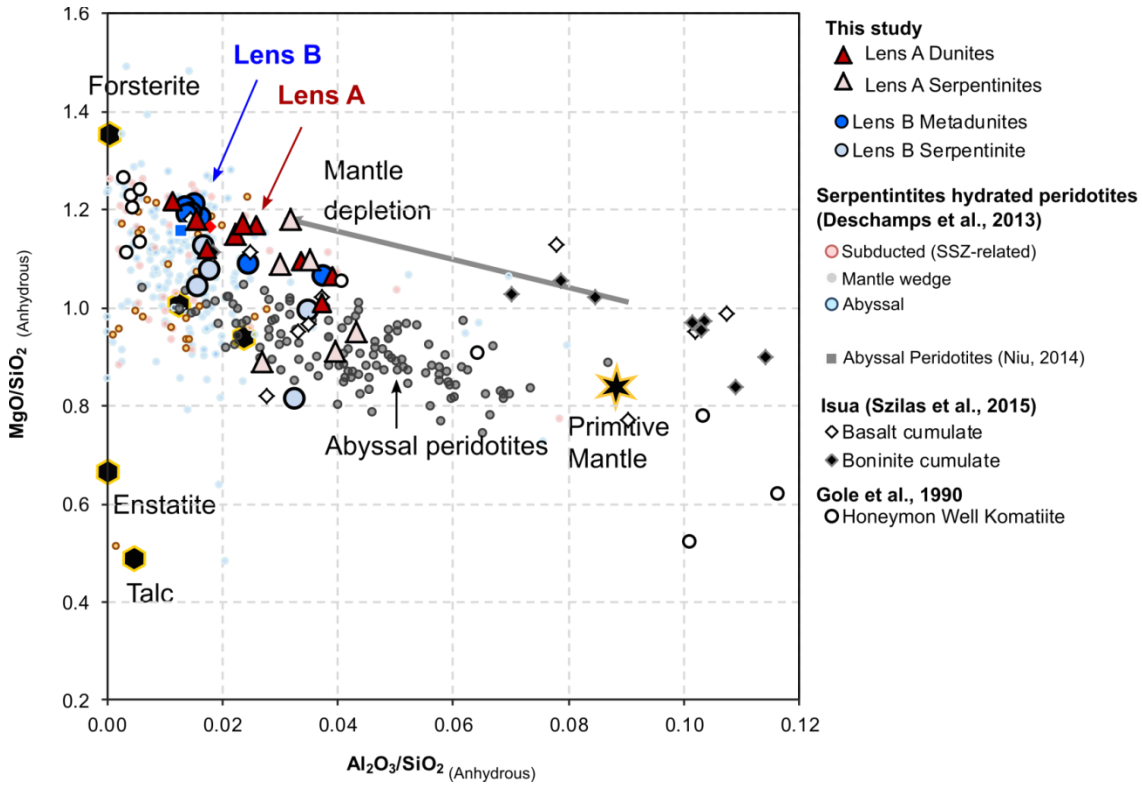

Figure 27. MgO/SiO_2 plotted against Al_2O_3/SiO_2 (calculated volatile-free) of ISB ultramafic rocks compared from other serpentinites (and hydrated peridotites) from various tectonic settings compiled (Deschamps et al., 2013). The compositions of abyssal peridotites (Niu, 2004), primitive mantle (McDonough and Sun, 1995) are also plotted. The same sample set also show lower MgO/SiO_2 and increase in Al_2O_3/SiO_2 for antigorite-dominated samples.

5.4.2. Origin of symplectite in Lens A olivine

The occurrence of oriented symplectite inclusions in the Lens A olivine is more associated with subsolidus diffusion mechanism and dehydration-oxidation model. The symplectites exhibit topotaxic relationship with host olivine and are independent of cracks and grain boundaries. The average Ca and Cr content of the olivine is not anomalously high and are still comparable to typical primary olivine. These features suggest that the elements associated with the symplectites (Ca, Cr and Fe) can be sourced from the host olivine.

Olivine can contain Fe^{3+} and Cr^{3+} in their structure (Duke, 1976; Moseley, 1984). In the subsolidus model, the spinel-clinopyroxene symplectite is attributed to the presence of ferric iron in the olivine which formed the symplectites as a result of repulsion of ferric iron and Si^{4+} in the crystal structure. Clinopyroxene hosts elements that are incompatible with

olivine structure (Moseley, 1984). The diffusion coefficient of Cr^{3+} is significantly lower than calcium (Ito and Ganguly, 2006) and diffusion of Cr^{2+} and oxidation along symplectites sites is another way to explain its formation. The diffusion of transition metals in its divalent state and subsequent oxidation can be explained by the dehydrogenation of an OH^- bearing phase. Hydrous olivine and humite defects occur as oriented planar inclusions acting as precursor phases. In the dehydrogenation model, the Cr was diffused in its divalent state and was oxidized at the olivine host-precursor phase boundary. These platelets could be initial hydrous olivine or humite layers that were dehydrogenized and initiated oxidation. The dehydrogenation and oxidation mechanism is also coupled with cation diffusion from the precursor hydrous olivine and host olivine. However, in Lens A, no clinohumites were found unlike samples from Lens B. The dehydrogenation mode of formation could be further strengthened by the presence of relic OH^- in the olivine which is not confirmed in the current study. The discussed mechanisms best explain the oriented symplectites in Lens A olivine. However, in the case of dehydrogenation-oxidation, this could suggest the presence of water in the olivine structure. The presence of OH in the olivine could be a potential marker of crystallization from a hydrous melt similar to subduction environment. This hypothesis needs additional evidence such as measurements of relic OH in the olivine. The two mechanisms discussed are not ruled out.

Formation of symplectites based on mathematical calculations based on rate energy dissipation, reaction rate and spacing, could take hundreds of years at temperatures above 800°C (Ashworth and Chambers, 2000). The symplectites regardless of the exact mechanism of formation suggest decompression at long-term heating conditions.

5.5. Summary

In spite of the close bulk-rock geochemical similarities and location of Lens A from Lens B, there is a significant contrast in the texture and mineral composition specifically in olivine. Lens A is composed of simpler mineral assemblage composed chiefly by olivine and serpentine. The olivine grains are entirely brownish and occur in some portions as megacrysts (more than 1 cm). The most striking feature is the presence of oriented Cr-spinel and diopside symplectites within the olivine. The intergrown phases occur as dendritic platelets within olivine and are oriented at a single direction relative to the olivine host. The occurrence of the symplectites could be explained by subsolidus diffusion of elements (Fe, Cr and Ca) from olivine to the symplectite sites. This mechanism involves diffusion of transition metals (Fe

and Cr) in its trivalent state and reaction of excess silica with the olivine to produce pyroxene. Another mechanism is dehydrogenation-oxidation which also similar to subsolidus diffusion but ascribes the oxidation of divalent transition metals with hydrogen loss of a precursor OH^- phase either hydrous olivine or humite which form oriented planar defects in the olivine. The defects serve as precursor sites for symplectites. The latter will be supported by measurements of relic OH^- in the olivine and detailed crystallographic description of the symplectites which is not available in the current study. The proposed mechanisms however suggest high-temperature decompression. If dehydrogenation did occur this suggests the presence of water in the olivine structure that could imply formation from a hydrous melt similar to subduction zones. Combined petrologic and chemical features of the Lens A dunites suggest that it retained more igneous features than the neighboring Lens B.

6. COMPLEX METAMORPHIC IMPRINTS IN OTHER ULTRAMAFIC BODIES IN SOUTHERN WEST GREENLAND: METAMORPHISM IN ULAMERTOQ PERIDOTITE BODY

High-grade metamorphism and its effect on the composition on chromites is manifested in the nearby Ulamertoq peridotite body in the Akia terrane, west of the Isua supracrustal belt. The Ulamertoq peridotite body hosts chromitites that exhibit contrasting textural and compositional characteristics. In this section, we discuss the effects of metamorphism and metasomatism manifesting as cation mobility at high temperatures even in spinels which are considered to be resistant to weathering and alteration. This study focuses on the Ulamertoq peridotite body in the Akia terrane which lies in the same region with the Isua supracrustal belt in southern Western Greenland.

6.1. Geological setting

The Nuuk region in southern West Greenland which forms part of the North Atlantic Craton can be subdivided into three terranes: Akia, Akulleq and Tarsiusarsuag (Fig.26). In the Fiskefjord area in the 3.0 Ga (Garde et al., 2000) Akia terrane, amphibolites, dioritic to tonalitic orthogneiss and peridotites are exposed. The occurrence of peridotites is similar to those in the ISB, as discontinuous lensoid bodies hosted within tonalitic orthogneiss. Several ultramafic bodies are also exposed in the vicinity which includes Miaggoq, Seqi and Amikoq. The Ulamertoq peridotite body is approximately 1km x 1.5km and is characterized by the assemblage olivine±orthopyroxene±clinopyroxene+amphibole. Some portions of the Ulamertoq peridotite body contain clinopyroxene which not common among the ultramafic bodies in Akia terrane. The ultramafic body is enveloped by biotite-schist reaction zone which serves as the boundary with the surrounding orthogneiss. Norites intrude the peridotite body which is then cut by younger pink granites (Garde et al., 2000; Szilas et al., 2018a).

6.2. Zoned and homogeneous chromites

Chromitites were sampled from two different localities within the Ulamertoq peridotite body. The chromitites exhibit contrasting textural and chemical characteristics which consist of a) zoned chromites and b) homogeneous chromites. The zoned chromites exhibit Mg-Al increase coupled with Cr-Fe decrease from core to rim and are hosted within olivine+orthopyroxene+magnesiohornblende+phlogopite dunitic rock.

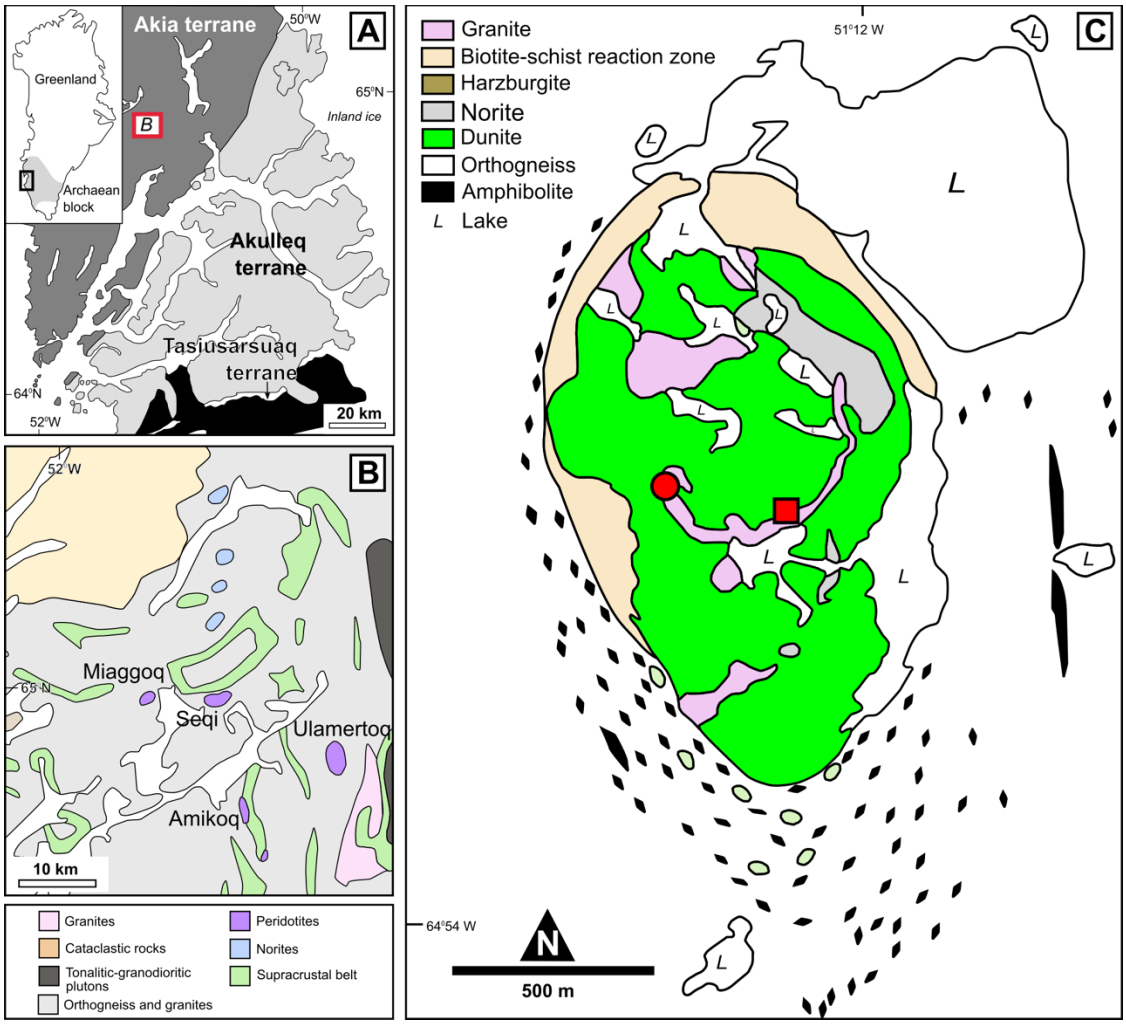

Figure 28. (A) Simplified geologic map of southern West Greenland showing the Akia, Akulleq, and Tarsiusarsuaq terranes; (B) Map showing the ultramafic bodies within the Mesoarchaean orthogneiss in Akia terrane (map adapted from Szilas et al., 2018b) (C) Geologic map of Ulamertoq peridotite body showing the sampling locations of chromitites with zoned chromites (filled circle) and homogeneous chromites (filled square) (map adapted from Garde, 1997).

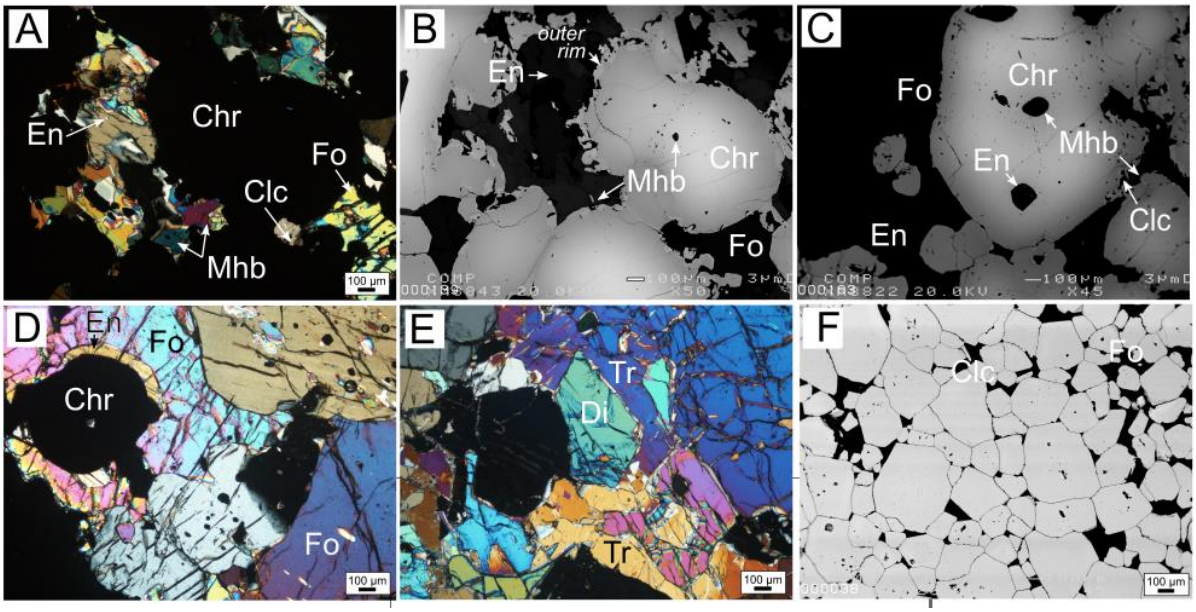

Figure 29. A) Interstitial silicate minerals in samples with zoned chromites (Chr) are characterized by that include enstatite (En), magnesiohornblende (Mhb), forsterite (Fo), and clinochlore (Clc); B-C) Backscattered electron (BSE) images of zoned chromites exhibiting gradual change from bright cores to dark rims. Irregular outer rims occur as overgrowths and have sharp contacts with dark rims; (D) Photomicrographs of the peridotite envelope (E) and host (F) of the chromitite hosting zoned chromites; E) Orthopyroxene is absent in the peridotite host of the homogeneous chromite but contains diopside (Di) and tremolite (Tr); (F) BSE image of the homogenous chromites wherein compositional zonation is absent.

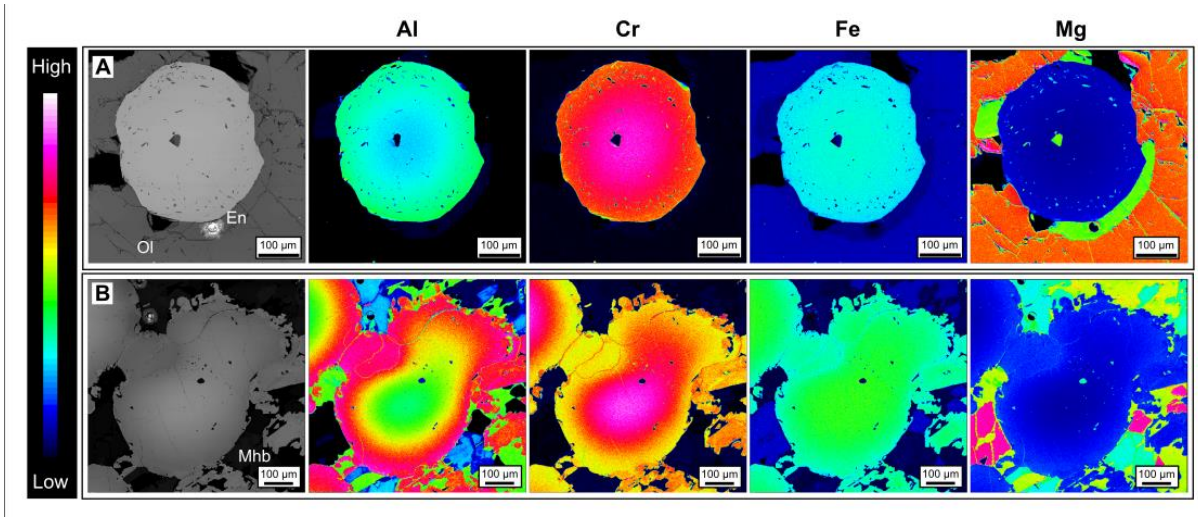

Figure 30. Backscattered scanning electron microscope (SEM) images and compositional maps of zoned chromites from the Ulamertoq peridotite body. A) Accessory chromite in the peridotite envelope enclosed by olivine and minor orthopyroxene shows less variation from core to rim. B) Chromite surrounded by Al-rich silicates (e.g. chlorite, amphibole, and orthopyroxene) shows a well-developed zonation of a Cr-rich core and Al-rich rims. Some chlorites fill the pores in the outer rim portions. The outermost rim occurs as irregular overgrowth, and is slightly Cr-rich; (B) Accessory chromite in the peridotite envelope enclosed by olivine and minor orthopyroxene shows less variation from core to rim.

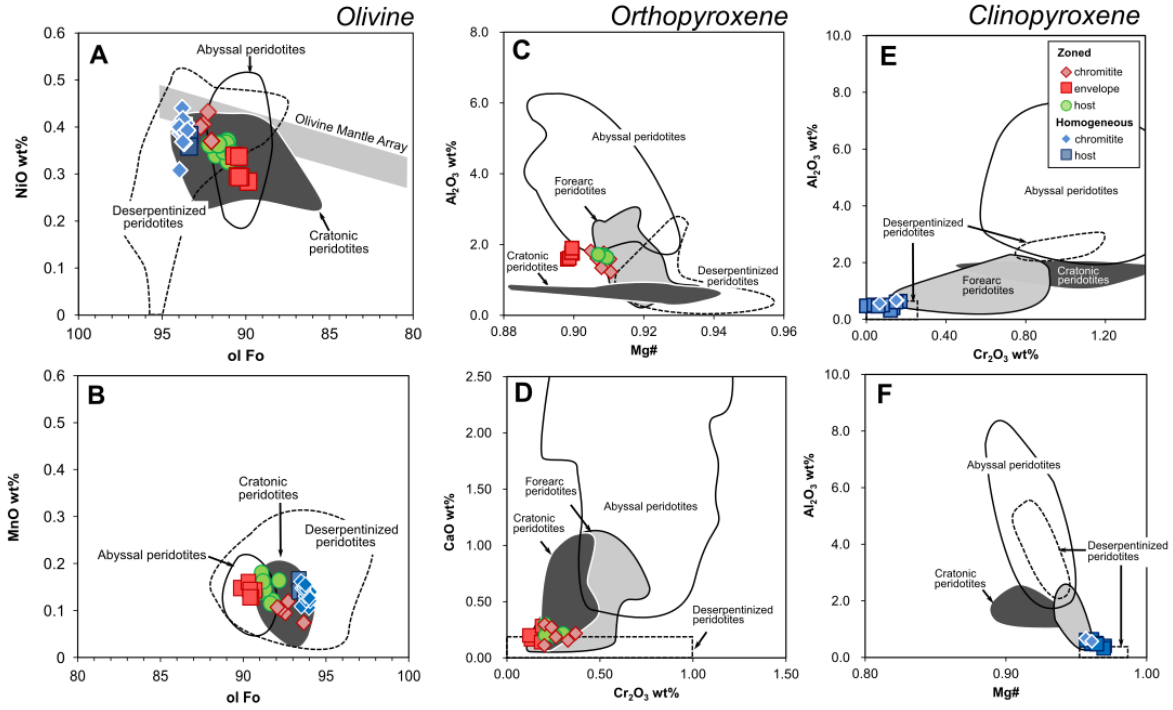

Figure 31. A-B) Olivine forsterite content vs. NiO wt.% and MnO wt. % plot of the Ulamertoq samples. Compositional fields of other metamorphic olivine and residual mantle olivine from typical abyssal peridotites and cratonic spinel-facies peridotites (Larsen, 1982; Boyd et al., 1997; Bernstein et al., 1998; Kelemen et al., 1998; Sand et al., 2009) are also plotted. C-D) Mg# vs. Al_2O_3 wt. % and Cr_2O_3 wt. % vs. CaO wt. % plots of orthopyroxenes (Opx); E-F) Mg# vs. Al_2O_3 wt. % and Cr_2O_3 wt. % vs. Al_2O_3 wt. % of the clinopyroxenes (Cpx). The mantle olivine array is from Takahashi (1980); Compositions of typical residual abyssal peridotite and metamorphic olivine from the Happo-O'ne peridotite complex (Khedr and Arai, 2012), Tari-Misaka (Arai, 1975), Ohsa-Yama (Nozaka and Shibata, 1995) in Japan, and abyssal peridotites (Warren, 2016) are also included for comparison.

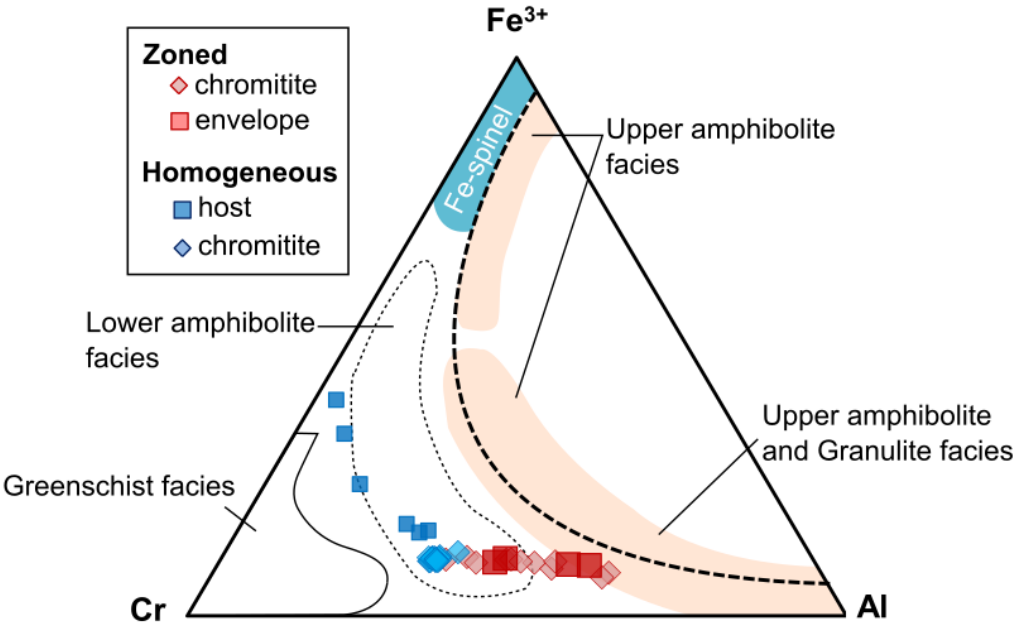

Figure 32. Cr–Fe^{3+}–Al ternary plot of the Ulamertoq chromites plotted with fields of metamorphic spinels from different metamorphic grades (metamorphic spinel fields taken from the data of Purvis et al., 1972, Evans and Frost, 1975, and Freitas Suita and Strieder, 1996.

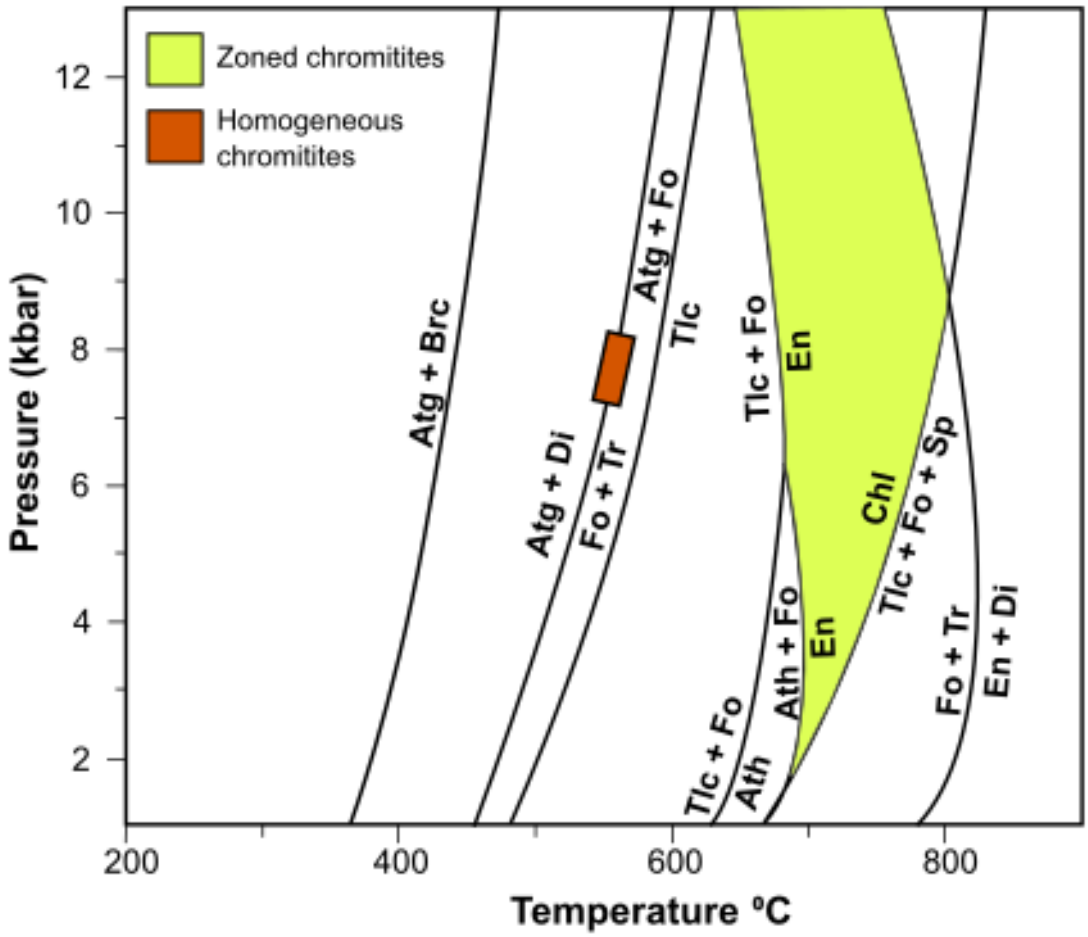

Figure 33. CaO-MgO-SiO_2-H_2O phase equilibria of ultramafic rocks with the stability field of the zoned and homgeneus chromites (Berman et al., 1986; Bucher and Frey, 2002). Abbreviations: Atg = antigorite, Brc = brucite, Di = diopside, Fo = Forsterite, Tr = tremolite, Tlc = talc, Ath = anthophyllite, Chl = chlorite, Sp = spinel, En = enstatite.

The outermost rim overgrowths of the zoned chromites are Al-poor and are associated with clinochlore. The homogenous chromites have uniform composition, finer and more closely packed relative to the zone chromites. Phlogopite is also present in the samples containing homogeneous chromites. The olivine grains in both samples contain magnetite inclusion and are characterized by low NiO content and variable MnO contents (Fig. 29 A-B) which could be features linked to deserpentinization. The pyroxenes also exhibit composition suggesting a secondary origin (Opx=low Al_2O_3 and CaO; Cpx=low Al_2O_3 and Cr_2O_3) (Fig. 29 C-F).

6.3. Discussion

6.3.1. Mechanism for zone chromites formation

Several mechanisms could explain the formation of zoned chromites with Al-rich rims. Reaction with residual melt which is Al-rich is observed in the chromites in the Rhum layered complex (Henderson and Wood, 1982). The zonation of chromites is attributed to the postcumulus reaction with intercumulus melt.

Subsolidus reaction with surrounding Al-rich phases is another mechanism (Hulbert and Von Gruenewaldt, 1985; Bai et al., 2018). The zone chromites in the Red Mountain mafic-ultramafic complex, Rhum layered complex and Yanmenguan mafic-ultramafic complex in China are associated with pyroxenes, amphiboles and plagioclase and reaction with such Al-rich phases at high temperatures is also one of the suggested mechanisms. The heating and reaction of chlorite and chromite is another reaction that could also cause Al-rich rims which is observed in the Calzadilla de los Barros ultramafic body (Spain). The formation of chlorite in the retrograde path and subsequent heating (due to intrusive rocks) could break-down chlorite and enrich the chromite rims with Al.

6.3.2. Metamorphic imprints and P-T path

The zoned chromites are hosted in orthopyroxene-bearing dunitic rocks without clinopyroxene. In the CaO-MgO-SiO_2-H_2O phase equilibria, this assemblage is stable above 650 ◦C and below 800◦C (Spear, 1993). In prograde metamorphism, orthopyroxene forms through the reaction: $2Tlc + 2Fo = 5En + 2H_2O$ (Tlc = talc; Fo = forsterite; En = enstatite). The Al increase in the rim portion can be attributed to the reaction of chromite with Al-rich silicates triggered by high-grade metamorphism (Evans and Trommsdorff, 1978). The outermost rims of the chromites exhibit spongy texture with abundant chlorite inclusions. The outermost rim formed the latest and could be linked to retrograde metamorphism with chlorite formation expense of Al decrease from the outermost chromite rim. In the homogenous chromites, the absence of orthopyroxene and equilibration with tremolite limit the temperature along the Atg+Di→Fo+Tr univariant curve around 530 ◦C. The presence of phlogopite also suggests metasomatism of K-bearing fluids. The Ulamertoq peridotite chromitites show metamorphic characteristics that suggest different metamorphic grades which could be explained by varying metasomatic infiltration paths.

7. CONCLUSIONS

The ultramafic bodies within the Eoarchean ISB show petrological features that are believed to be intact and are least affected by chemical modification and deformation. However, detailed petrological and geochemical investigation reveals some key differences between Lens A and B.

The olivine texture and composition of the Lens B metadunites exhibit characteristics that are indicative of a metamorphic origin with high Fo contents and varying NiO and MnO contents that are distinct from typical mantle olivine. Texturally distinct olivine types in the Lens B metadunites suggest a complex metamorphic history forming two generations of olivine. The metadunite protoliths underwent early serpentinization before a prograde metamorphic event forming inclusion-rich olivine (dusty) and Ti-rich humite-group minerals that probably reached high-pressure conditions (~1.6-2.6 GPa; <650°C) to stabilize Ol+Atg+Ti-Chn+Ti-Chu. This was followed by a high-temperature hydration-dehydration event which is inferred to explain the formation of the clear olivine. Late serpentinization forming lizardite which cut both types of olivine and was replaced by coarse antigorite blades. The exact timing of the high-pressure metamorphic event is not clear. However, pressure estimation suggests that it occurred younger than the 3.74 Ga metamorphic event characterized by temperatures above 610°C and a minimum pressure of 6 kbar. On the contrary, Lens A shows minimal metamorphic imprints and more igneous features than Lens B. Dunites from Lens A shows strong contrast mineralogical features and texture compared to Lens B suggesting a difference in the P-T path or exhumation history. Lens A dunites consist of oriented symplectite-bearing olivine. The origin of this symplectite could be ascribed to subsolidus diffusion of elements from the host olivine or dehydrogenation-oxidation. The latter case would imply the presence of water in the olivine structure of Lens A. The two ultramafic lenses share common similarities in their bulk-rock composition. However, their contrasting petrological features could be associated with differences in metamorphic histories or emplacement histories. The complex metamorphic history of ultramafic rocks in southern Western Greenland is also observed in the nearby Ulamertoq body in the Akia terrane.

The Eoarchean age metadunites (Lens B) in this study exhibit features suggestive of HP metamorphism followed by retrograde metamorphism, which are characteristics that can be explained by deep burial followed by rapid exhumation, comparable to modern subduction

zone channels, though the extent of actual subduction remains unclear. Studies on primary igneous features of ultramafic rocks can be more focused on Lens A.

8. ACKNOWLEDGEMENTS

This study was funded by a Grant-in-Aid for Scientific Research of the Ministry of Education Culture, Sports, Science and Technology of Japan (No. 16H05741: TM) under the supervision of Prof. Tomoaki Morishita. Prof. Kristoffer Szilas acknowledges the Carlsberg Foundation for financial support of the fieldwork in Greenland to collect the Ulamertoq samples. The author would like to thank the Government of Japan's Ministry of Education, Culture, Sports, Science and Technology (MEXT or Monbukagakusho) and Kanazawa University for the financial support during the Ph.D. course. My deepest gratitude is extended to Prof. Tomoaki Morishita for all the guidance and support in all parts of this study. I would also like to thank Dr. Akihiro Tamura, Prof. Susumu Umino, Prof. Tomoyuki Mizukami, Dr. Kenichiro Tani, Dr. Yumiko Harigane, Prof. Kristoffer Szilas, Prof. D. Graham Pearson, Ryoko Yamaguchi and Ikuya Nishio and for all support in analytical and scientific discussions in the Greenland project topics. I would also like to thank all students in the Petrology group of Kanazawa University for the fun learning experience and memories. I would also like to thank Dr. Betchaida Payot and the whole Rushurgent Working Group of the University of the Philippines for the unwavering support. This study is dedicated to all of my family and friends.

9. REFERENCES

Abbott, D., Burgess, L., Longhi, J., and Smith, W.H.F., 1994, An empirical thermal history of the Earth's upper mantle: Journal of Geophysical Research: Solid Earth, v. 99, p. 13835–13850.

Abu-Jaber, N.S., and Kimberley, M.M., 1992, Origin of ultramafic-hosted vein magnesite deposits: Ore Geology Reviews, v. 7, p. 155–191.

Aguinis, H., Gottfredson, R.K., and Joo, H., 2013, Best-Practice Recommendations for Defining, Identifying, and Handling Outliers: Organizational Research Methods, v. 16, p. 270–301, doi:10.1177/1094428112470848.

Andréani, M., Mével, C., Boullier, A., and Escartin, J., 2007, Dynamic control on serpentine crystallization in veins: Constraints on hydration processes in oceanic peridotites: Geochemistry, Geophysics, Geosystems, v. 8.

Aoki, K., Fujino, K., and Akaogi, M., 1976, Mineralogy and Petrology Titanoehondrodite and Titanoelinohumite Derived from the Upper Mantle in the Buell Park Kimberlite , Arizona , USA: Contribution to Mineralogy and Petrology, v. 253, p. 243–253.

Appel, P.W.U., Fedo, C.M., Moorbath, S., and Myers, J.S., 1998, Early Archaean Isua supracrustal belt, west Greenland: pilot study of the Isua multidisciplinary research project: Geological Survey of Denmark and Greenland (GEUS) Bulletin, p. 94–99.

Arai, S., 1975, Contact metamorphosed dunite-harzburgite complex in the Chugoku district, western Japan: Contributions to Mineralogy and Petrology, v. 52, p. 1–16, doi:10.1007/BF00377998.

Ashworth, S.R. in O. and the C. of I.S. in S.R., and Chambers, A.D., 2000, Symplectic Reaction in Olivine and the Controls of Intergrowth Spacing in Symplectites: Journal of Petrology, v. 41, p. 285–304, doi:10.1093/petrology/41.2.285.

Baadsgaard, H., Nutman, A.P., Bridgwater, D., Rosing, M., McGregor, V.R., and Allaart, J.H., 1984, The zircon geochronology of the Akilia association and Isua supracrustal belt, West Greenland: Earth and Planetary Science Letters, v. 68, p. 221–228.

Bach, W., Paulick, H., Garrido, C.J., Ildefonse, B., Meurer, W.P., and Humphris, S.E., 2006, Unraveling the sequence of serpentinization reactions: Petrography, mineral chemistry, and petrophysics of serpentinites from MAR 15°N (ODP Leg 209, Site 1274): Geophysical Research Letters, v. 33, p. 4–7, doi:10.1029/2006GL025681.

Bai, Y., Su, B.-X., Xiao, Y., Lenaz, D., Asamoah Sakyi, P., Liang, Z., Chen, C., and Yang, S.-H., 2018, Origin of Reverse Zoned Cr-Spinels from the Paleoproterozoic Yanmenguan Mafic–Ultramafic Complex in the North China Craton: Minerals, v. 8, p. 62, doi:10.3390/min8020062.

Balling, N., 2000, Deep seismic reflection evidence for ancient subduction and collision zones within the continental lithosphere of northwestern Europe: Tectonophysics, v. 329, p. 269–300.

Barnes, S.J., and Roeder, P.L., 2001, The range of spinel compositions in terrestrial mafic and ultramafic rocks: Journal of Petrology, v. 42, p. 2279–2302, doi:10.1093/petrology/42.12.2279.

Bell, P.M., Mao, H.K., RoEDDER, Ed., and Weiblen, P.W., 1975, The problem of the origin of symplectites in olivine-bearing lunar rocks, *in* Lunar and Planetary Science Conference Proceedings, v. 6, p. 231–248.

Bell, D.R., and Rossman, G.R., 1992, The Role of Earth ' s Mantle : Science, v. 255, p. 1391–1397.

Berman, R.G., Engi, M., Greenwood, H.J., and Brown, T.H., 1986, Derivation of Internally-Consistent Thermodynamic Data by the Technique of Mathematical Programming: a Review

with Application the System MgO-SiO2-H2O: Journal of Petrology, v. 27, p. 1331–1364.

Bernstein, S., Kelemen, P.B., and Brooks, C.K., 1998, Depleted spinel harzburgite xenoliths in Tertiary dykes from East Greenland: Restites from high degree melting: Earth and Planetary Science Letters, v. 154, p. 221–235, doi:10.1016/S0012-821X(97)00175-1.

Bjørnerud, M.G., and Austrheim, H., 2004, Inhibited eclogite formation: The key to the rapid growth of strong and buoyant Archean continental crust: Geology, v. 32, p. 765–768, doi:10.1130/G20590.1.

Boak, J.L., and Dymek, R.F., 1982, Metamorphism of the ca. 3800 Ma supracrustal rocks at Isua, West Greenland: implications for early Archaean crustal evolution: Earth and Planetary Science Letters, v. 59, p. 155–176, doi:10.1016/0012-821X(82)90123-6.

Bowring, S.A., Williams, I.S., and Compston, W., 1989, 3.96 Ga gneisses from the slave province, Northwest Territories, Canada: Geology, v. 17, p. 971–975.

Boyd, F.R., Pokhilenko, N.P., Pearson, D.G., Mertzman, S.A., Sobolev, N. V., and Finger, L.W., 1997, Composition of the Siberian cratonic mantle: evidence from Udachnaya peridotite xenoliths: Contributions to Mineralogy and Petrology, v. 128, p. 228–246, doi:10.1007/s004100050305.

Brenker, F.E., Stachel, T., and Harris, J.W., 2002, Exhumation of lower mantle inclusions in diamond: ATEM investigation of retrograde phase transitions, reactions and exsolution: Earth and Planetary Science Letters, v. 198, p. 1–9, doi:10.1016/S0012-821X(02)00514-9.

Bucher, K., and Frey, M., 2002, Definition, Conditions and Types of Metamorphism, *in* Petrogenesis of Metamorphic Rocks, Berlin, Heidelberg, Springer Berlin Heidelberg, p. 3–15, doi:10.1007/978-3-662-04914-3_1.

Chen, Y., Ye, K., Guo, S., Wu, T.F., and Liu, J.B., 2013, Multistage metamorphism of garnet orthopyroxenites from the Maowu mafic-ultramafic complex, Dabieshan UHP terrane, eastern China: International Geology Review, v. 55, p. 1239–1260, doi:10.1080/00206814.2013.772694.

Churakov, S. V., Khisina, N.R., Urusov, V.S., and Wirth, R., 2003, First-principles study of (MgH2SiO4) • n(Mg2SiO4) hydrous olivine structures. I. Crystal structure modelling of hydrous olivine Hy-2a (MgH2SiO4) • 3(Mg2SiO4): Physics and Chemistry of Minerals, v. 30, p. 1–11, doi:10.1007/s00269-002-0288-9.

Cimmino, F., Messiga, B., Piccardo, G.B., and Zeda, O., 1979, Titanian clinohumite-bearing

assemblages within antigorite serpentinites of the Gruppo di Voltri (Western Liguria), inferences on the geodynamic evolution of the Piedmontese ultramafic section: Ofioliti, v. 4, p. 97–120.

Complex, A., Komiya, T., Maruyama, S., Masuda, T., Nohda, S., Hayashi, M., and Okamoto, K., 1999, A RT I C L E S Plate Tectonics at 3 . 8 – 3 . 7 Ga : Field Evidence from the Isua: Sciences-New York, v. 107, p. 515–554.

D'Errico, M.E., Warren, J.M., and Godard, M., 2016, Evidence for chemically heterogeneous Arctic mantle beneath the Gakkel Ridge: Geochimica et Cosmochimica Acta, v. 174, p. 291–312, doi:10.1016/j.gca.2015.11.017.

Debret, B., Andreani, M., Godard, M., Nicollet, C., Schwartz, S., and Lafay, R., 2013a, Trace element behavior during serpentinization/de-serpentinization of an eclogitized oceanic lithosphere: A LA-ICPMS study of the Lanzo ultramafic massif (Western Alps): Chemical Geology, v. 357, p. 117–133, doi:10.1016/j.chemgeo.2013.08.025.

Debret, B., Nicollet, C., Andreani, M., Schwartz, S., and Godard, M., 2013b, Three steps of serpentinization in an eclogitized oceanic serpentinization front (Lanzo Massif - Western Alps): Journal of Metamorphic Geology, v. 31, p. 165–186, doi:10.1111/jmg.12008.

Deschamps, F., Godard, M., Guillot, S., and Hattori, K., 2013, Geochemistry of subduction zone serpentinites: A review: Lithos, v. 178, p. 96–127, doi:10.1016/j.lithos.2013.05.019.

Dick, H.J.B., and Bullen, T., 1984, Chromian spinel as a petrogenetic indicator in abyssal and alpine-type peridotites and spatially associated lavas: Contributions to Mineralogy and Petrology, Volume 86, Issue 1, pp.54-76, v. 86, p. 54–76, doi:10.1007/BF00373711.

Dilek, Y., and Furnes, H., 2013, Evolution of Archean crust and early life: Springer, v. 7.

Downes, H., 2020, Ultramafic Rocks, *in* Reference Module in Earth Systems and Environmental Sciences, Elsevier, doi:10.1016/b978-0-12-409548-9.12478-9.

Duke, J.M., 1976, Distribution of the period four transition elements among olivine, calcic clinopyroxene and mafic silicate liquid: experimental results: Journal of Petrology, v. 17, p. 499–521.

Dymek, R.F., Boak, J.L., and Brothers, S.C., 1988, Titanian chondrodite- and titanian clinohumite-bearing metadunite from the 3800 Ma Isua supracrustal belt West Greenland : Chemistry, petrology, and origin: American Mineralogist, v. 73, p. 547–558.

Elardo, S.M., McCubbin, F.M., and Shearer, C.K., 2012, Chromite symplectites in Mg-suite troctolite 76535 as evidence for infiltration metasomatism of a lunar layered intrusion: Geochimica et

Cosmochimica Acta, v. 87, p. 154–177, doi:10.1016/j.gca.2012.03.030.

Evans, B.W., 2008, Control of the Products of Serpentinization by the Fe2+Mg−1 Exchange Potential of Olivine and Orthopyroxene: Journal of Petrology, v. 49, p. 1873–1887, doi:10.1093/petrology/egn050.

Evans, B.W., 2010, Lizardite versus antigorite serpentinite: Magnetite, hydrogen, and life(?): Geology, v. 38, p. 879–882, doi:10.1130/G31158.1.

Evans, B.W., 1977, Metamorphism of Alpine Peridotite and Serpentinite: Annual Review of Earth and Planetary Sciences, v. 5, p. 397–447, doi:10.1146/annurev.ea.05.050177.002145.

Evans, B.W., 2004, The Serpentinite Multisystem Revisited: Chrysotile Is Metastable: International Geology Review, v. 46, p. 479–506, doi:10.2747/0020-6814.46.6.479.

Evans, B.W., and Frost, B.R., 1975, Chrome-spinel in progressive metamorphism-a preliminary analysis: Geochimica et Cosmochimica Acta, v. 39, p. 959–972, doi:10.1016/0016-7037(75)90041-1.

Evans, B.W., and Trommsdorff, V., 1978, Breakdown of titanoclinohumite in contact and regional metamorphism, Central Alps, *in* TRANSACTIONS-AMERICAN GEOPHYSICAL UNION, AMER GEOPHYSICAL UNION 2000 FLORIDA AVE NW, WASHINGTON, DC 20009, v. 59, p. 407.

Field, S.W., 2008, Diffusion, discontinuous precipitation, metamorphism, and metasomatism: The complex history of South African upper-mantle symplectites: American Mineralogist, v. 93, p. 618–631, doi:10.2138/am.2008.2626.

Fischer, R., and Gerya, T., 2016, Regimes of subduction and lithospheric dynamics in the Precambrian: 3D thermomechanical modelling: Gondwana Research, v. 37, p. 53–70.

Frei, R., Bridgwater, D., Rosing, M., and Stecher, O., 1999, Controversial Pb-Pb and Sm-Nd isotope results in the early Archean Isua (West Greenland) oxide iron formation: Preservation of primary signatures versus secondary disturbances: Geochimica et Cosmochimica Acta, v. 63, p. 473–488.

Freitas Suita, M.T. De, and Strieder, A.J., 1996, Cr-Spinels from Brazilian Mafic-Ultramafic Complexes: Metamorphic Modifications: International Geology Review, v. 38, p. 245–267, doi:10.1080/00206819709465333.

Frezzotti, M.L., Tecce, F., and Casagli, A., 2012, Raman spectroscopy for fluid inclusion analysis: Journal of Geochemical Exploration, v. 112, p. 1–20, doi:10.1016/j.gexplo.2011.09.009.

Friend, C.R.L., and Nutman, A.P., 2011, Dunites from Isua, Greenland: A ca. 3720 Ma window into subcrustal metasomatism of depleted mantle: Geology, v. 39, p. 663–666, doi:10.1130/G31904.1.

Frost, B.R., 1975, Contact metamorphism of serpentinite, chloritic blackwall and rodingite at paddy-go-easy pass, central cascades, Washington: Journal of Petrology, v. 16, p. 272–313, doi:10.1093/petrology/16.1.272.

Fujino, K., and Takeuchi, Y., 1978, Crystal chemistry of titanian chondrodite and titanian clinohumite of high-pressure origin: American Mineralogist, v. 63, p. 535–543, https://pubs.geoscienceworld.org/msa/ammin/article/73/5-6/547/105004/titanian-chondrodite-and-titanian-clinohumite (accessed July 2019).

Furnes, H. et al., 2009, Isua supracrustal belt (Greenland)-A vestige of a 3.8 Ga suprasubduction zone ophiolite, and the implications for Archean geology: Lithos, v. 113, p. 115–132, doi:10.1016/j.lithos.2009.03.043.

Furnes, H., De Wit, M., Staudigel, H., Rosing, M., and Muehlenbachs, K., 2007, A vestige of earth's oldest ophiolite: Science, v. 315, p. 1704–1707, doi:10.1126/science.1139170.

Garde, A.A., 1997, Accretion and evolution of an Archaean high-grade grey gneiss – amphibolite complex: the Fiskefjord area, southern West Greenland: v. 177, 115 p., doi:10.1007/978-1-4614-8757-9.

Garde, A.A., Friend, C.R.L.L., Nutman, A.P.R.P.R., and Marker, M., 2000, Rapid maturation and stabilisation of middle Archaean continental crust: The Akia terrane, southern West Greenland: Bulletin of the Geological Society of Denmark, v. 47, p. 1–27.

Garrido, C.J., López Sánchez-Vizcaíno, V., Gómez-Pugnaire, M.T., Trommsdorff, V., Alard, O., Bodinier, J.-L., and Godard, M., 2005, Enrichment of HFSE in chlorite-harzburgite produced by high-pressure dehydration of antigorite-serpentinite: Implications for subduction magmatism: Geochemistry, Geophysics, Geosystems, v. 6, p. n/a-n/a, doi:10.1029/2004GC000791.

Gerya, T., 2019, Geodynamics of the early Earth: Quest for the missing paradigm: Geology, v. 47, p. 1006–1007, doi:10.1130/focus102019.1.

Gerya, T. V., Stern, R.J., Baes, M., Sobolev, S. V., and Whattam, S.A., 2015, Plate tectonics on the Earth triggered by plume-induced subduction initiation: Nature, v. 527, p. 221–225, doi:10.1038/nature15752.

González-Jiménez, J.M. et al., 2017, Titanian clinohumite and chondrodite in antigorite serpentinites

from Central Chile: evidence for deep and cold subduction: European Journal of Mineralogy, v. 29, p. 959–970, doi:10.1127/ejm/2017/0029-2668.

Goodwin, A.M., 1991, Archean Crust, *in* Precambrian Geology, Elsevier, p. 79–232, doi:10.1016/b978-0-12-289870-9.50007-2.

Gruau, G., Rosing, M., Bridgwater, D., and Gill, R.C.O., 1996, Resetting of Sm□ Nd systematics during metamorphism of> 3.7-Ga rocks: implications for isotopic models of early Earth differentiation: Chemical Geology, v. 133, p. 225–240.

Grützner, T., Klemme, S., Rohrbach, A., Gervasoni, F., and Berndt, J., 2017, The role of F-clinohumite in volatile recycling processes in subduction zones: Geology, v. 45, p. 443–446, doi:10.1130/G38788.1.

Hacker, B.R., Calvert, A., Zhang, R.Y., Ernst, W.G., and Liou, J.G., 2003, Ultrarapid exhumation of ultrahigh-pressure diamond-bearing metasedimentary rocks of the Kokchetav Massif, Kazakhstan? Lithos, v. 70, p. 61–75, doi:10.1016/S0024-4937(03)00092-6.

Hanghøj, K., Kelemen, P.B., Hassler, D., and Godard, M., 2010, Composition and genesis of depleted mantle peridotites from the Wadi Tayin Massif, Oman Ophiolite; major and trace element geochemistry, and Os isotope and PGE systematics: Journal of Petrology, v. 51, p. 201–227.

Harland, W.B., Armstrong, R.L., Cox, A. V, Craig, L.E., Smith, A.G., and Smith, D.G., 1990, A geologic time scale 1989: Cambridge University Press.

Harrison, T.M., Blichert-Toft, J., Müller, W., Albarede, F., Holden, P., and Mojzsis, S.J., 2005, Heterogeneous Hadean hafnium: evidence of continental crust at 4.4 to 4.5 Ga: Science, v. 310, p. 1947–1950.

Hattori, K.H., and Guillot, S., 2003, Volcanic fronts form as a consequence of serpentinite dehydration in the forearc mantle wedge: Geology, v. 31, p. 525–528, doi:10.1130/0091-7613(2003)031<0525:vffaac>2.0.co;2.

Henderson, P., and Wood, R.J., 1982, Reaction relationships of chrome-spinels in igneous rocks - further evidence from the layered intrusions of Rhum and Mull, Inner Hebrides, Scotland: Contributions to Mineralogy and Petrology, v. 78, p. 225–229, doi:10.1007/BF00398917.

Hermann, J., Fitz Gerald, J.D., Malaspina, N., Berry, A.J., and Scambelluri, M., 2007, OH-bearing planar defects in olivine produced by the breakdown of Ti-rich humite minerals from Dabie Shan (China): Contributions to Mineralogy and Petrology, v. 153, p. 417–428, doi:10.1007/s00410-006-0155-7.

De Hoog, J.C.M., Hattori, K., and Jung, H., 2014, Titanium- and water-rich metamorphic olivine in high-pressure serpentinites from the Voltri Massif (Ligurian Alps, Italy): Evidence for deep subduction of high-field strength and fluid-mobile elements: Contributions to Mineralogy and Petrology, v. 167, p. 1–15, doi:10.1007/s00410-014-0990-x.

Hulbert, L.J., and Von Gruenewaldt, G., 1985, Textural and compositional features of chromite in the lower and critical zones of the Bushveld Complex south of Potgietersrus: Economic Geology, v. 80, p. 872–895.

van Hunen, J., and Moyen, J.-F., 2012, Archean Subduction: Fact or Fiction? Annual Review of Earth and Planetary Sciences, v. 40, p. 195–219, doi:10.1146/annurev-earth-042711-105255.

Hwang, S.L., Yui, T.F., Chu, H.T., Shen, P., Iizuka, Y., Yang, H.Y., Yang, J., and Xu, Z., 2008, Hematite and magnetite precipitates in olivine from the Sulu peridotite: A result of dehydrogenation-oxidation reaction of mantle olivine? American Mineralogist, v. 93, p. 1051–1060, doi:10.2138/am.2008.2784.

Ishii, T., Robinson, P.T., Maekawa, H., and Fiske, R., 1992, Petrological studies of peridotites from diapiric serpentinite seamounts in the Izu-Ogasawara-Mariana forearc, Leg 125, *in* Proceedings of the ocean drilling program, scientific results, Ocean Drilling Program College Station, v. 125.

Ito, M., and Ganguly, J., 2006, Diffusion kinetics of Cr in olivine and 53Mn-53Cr thermochronology of early solar system objects: Geochimica et Cosmochimica Acta, v. 70, p. 799–809, doi:10.1016/j.gca.2005.09.020.

Iwamori, H., 2004, Phase relations of peridotites under H2O-saturated conditions and ability of subducting plates for transportation of H2O: Earth and Planetary Science Letters, v. 227, p. 57–71, doi:10.1016/j.epsl.2004.08.013.

Jones, N.W., 1969, Crystallographic nomenclature and twinning in the humite minerals: American Mineralogist, v. 54, p. 309–313, http://dx.doi.org/.

Kaczmarek, M.A., Reddy, S.M., Nutman, A.P., Friend, C.R.L., and Bennett, V.C., 2016, Earth's oldest mantle fabrics indicate Eoarchaean subduction: Nature Communications, v. 7, p. 10665, doi:10.1038/ncomms10665.

Kawamoto, T., Hervig, R.L., and Holloway, J.R., 1996, Experimental evidence for a hydrous transition zone in the early Earth's mantle: Earth and Planetary Science Letters, v. 142, p. 587–592, doi:10.1016/0012-821x(96)00113-6.

Kelemen, P.B., Hart, S.R., and Bernstein, S., 1998, Silica enrichment in the continental upper mantle

via melt/rock reaction: Earth and Planetary Science Letters, v. 164, p. 387–406, doi:10.1016/S0012-821X(98)00233-7.

Kelemen, P.B., and Matter, J., 2008, In situ carbonation of peridotite for CO2 storage: Proceedings of the National Academy of Sciences of the United States of America, v. 105, p. 17295–17300, doi:10.1073/pnas.0805794105.

Kelemen, P.B., and Miller, D.J., 2004, Proceedings of the Ocean Drilling Program [electronic resource].: drilling mantle peridotite along the Mid-Atlantic Ridge from 14 [degrees] to 16 [degrees] N; covering leg 209 of the cruises of the drilling vessel JOIDES Resolution; Rio de Janeiro, Brazil: Texas A&M University.

Kent, A.J.R., and Rossman, G.R., 2002, Hydrogen, lithium, and boron in mantle-derived olivine: The role of coupled substitutions: American Mineralogist, v. 87, p. 1432–1436, doi:10.2138/am-2002-1020.

Khedr, M.Z., and Arai, S., 2013, Origin of Neoproterozoic ophiolitic peridotites in south Eastern Desert, Egypt, constrained from primary mantle mineral chemistry: Mineralogy and Petrology, v. 107, p. 807–828, doi:10.1007/s00710-012-0213-y.

Khedr, M.Z., and Arai, S., 2012, Petrology and geochemistry of prograde deserpentinized peridotites from Happo-O'ne, Japan: Evidence of element mobility during deserpentinization: Journal of Asian Earth Sciences, v. 43, p. 150–163, doi:10.1016/j.jseaes.2011.08.017.

Khisina, N.R., and Lorenz, C.A., 2015, Dehydrogenation as the mechanism of formation of the oriented spinel-pyroxene symplectites and magnetite-hematite inclusions in terrestrial and extraterrestrial olivines: Petrology, v. 23, p. 176–188, doi:10.1134/S086959111502006X.

Khisina, N.R., and Wirth, R., 2002, Hydrous olivine in mantle olivine: Physics and Chemistry of Minerals, v. 29, p. 98–111, doi:10.1007/s002690100205.

Khisina, N.R., Wirth, R., Abart, R., Rhede, D., and Heinrich, W., 2013, Oriented chromite-diopside symplectic inclusions in olivine from lunar regolith delivered by " Luna-24" mission: Geochimica et Cosmochimica Acta, v. 104, p. 84–98, doi:10.1016/j.gca.2012.10.050.

Khisina, N., Wirth, R., Matsyuk, S., and Koch-Müller, M., 2008, Microstructures and OH-bearing nano-inclusions in "wet" olivine xenocrysts from the Udachnaya kimberlite: European Journal of Mineralogy, v. 20, p. 1067–1078, doi:10.1127/0935-1221/2008/0020-1799.

Klein, F., Bach, W., Humphris, S.E., Kahl, W.A., Jöns, N., Moskowitz, B., and Berquó, T.S., 2014, Magnetite in seafloor serpentinite-Some like it hot: Geology, v. 42, p. 135–138,

doi:10.1130/G35068.1.

Klein, F., and Garrido, C.J., 2011, Thermodynamic constraints on mineral carbonation of serpentinized peridotite: Lithos, v. 126, p. 147–160, doi:10.1016/j.lithos.2011.07.020.

Klein, F., and McCollom, T.M., 2013, From serpentinization to carbonation: New insights from a CO2 injection experiment: Earth and Planetary Science Letters, v. 379, p. 137–145, doi:10.1016/j.epsl.2013.08.017.

Komiya, T., Hayashi, M., Maruyama, S., and Yurimoto, H., 2002, Intermediate-P/T type Archean metamorphism of the Isua supracrustal belt: Implications for secular change of geothermal gradients at subduction zones and for Archean plate tectonics: American Journal of Science, v. 302, p. 806–826, doi:10.2475/ajs.302.9.806.

Komiya, T., Maruyama, S., Masuda, T., Nohda, S., Hayashi, M., and Okamoto, K., 1999, Plate Tectonics at 3.8–3.7 Ga: Field Evidence from the Isua Accretionary Complex, Southern West Greenland: The Journal of Geology, v. 107, p. 515–554, doi:10.1086/314371.

Kushiro, I., and Yoder Jr, H.S., 1966, Anorthite—forsterite and anorthite—enstatite reactions and their bearing on the basalt—eclogite transformation: Journal of Petrology, v. 7, p. 337–362.

Lafuente, B., Downs, R.T., Yang, H., and Stone, N., 2016, The power of databases: The RRUFF project, *in* Highlights in Mineralogical Crystallography, Berlin, München, Boston, Walter de Gruyter GmbH, p. 1–29, doi:10.1515/9783110417104-003.

Larsen, J.G., 1982, Mantle-derived dunite and lherzolite nodules from Ubekendt Ejland, west Greenland Tertiary province: Mineralogical Magazine, v. 46, p. 329–336.

López Sánchez-Vizcaíno, V., Trommsdorff, V., Gómez-Pugnaire, M.T., Garrido, C.J., Müntener, O., and Connolly, J.A.D., 2005, Petrology of titanian clinohumite and olivine at the high-pressure breakdown of antigorite serpentinite to chlorite harzburgite (Almirez Massif, S. Spain): Contributions to Mineralogy and Petrology, v. 149, p. 627–646, doi:10.1007/s00410-005-0678-3.

Markl, G., Marks, M., and Wirth, R., 2001, The influence of T, aSiO2, and fo2 on exsolution textures in Fe-Mg olivine: An example from augite syenites of the Ilimaussaq Intrussion, South Greenland: American Mineralogist, v. 86, p. 36–46, doi:10.2138/am-2001-0105.

Marshak, S., 2005, Earth: portrait of a planet vol 1:

Maruyama, S., 1991, The oldest accretionary complex on the Earth, Isua, Greenland: Geological Society of America, v. 23, p. A429–A430.

McCaig, A.M., Titarenko, S.S., Savov, I.P., Cliff, R.A., Banks, D., Boyce, A., and Agostini, S., 2018, No significant boron in the hydrated mantle of most subducting slabs: Nature Communications, v. 9, p. 1–10, doi:10.1038/s41467-018-07064-6.

McDonough, W.F., and Sun, S. s., 1995, The composition of the Earth: Chemical Geology, v. 120, p. 223–253, doi:10.1016/0009-2541(94)00140-4.

Mcgregor, V.R., Friend, C.R.L., and Nutman, A.P., 1991, The late Archaean mobile belt through Godthåbsfjord, southern West Greenland: a continent-continent collision zone? Bull. geol. Soc. Denmark, v. 39, p. 179–197, https://2dgf.dk/xpdf/bull39-03-04-179-197.pdf (accessed June 2018).

McGregor, V.R., and Mason, B., 1977, Petrogenesis and geochemistry of metabasaltic and metasedimentary enclaves in the Amitsoq gneisses, West Greenland: American Mineralogist, v. 62, p. 887–904.

Mikouchi, T., Yamada, I., and Miyamoto, M., 2000, Symplectic exsolution in olivine from the Nakhla martian meteorite: Meteoritics and Planetary Science, v. 35, p. 937–942, doi:10.1111/j.1945-5100.2000.tb01483.x.

Möckel, J.R., 1969, Structural petrology of the garnet-peridotite of Alpe Arami (Ticino, Switzerland): Leidse Geologische Mededelingen, v. 42, p. 61–130.

Moseley, D., 1984, Symplectic exsolution in olivine: American Mineralogist, v. 69, p. 139–153.

Nisbet, E.G., and Fowler, C.M.R., 1983, Model for Archean plate tectonics: Geology, v. 11, p. 376–379.

Nishio, I. et al., 2019, Titanian Clinohumite-Bearing Peridotite from the Ulamertoq Ultramafic Body in the 3.0 Ga Akia Terrane of Southern West Greenland: Geosciences 2019, Vol. 9, Page 153, v. 9, p. 153, doi:10.3390/GEOSCIENCES9040153.

Niu, Y., 2004, Bulk-rock major and trace element compositions of abyssal peridotites: Implications for mantle melting, melt extraction and post-melting processes beneath Mid-Ocean ridges: Journal of Petrology, v. 45, p. 2423–2458, doi:10.1093/petrology/egh068.

Noffke, N., Christian, D., Wacey, D., and Hazen, R.M., 2013, Microbially induced sedimentary structures recording an ancient ecosystem in the ca. 3.48 Billion-year-old dresser formation, pilbara, Western Australia: Astrobiology, v. 13, p. 1103–1124, doi:10.1089/ast.2013.1030.

Nozaka, T., 2003, Compositional heterogeneity of olivine in thermally metamorphosed serpentinite from Southwest Japan: American Mineralogist, v. 88, p. 1377–1384, doi:10.2138/am-2003-8-

922.

Nozaka, T., 2005, Metamorphic history of serpentinite mylonites from the Happo ultramafic complex, central Japan: Journal of Metamorphic Geology, v. 23, p. 711–723, doi:10.1111/j.1525-1314.2005.00605.x.

Nozaka, T., and Shibata, T., 1995, Mineral paragenesis in thermally metamorphosed serpentinites, Ohsa-yama, Okayama Prefecture.: Okayama University Earth Science Reports, v. 2, p. 1–11.

Nutman, A.P., Allaart, J.H., Bridgwater, D., Dimroth, E., and Rosing, M., 1984, Stratigraphic and geochemical evidence for the depositional environment of the early archaean isua supracrustal belt, southern west greenland: Precambrian Research, v. 25, p. 365–396, doi:10.1016/0301-9268(84)90010-X.

Nutman, A.P., Bennett, V.C., Friend, C.R.L., and Yi, K., 2020, Eoarchean contrasting ultra-high-pressure to low-pressure metamorphisms (<250 to >1000 °C/GPa) explained by tectonic plate convergence in deep time: Precambrian Research, v. 344, p. 105770, doi:10.1016/j.precamres.2020.105770.

Nutman, A.P., and Friend, C.R.L., 2009, New 1:20,000 scale geological maps, synthesis and history of investigation of the Isua supracrustal belt and adjacent orthogneisses, southern West Greenland: A glimpse of Eoarchaean crust formation and orogeny: Precambrian Research, v. 172, p. 189–211, doi:10.1016/j.precamres.2009.03.017.

Nutman, A.P., Friend, C.R.L., and Paxton, S., 2009, Detrital zircon sedimentary provenance ages for the Eoarchaean Isua supracrustal belt southern West Greenland: Juxtaposition of an imbricated ca. 3700 Ma juvenile arc against an older complex with 3920-3760 Ma components: Precambrian Research, v. 172, p. 212–233, doi:10.1016/j.precamres.2009.03.019.

Nutman, A.P., McGregor, V.R., Friend, C.R.L., Bennett, V.C., and Kinny, P.D., 1996a, The Itsaq Gneiss Complex of southern West Greenland; the world's most extensive record of early crustal evolution (3900-3600 Ma): Precambrian Research, v. 78, p. 1–39, doi:10.1016/0301-9268(95)00066-6.

Nutman, A.P., McGregor, V.R., Friend, C.R.L., Bennett, V.C., and Kinny, P.D., 1996b, The Itsaq Gneiss Complex of southern West Greenland; the world's most extensive record of early crustal evolution (3900-3600 Ma): Precambrian Research, v. 78, p. 1–39, doi:10.1016/0301-9268(95)00066-6.

O'Hanley, D.S., 1996, Serpentinites: records of tectonic and petrological history: Oxford University Press on Demand.

O'Neil, J., Carlson, R.W., Francis, D., and Stevenson, R.K., 2008, Neodymium-142 evidence for hadean mafic crust: Science, v. 321, p. 1828–1831, doi:10.1126/science.1161925.

Padrón-Navarta, J.A., Lopez Sanchez-Vizcaino, V., Garrido, C.J., and Gómez-Pugnaire, M.T., 2011, Metamorphic record of high-pressure dehydration of antigorite serpentinite to chlorite harzburgite in a subduction setting (Cerro del Almirez, Nevado–Filábride Complex, Southern Spain): Journal of Petrology, v. 52, p. 2047–2078.

Padrón-Navarta, J.A., Sánchez-Vizcaíno, V.L., Hermann, J., Connolly, J.A.D., Garrido, C.J., Gómez-Pugnaire, M.T., and Marchesi, C., 2013, Tschermak's substitution in antigorite and consequences for phase relations and water liberation in high-grade serpentinites: Lithos, v. 178, p. 186–196, doi:10.1016/j.lithos.2013.02.001.

Petriglieri, J.R., Salvioli-Mariani, E., Mantovani, L., Tribaudino, M., Lottici, P.P., Laporte-Magoni, C., and Bersani, D., 2015, Micro-Raman mapping of the polymorphs of serpentine: Journal of Raman Spectroscopy, v. 46, p. 953–958, doi:10.1002/jrs.4695.

Plümper, O., Piazolo, S., and Austrheim, H., 2012, Olivine pseudomorphs after serpentinized orthopyroxene record transient oceanic lithospheric mantle dehydration (Leka Ophiolite complex, Norway): Journal of Petrology, v. 53, p. 1943–1968, doi:10.1093/petrology/egs039.

Purvis, A.C., Nesbitt, R.W., and Hallberg, J.A., 1972, The Geology of Part of the Carr Boyd Rocks Complex and Its Associated Nickel Mineralization, Western Australia: Economic Geology, v. 67, p. 1093–1113, doi:10.2113/gsecongeo.67.8.1093.

Ribbe, P.H., 1979, Titanium, fluorine, and hydroxyl in the humite minerals: American Mineralogist, v. 64, p. 1027.

Rollinson, H., 2002a, A Metamorphosed, Early Archaean Chromitite from West Greenland: Implications for the Genesis of Archaean Anorthositic Chromitites: Journal of Petrology, v. 43, p. 2143–2170, doi:10.1093/petrology/43.11.2143.

Rollinson, H., 2007, Recognising early Archaean mantle: A reappraisal: Contributions to Mineralogy and Petrology, v. 154, p. 241–252, doi:10.1007/s00410-007-0191-y.

Rollinson, H., 2002b, The metamorphic history of the Isua Greenstone Belt, West Greenland: Geological Society Special Publication, v. 199, p. 329–350, doi:10.1144/GSL.SP.2002.199.01.16.

Rose, N.M., Rosing, Minik, T., Bridgwater, D., Rosing, M.T., and Bridgwater, D., 1996, The origin of metacarbonate rocks in the archaean Isua supracrustal belt, west Greenland: v. 296, p. 1004–

1044, doi:10.2475/ajs.296.9.1004.

Rosing, M.T., 1989, Metasomatic Alteration of Ultramafic Rocks, *in* Fluid Movements — Element Transport and the Composition of the Deep Crust, Kluwer Academic Publishers, p. 187–202, doi:10.1007/978-94-009-0991-5_17.

Salters, V.J.M., and Stracke, A., 2004, Composition of the depleted mantle: Geochemistry, Geophysics, Geosystems, v. 5, p. 209–229, doi:10.1029/2003GC000597.

Sand, K.K., Waight, T.E., Pearson, D.G., Nielsen, T.F.D.D., Makovicky, E., and Hutchison, M.T., 2009, The lithospheric mantle below southern West Greenland: A geothermobarometric approach to diamond potential and mantle stratigraphy: Lithos, v. 112, p. 1155–1166, doi:10.1016/j.lithos.2009.05.012.

Sano, T., Fukuoka, T., and Ishimoto, M., 2011, Petrological constraints on magma evolution of the Fuji volcano: A case study for the 1707 Hoei eruption: Memoirs of the National Museum of Nature and Science, v. 47, p. 471–496, https://www.researchgate.net/publication/285141791_Petrological_constraints_on_magma_evolution_of_the_Fuji_volcano_A_case_study_for_the_1707_Hoei_eruption (accessed May 2020).

Scambelluri, M., Bottazzi, P., Trommsdorff, V., Vannucci, R., Hermann, J., Gòmez-Pugnaire, M.T., and Lòpez-Sànchez Vizcano, V., 2001, Incompatible element-rich fluids released by antigorite breakdown in deeply subducted mantle: Earth and Planetary Science Letters, v. 192, p. 457–470, doi:10.1016/S0012-821X(01)00457-5.

Scambelluri, M., Fiebig, J., Malaspina, N., Müntener, O., and Pettke, T., 2004, Serpentinite Subduction: Implications for Fluid Processes and Trace-Element Recycling: International Geology Review, v. 46, p. 595–613, doi:10.2747/0020-6814.46.7.595.

Scambelluri, M., Muntener, O., Hermann, J., Piccardo, G.B., and Trommsdorff, V., 1995, Subduction of water into the mantle: history of an Alpine peridotite: Geology, v. 23, p. 459–462, doi:10.1130/0091-7613(1995)023<0459:SOWITM>2.3.CO;2.

Scambelluri, M., and Rampone, E., 1999, Mg-metasomatism of oceanic gabbros and its control on Ti-clinohumite formation during eclogitization: Contributions to Mineralogy and Petrology, v. 135, p. 1–17, doi:10.1007/s004100050494.

Schmidberger, S.S., and Francis, D., 1999, Nature of the mantle roots beneath the North American craton: mantle xenolith evidence from Somerset Island kimberlites: Lithos, v. 48, p. 195–216, doi:https://doi.org/10.1016/S0024-4937(99)00029-8.

Schwartz, S., Guillot, S., Reynard, B., Lafay, R., Debret, B., Nicollet, C., Lanari, P., and Auzende, A.L., 2013, Pressure-temperature estimates of the lizardite/antigorite transition in high pressure serpentinites: Lithos, v. 178, p. 197–210, doi:10.1016/j.lithos.2012.11.023.

Shen, T., Hermann, J., Zhang, L., Lü, Z., Padrón-Navarta, J.A., Xia, B., and Bader, T., 2015, UHP metamorphism documented in Ti-chondrodite- and Ti-clinohumite-bearing serpentinized ultramafic rocks from Chinese southwestern Tianshan: Journal of Petrology, v. 56, p. 1425–1458, doi:10.1093/petrology/egv042.

Sizova, E., Gerya, T., Brown, M., and Perchuk, L.L., 2010, Subduction styles in the Precambrian: insight from numerical experiments: Lithos, v. 116, p. 209–229.

Skogby, H., 2006, Water in natural mantle minerals I: Pyroxenes: Reviews in Mineralogy and Geochemistry, v. 62, p. 155–167.

Smith, D., 1977, Titanochondrodite and titanoclinohumite derived from the upper mantle in the Buell Park kimberlite, Arizona, USA - A discussion: Contributions to Mineralogy and Petrology, v. 61, p. 213–215, doi:10.1007/BF00374369.

Smithies, R.H., Champion, D.C., and Cassidy, K.F., 2003, Formation of Earth's early Archaean continental crust, *in* Precambrian Research, Elsevier B.V., v. 127, p. 89–101, doi:10.1016/S0301-9268(03)00182-7.

Sobolev, S. V, and Brown, M., 2019, Surface erosion events controlled the evolution of plate tectonics on Earth: Nature, v. 570, p. 52–57.

Spear, F.S., 1993, Metamorphic phase equilibria and pressure-temperature-time paths: Mineralogical Society of America Washington, DC, v. 1.

Sun, S. -s., and McDonough, W.F., 1989, Chemical and isotopic systematics of oceanic basalts: implications for mantle composition and processes: Geological Society, London, Special Publications, v. 42, p. 313–345, doi:10.1144/GSL.SP.1989.042.01.19.

Szilas, K., van Hinsberg, V., McDonald, I., Næraa, T., Rollinson, H., Adetunji, J., and Bird, D., 2018a, Highly refractory Archaean peridotite cumulates: Petrology and geochemistry of the Seqi Ultramafic Complex, SW Greenland: Geoscience Frontiers, v. 9, p. 689–714, doi:10.1016/j.gsf.2017.05.003.

Szilas, K., van Hinsberg, V., McDonald, I., Næraa, T., Rollinson, H., Adetunji, J., and Bird, D., 2018b, Highly refractory Archaean peridotite cumulates: Petrology and geochemistry of the Seqi Ultramafic Complex, SW Greenland: Geoscience Frontiers, v. 9, p. 689–714,

doi:10.1016/j.gsf.2017.05.003.

Szilas, K., Kelemen, P.B., and Rosing, M.T., 2015, The petrogenesis of ultramafic rocks in the >3.7Ga Isua supracrustal belt, southern West Greenland: Geochemical evidence for two distinct magmatic cumulate trends: Gondwana Research, v. 28, p. 565–580, doi:10.1016/j.gr.2014.07.010.

Takahashi, E., 1980, Thermal history of iherzolite xenoliths—I. Petrology of iherzolite xenoliths from the ichinomegata crater, oga peninsula, northeast Japan: Geochimica et Cosmochimica Acta, v. 44, p. 1643–1658.

Thompson, J.B., 1978, Biopyriboles and polysomatic series: American Mineralogist, v. 63, p. 239–249.

Trommsdorff, V., and Evans, B.W., 1972, Progressive metamorphism of antigorite schist in the Bergell tonalite aureole (Italy): American Journal of Science, v. 272, p. 423–437, doi:10.2475/ajs.272.5.423.

Trommsdorff, V., and Evans, B.W., 1980, Titanian hydroxyl-clinohumite: Formation and breakdown in antigorite rocks (Malenco, Italy): Contributions to Mineralogy and Petrology, v. 72, p. 229–242, doi:10.1007/BF00376142.

Trommsdorff, V., López Sánchez-Vizcaíno, V., Gómez-Pugnaire, M.T., and Müntener, O., 1998, High pressure breakdown of antigorite to spinifex-textured olivine and orthopyroxene, SE Spain: Contributions to Mineralogy and Petrology, v. 132, p. 139–148, doi:10.1007/s004100050412.

Ulmer, P., and Trommsdorff, V., 1995, Serpentine stability to mantle depths and subduction-related magmatism: Science, v. 268, p. 858–861, doi:10.1126/science.268.5212.858.

Vance, J.A., and Dungan, M.A., 1977, Formation of peridotites by deserpentinization in the Darrington and Sultan areas, Cascade Mountains, Washington: Bulletin of the Geological Society of America, v. 88, p. 1497–1508, doi:10.1130/0016-7606(1977)88<1497:FOPBDI>2.0.CO;2.

Vrijmoed, J.C., Van Roermund, H.L.M., and Davies, G.R., 2006, Evidence for diamond-grade ultra-high pressure metamorphism and fluid interaction in the Svartberget Fe-Ti garnet peridotite-websterite body, Western Gneiss Region, Norway: Mineralogy and Petrology, v. 88, p. 381–405, doi:10.1007/s00710-006-0160-6.

Warren, J.M., 2016, Global variations in abyssal peridotite compositions: Lithos, v. 248–251, p. 193–219, doi:10.1016/j.lithos.2015.12.023.

Weiss, M., 1997, Clinohumites: a field and experimental study. PhD Thesis. ETH, Zurich, pp 168: Dissertation, ETH, v. No. 12202, p. 168.

Wilde, S.A., Valley, J.W., Peck, W.H., and Graham, C.M., 2001, Evidence from detrital zircons for the existence of continental crust and oceans on the Earth 4.4 Gyr ago: Nature, v. 409, p. 175–178, doi:10.1038/35051550.

Yamamoto, K., and Akimoto, S.I., 1974, High pressure and high temperature investigations in the system MgOSiO2H2O: Journal of Solid State Chemistry, v. 9, p. 187–195, doi:10.1016/0022-4596(74)90073-5.

Yang, J.J., 2003, Titanian clinohumite - garnet - pyroxene rock from the Su-Lu UHP metamorphic terrane, China: Chemical evolution and tectonic implications: Lithos, v. 70, p. 359–379, doi:10.1016/S0024-4937(03)00106-3.

Yufeng, R., Fangyuan, C., Jingsui, Y., and Yuanhong, G., 2010, Exsolutions of Diopside and Magnetite in Olivine from Mantle Dunite, Luobusa Ophiolite, Tibet, China: Acta Geologica Sinica - English Edition, v. 82, p. 377–384, doi:10.1111/j.1755-6724.2008.tb00587.x.

Zhang, R.Y., Shu, J.F., Mao, H.K., and Liou, J.G., 1999, Magnetite lamellae in olivine and clinohumite from Dabie UHP ultramafic rocks, central China: American Mineralogist, v. 84, p. 564–569, doi:https://doi.org/10.2138/am-1999-0410.

10. TABLES

Table 1. Major-element mineral chemistry of olivine from Lens B metadunites.

Sample	194896 CPL							
Mineral	olivine	olivine	olivine	olivine	olivine	olivine	olivine	olivine
Position	clear	clear	clear	clear	clear	clear	clear	clear
SiO_2	41.48	41.38	41.28	41.09	41.43	42.03	41.99	41.72
TiO_2	0.00	0.01	0.00	0.01	0.02	0.00	0.03	0.00
Al_2O_3	0.00	0.00	0.00	0.00	0.00	0.00	0.00	0.00
Cr_2O_3	0.00	0.00	0.00	0.00	0.00	0.00	0.00	0.00
FeO*	3.25	3.12	3.38	3.03	3.33	2.68	3.69	3.41
MnO	0.19	0.14	0.21	0.14	0.18	0.12	0.21	0.18
MgO	54.64	54.23	54.50	54.84	54.14	54.84	54.23	53.71
CaO	0.00	0.00	0.00	0.00	0.00	0.00	0.01	0.00
Na_2O	0.00	0.00	0.00	0.00	0.00	0.00	0.00	0.00
K_2O	0.01	0.02	0.02	0.01	0.03	0.03	0.02	0.02
NiO	0.53	0.52	0.50	0.44	0.52	0.52	0.55	0.54
Total	100.10	99.40	99.90	99.56	99.64	100.23	100.73	99.57
Mg#	0.97	0.97	0.97	0.97	0.97	0.97	0.96	0.97
Si	0.99	0.99	0.99	0.98	0.99	1.00	1.00	1.00
Ti	0.00	0.00	0.00	0.00	0.00	0.00	0.00	0.00
Al	0.00	0.00	0.00	0.00	0.00	0.00	0.00	0.00
Cr	0.00	0.00	0.00	0.00	0.00	0.00	0.00	0.00
Fe*	0.06	0.06	0.07	0.06	0.07	0.05	0.07	0.07
Mn	0.00	0.00	0.00	0.00	0.00	0.00	0.00	0.00
Mg	1.94	1.94	1.94	1.96	1.93	1.94	1.92	1.92
Ca	0.00	0.00	0.00	0.00	0.00	0.00	0.00	0.00
Na	0.00	0.00	0.00	0.00	0.00	0.00	0.00	0.00
K	0.00	0.00	0.00	0.00	0.00	0.00	0.00	0.00
Ni	0.01	0.01	0.01	0.01	0.01	0.01	0.01	0.01
Total	3.01	3.01	3.01	3.02	3.01	3.00	3.00	3.00

Normalized to 4 oxygens

Table 1 continued

Sample	194903									
Mineral	olivine	olivine	olivine	olivine	olivine	olivine	olivine	olivine	olivine	olivine
Position	dusty	dusty	dusty	dusty	dusty	dusty	dusty	dusty	dusty	clear
SiO_2	41.69	41.73	41.65	41.84	41.40	41.61	41.20	41.78	41.53	42.59
TiO_2	0.00	0.00	0.01	0.00	0.00	0.00	0.01	0.00	0.00	0.02
Al_2O_3	0.00	0.01	0.00	0.01	0.00	0.00	0.01	0.00	0.01	0.03
Cr_2O_3	0.00	0.00	0.00	0.00	0.00	0.00	0.00	0.00	0.00	0.00
FeO*	2.62	3.35	2.54	2.60	2.71	2.71	2.86	2.78	2.68	2.28
MnO	0.21	0.48	0.45	0.49	0.47	0.41	0.51	0.38	0.27	0.10
MgO	54.52	54.33	54.39	54.45	54.22	54.41	53.91	54.34	54.66	55.04
CaO	0.00	0.00	0.00	0.01	0.00	0.00	0.00	0.00	0.01	0.00
Na_2O	0.00	0.00	0.00	0.00	0.00	0.00	0.00	0.00	0.00	0.00
K_2O	0.01	0.03	0.02	0.01	0.03	0.02	0.03	0.03	0.01	0.02
NiO	0.53	0.68	0.69	0.70	0.63	0.67	0.67	0.66	0.60	0.42
Total	99.59	100.60	99.75	100.11	99.46	99.82	99.20	99.96	99.76	100.50
Mg#	0.97	0.97	0.97	0.97	0.97	0.97	0.97	0.97	0.97	0.98
Si	1.00	0.99	1.00	1.00	0.99	0.99	0.99	1.00	0.99	1.00
Ti	0.00	0.00	0.00	0.00	0.00	0.00	0.00	0.00	0.00	0.00
Al	0.00	0.00	0.00	0.00	0.00	0.00	0.00	0.00	0.00	0.00
Cr	0.00	0.00	0.00	0.00	0.00	0.00	0.00	0.00	0.00	0.00
Fe*	0.05	0.07	0.05	0.05	0.05	0.05	0.06	0.06	0.05	0.04
Mn	0.00	0.01	0.01	0.01	0.01	0.01	0.01	0.01	0.01	0.00
Mg	1.94	1.92	1.94	1.93	1.94	1.94	1.93	1.93	1.94	1.93
Ca	0.00	0.00	0.00	0.00	0.00	0.00	0.00	0.00	0.00	0.00
Na	0.00	0.00	0.00	0.00	0.00	0.00	0.00	0.00	0.00	0.00
K	0.00	0.00	0.00	0.00	0.00	0.00	0.00	0.00	0.00	0.00
Ni	0.01	0.01	0.01	0.01	0.01	0.01	0.01	0.01	0.01	0.01
Total	3.00	3.01	3.00	3.00	3.01	3.01	3.01	3.00	3.01	3.00

Table 1 continued

Sample	19404									
Mineral	olivine	olivine	olivine	olivine	olivine	olivine	olivine	olivine	olivine	olivine
Position	dusty	dusty	clear	clear	dusty	clear	dusty	dusty	clear	dusty
SiO_2	41.55	40.98	41.78	41.15	40.97	41.70	41.33	41.44	41.52	41.14
TiO_2	0.00	0.00	0.00	0.00	0.00	0.00	0.00	0.00	0.00	0.00
Al_2O_3	0.00	0.00	0.00	0.00	0.00	0.00	0.00	0.00	0.00	0.00
Cr_2O_3	0.00	0.00	0.00	0.00	0.00	0.00	0.00	0.00	0.00	0.00
FeO*	2.89	2.67	2.36	2.12	3.58	2.40	3.36	3.06	2.32	2.85
MnO	0.34	0.35	0.13	0.08	0.18	0.14	0.20	0.28	0.16	0.23
MgO	53.98	54.15	54.89	54.88	53.34	54.63	53.63	54.40	54.55	54.02
CaO	0.00	0.01	0.00	0.00	0.00	0.01	0.00	0.01	0.00	0.01
Na_2O	0.00	0.00	0.01	0.01	0.00	0.00	0.00	0.00	0.01	0.00
K_2O	0.02	0.00	0.01	0.01	0.01	0.01	0.01	0.02	0.00	0.01
NiO	0.53	0.50	0.38	0.36	0.47	0.45	0.53	0.50	0.41	0.51
Total	99.31	98.65	99.57	98.62	98.55	99.33	99.07	99.70	98.97	98.78
Mg#	0.97	0.97	0.98	0.98	0.96	0.98	0.97	0.97	0.98	0.97
Si	1.00	0.99	1.00	0.99	0.99	1.00	1.00	0.99	1.00	0.99
Ti	0.00	0.00	0.00	0.00	0.00	0.00	0.00	0.00	0.00	0.00
Al	0.00	0.00	0.00	0.00	0.00	0.00	0.00	0.00	0.00	0.00
Cr	0.00	0.00	0.00	0.00	0.00	0.00	0.00	0.00	0.00	0.00
Fe*	0.06	0.05	0.05	0.04	0.07	0.05	0.07	0.06	0.05	0.06
Mn	0.01	0.01	0.00	0.00	0.00	0.00	0.00	0.01	0.00	0.00
Mg	1.93	1.95	1.95	1.97	1.93	1.95	1.93	1.94	1.95	1.94
Ca	0.00	0.00	0.00	0.00	0.00	0.00	0.00	0.00	0.00	0.00
Na	0.00	0.00	0.00	0.00	0.00	0.00	0.00	0.00	0.00	0.00
K	0.00	0.00	0.00	0.00	0.00	0.00	0.00	0.00	0.00	0.00
Ni	0.01	0.01	0.01	0.01	0.01	0.01	0.01	0.01	0.01	0.01
Total	3.00	3.01	3.00	3.01	3.01	3.00	3.00	3.01	3.00	3.01

Table 1 continued

Sample	194904					194901		194897	
Mineral	olivine	olivine	olivine	olivine	olivine	olivine	olivine	olivine	olivine
Position	dusty	dusty	clear	dusty	clear	dusty	dusty	clear	clear
SiO_2	41.70	40.74	41.42	41.06	41.03	40.41	40.90	40.83	40.95
TiO_2	0.00	0.01	0.00	0.02	0.01	0.01	0.00	0.00	0.01
Al_2O_3	0.00	0.01	0.00	0.00	0.00	0.00	0.00	0.00	0.00
Cr_2O_3	0.00	0.00	0.00	0.00	0.02	0.00	0.00	0.00	0.00
FeO*	3.18	3.11	2.40	2.91	2.54	2.30	2.45	2.29	2.12
MnO	0.40	0.36	0.11	0.22	0.16	0.59	0.32	0.18	0.11
MgO	54.51	54.04	55.27	54.19	55.21	53.44	54.47	54.45	54.98
CaO	0.01	0.00	0.00	0.00	0.01	0.01	0.01	0.00	0.00
Na_2O	0.00	0.00	0.00	0.00	0.00	0.00	0.00	0.00	0.00
K_2O	0.02	0.01	0.03	0.01	0.01	0.01	0.01	0.01	0.02
NiO	0.57	0.55	0.37	0.52	0.44	0.62	0.58	0.49	0.48
Total	100.40	98.81	99.60	98.93	99.42	97.39	98.75	98.26	98.66
Mg#	0.97	0.97	0.98	0.97	0.97	0.98	0.98	0.98	0.98
Si	0.99	0.99	0.99	0.99	0.98	0.99	0.99	0.99	0.99
Ti	0.00	0.00	0.00	0.00	0.00	0.00	0.00	0.00	0.00
Al	0.00	0.00	0.00	0.00	0.00	0.00	0.00	0.00	0.00
Cr	0.00	0.00	0.00	0.00	0.00	0.00	0.00	0.00	0.00
Fe*	0.06	0.06	0.05	0.06	0.05	0.05	0.05	0.05	0.04
Mn	0.01	0.01	0.00	0.00	0.00	0.01	0.01	0.00	0.00
Mg	1.93	1.95	1.97	1.95	1.97	1.95	1.96	1.96	1.97
Ca	0.00	0.00	0.00	0.00	0.00	0.00	0.00	0.00	0.00
Na	0.00	0.00	0.00	0.00	0.00	0.00	0.00	0.00	0.00
K	0.00	0.00	0.00	0.00	0.00	0.00	0.00	0.00	0.00
Ni	0.01	0.01	0.01	0.01	0.01	0.01	0.01	0.01	0.01
Total	3.01	3.01	3.01	3.01	3.02	3.01	3.01	3.01	3.01

Table 1 continued

Sample	194906	194906	194905			
Mineral	olivine	olivine	olivine	olivine	olivine	olivine
Position	clear	clear	clear	dusty	dusty	clear
SiO_2	41.70	41.13	41.33	41.15	41.06	41.33
TiO_2	0.01	0.00	0.00	0.02	0.01	0.00
Al_2O_3	0.00	0.00	0.00	0.00	0.01	0.01
Cr_2O_3	0.00	0.00	0.00	0.00	0.01	0.01
FeO*	2.90	2.34	2.88	3.92	3.95	2.58
MnO	0.20	0.09	0.25	0.22	0.21	0.16
MgO	54.82	54.85	53.73	53.47	54.16	54.98
CaO	0.00	0.00	0.00	0.00	0.00	0.00
Na_2O	0.00	0.00	0.00	0.01	0.04	0.00
K_2O	0.00	0.02	0.02	0.01	0.02	0.01
NiO	0.53	0.36	0.50	0.50	0.45	0.46
Total	100.17	98.77	98.70	99.30	99.91	99.53
Mg#	0.97	0.98	0.97	0.96	0.96	0.97
Si	0.99	0.99	1.00	0.99	0.99	0.99
Ti	0.00	0.00	0.00	0.00	0.00	0.00
Al	0.00	0.00	0.00	0.00	0.00	0.00
Cr	0.00	0.00	0.00	0.00	0.00	0.00
Fe*	0.06	0.05	0.06	0.08	0.08	0.05
Mn	0.00	0.00	0.01	0.00	0.00	0.00
Mg	1.94	1.97	1.93	1.92	1.94	1.96
Ca	0.00	0.00	0.00	0.00	0.00	0.00
Na	0.00	0.00	0.00	0.00	0.00	0.00
K	0.00	0.00	0.00	0.00	0.00	0.00
Ni	0.01	0.01	0.01	0.01	0.01	0.01
Total	3.01	3.01	3.00	3.01	3.02	3.01

Table 2. Trace-element mineral chemistry of olivine from the Lens A and B metadunites.

Sample No.	#201-2020	#202-2020	#203-2020	194904_#103	194903_#202-	194903_#212
Remarks	Lens A	Lens A	Lens A	Lens B	Lens B	Lens B
Mineral	Atg	Atg	Ol (bulk)	Ol	Ol	Ol
Li	1.01	0.24	2.15	79.44	5.44	47.51
B	6.13	8.21	1.79	20.91	16.13	14.83
Sc	12.12	13.62	4.27	4.21	7.67	3.18
Ti	106.59	103.67	51.60	94.74	4.41	89.27
V	43.00	52.20	14.98	0.61	0.15	0.44
Cr	1614.24	3267.48	508.56	45.95	8.58	16.70
Co	76.30	52.43	148.71	275.51	270.98	298.38
Ni	2890.72	2364.67	4051.21	4552.75	5206.73	5148.07
Rb	0.08	0.16	0.01			
Sr	0.08	0.16	0.06		0.01	
Y	1.12	1.55	0.40	0.28	0.07	0.07
Zr	0.60	0.98	0.09	0.99	0.22	0.59
Nb	0.06	0.05	0.02	1.02	0.08	0.71
Cs	0.08	0.19	0.00			
Ba	0.14	0.29	0.18		0.01	
La	0.12	0.11	0.01	0.05		0.00
Ce	0.51	0.54	0.06	0.18	0.02	0.02
Pr	0.06	0.07	0.01	0.02		
Nd	0.32	0.40	0.04	0.07	0.01	0.01
Sm	0.11	0.14	0.01	0.02	0.01	
Eu	0.03	0.02	0.00			
Gd	0.16	0.17	0.02	0.02		0.00
Tb	0.03	0.04	0.00	0.01		
Dy	0.17	0.23	0.04	0.03	0.01	0.01
Ho	0.04	0.05	0.01	0.01	0.00	0.00
Er	0.12	0.16	0.04	0.03	0.02	0.01
Tm	0.02	0.03	0.01		0.01	0.00
Yb	0.15	0.20	0.09	0.02	0.06	0.02
Lu	0.03	0.03	0.02	0.01	0.02	0.01
Hf	0.03	0.06	0.00	0.03	0.02	0.02
Ta	0.00	0.01	0.00	0.08	0.01	0.05
Pb	0.34	0.34	0.12	0.03	0.06	0.04
Th	0.04	0.05	0.00			
U	0.01	0.02	0.00	0.01		0.01
Zn						
Ga						

Table 3. Major-element mineral chemistry of antigorites from Lens B metadunites.

Sample	194897			194901			194903		
Type	atg	atg	atg	atg	atg	atg	atg	atg	atg
Position	blades	gmass	blades	gmass	gmass	blades	gmass	gmass	blades
EPMA Point	5	4	8	7	6	5	4	8	9
SiO_2	41.62	42.96	41.95	40.59	41.41	41.34	42.41	42.60	43.17
TiO_2	0.07	0.03	0.03	0.07	0.03	0.03	0.02	0.04	0.02
Al_2O_3	0.77	0.89	1.44	1.24	1.45	1.92	1.19	1.46	1.72
Cr_2O_3	0.07	0.03	0.11	0.17	0.26	0.25	0.06	0.05	0.06
FeO*	1.43	1.06	1.40	1.49	1.57	2.00	1.44	1.55	1.58
MnO	0.00	0.04	0.01	0.01	0.01	0.02	0.01	0.05	0.03
MgO	39.46	38.87	38.94	38.28	38.26	38.18	39.23	39.12	38.84
CaO	0.00	0.00	0.00	0.01	0.00	0.01	0.00	0.00	0.01
Na_2O	0.03	0.00	0.03	0.00	0.00	0.00	0.00	0.00	0.00
K_2O	0.01	0.04	0.01	0.01	0.02	0.00	0.02	0.02	0.01
NiO	0.18	0.14	0.14	0.16	0.18	0.15	0.14	0.16	0.18
Total	83.64	84.05	84.05	82.05	83.19	83.89	84.51	85.04	85.61
Mg#	0.98	0.98	0.98	0.98	0.98	0.97	0.98	0.98	0.98
Si	33.31	34.01	33.34	33.13	33.31	33.05	33.51	33.47	33.65
Ti	0.04	0.02	0.02	0.04	0.02	0.02	0.01	0.03	0.01
Al	0.73	0.83	1.35	1.19	1.38	1.81	1.11	1.35	1.58
Cr	0.04	0.02	0.07	0.11	0.16	0.16	0.03	0.03	0.04
Fe*	0.96	0.70	0.93	1.02	1.06	1.34	0.95	1.02	1.03
Mn	0.00	0.03	0.01	0.01	0.00	0.02	0.01	0.03	0.02
Mg	47.04	45.84	46.10	46.54	45.85	45.47	46.18	45.79	45.09
Ca	0.00	0.00	0.00	0.01	0.00	0.01	0.00	0.00	0.01
Na	0.05	0.00	0.04	0.00	0.00	0.00	0.00	0.00	0.00
K	0.01	0.04	0.01	0.01	0.02	0.00	0.02	0.02	0.01
Ni	0.11	0.09	0.09	0.11	0.11	0.09	0.09	0.10	0.11
Total	82.29	81.57	81.96	82.18	81.91	81.96	81.91	81.82	81.54
XAl	0.09	0.10	0.17	0.15	0.17	0.23	0.14	0.17	0.20
Mg/Si	1.41	1.35	1.38	1.40	1.38	1.38	1.38	1.37	1.34
Mg+Fe	48.00	46.54	47.03	47.56	46.90	46.81	47.13	46.80	46.12

Normalized to 116 oxygens

Table 3 continued

Sample	194904						194905	
Type	atg	atg	atg	atg	atg	atg	atg	atg
Position	inclusion	inclusion	blades	gmass	gmass	gmass	gmass	gmass
EPMA Point	26b	14	24b	7b	30b	31b	15	7
SiO_2	40.10	43.38	43.04	40.05	42.69	41.84	41.35	41.53
TiO_2	0.00	0.01	0.01	0.12	0.01	0.00	0.04	0.03
Al_2O_3	0.01	0.34	1.40	1.46	1.48	2.08	1.70	2.61
Cr_2O_3	0.01	0.04	0.11	0.64	0.04	0.03	0.16	0.16
FeO*	1.48	1.23	1.88	1.63	1.56	1.83	1.65	1.99
MnO	0.11	0.07	0.01	0.02	0.03	0.02	0.04	0.01
MgO	40.82	38.71	39.31	38.77	38.82	38.31	38.37	37.71
CaO	0.00	0.00	0.00	0.01	0.00	0.00	0.00	0.01
Na_2O	0.00	0.00	0.01	0.00	0.00	0.00	0.04	0.02
K_2O	0.02	0.01	0.01	0.04	0.01	0.01	0.02	0.02
NiO	0.47	0.17	0.16	0.14	0.20	0.17	0.18	0.13
Total	83.01	83.96	85.94	82.88	84.84	84.29	83.55	84.21
Mg#	0.98	0.98	0.97	0.98	0.98	0.97	0.98	0.97
Si	32.59	34.39	33.51	32.51	33.60	33.21	33.14	33.02
Ti	0.00	0.00	0.00	0.07	0.01	0.00	0.02	0.02
Al	0.01	0.31	1.29	1.40	1.38	1.95	1.61	2.45
Cr	0.00	0.02	0.07	0.41	0.02	0.02	0.10	0.10
Fe*	1.01	0.81	1.23	1.11	1.03	1.21	1.11	1.32
Mn	0.08	0.05	0.01	0.01	0.02	0.01	0.03	0.01
Mg	49.41	45.72	45.59	46.88	45.51	45.30	45.81	44.66
Ca	0.00	0.00	0.00	0.01	0.00	0.00	0.00	0.01
Na	0.00	0.00	0.01	0.00	0.00	0.00	0.07	0.04
K	0.02	0.01	0.01	0.04	0.01	0.01	0.02	0.02
Ni	0.31	0.11	0.10	0.09	0.12	0.11	0.12	0.08
Total	83.41	81.43	81.82	82.53	81.70	81.82	82.03	81.72
XAl	0.00	0.04	0.16	0.17	0.17	0.24	0.20	0.31
Mg/Si	1.52	1.33	1.36	1.44	1.35	1.36	1.38	1.35
Mg+Fe	50.41	46.53	46.82	47.99	46.54	46.51	46.92	45.98

Table 3 continued

Sample	194906				194896CPL			
Type	atg	atg	atg	atg	atg	atg	atg	atg
Position	gmass	gmass	gmass	blades	inclusion	blades	blades	blades
EPMA Point	5	4	6	7	20	29	14	11
SiO_2	42.63	42.63	41.78	41.23	43.82	42.81	42.65	43.64
TiO_2	0.01	0.00	0.03	0.06	0.03	0.01	0.03	0.00
Al_2O_3	1.16	1.22	1.38	1.46	0.52	1.09	1.19	1.22
Cr_2O_3	0.40	0.23	0.45	0.66	0.07	0.16	0.05	0.03
FeO*	1.35	1.46	1.73	1.67	1.11	1.43	1.44	1.13
MnO	0.00	0.01	0.03	0.02	0.00	0.04	0.02	0.01
MgO	38.52	38.98	38.86	38.94	39.33	39.07	38.61	38.82
CaO	0.00	0.02	0.00	0.00	0.00	0.00	0.00	0.00
Na_2O	0.01	0.01	0.00	0.00	0.00	0.01	0.01	0.00
K_2O	0.02	0.02	0.02	0.01	0.02	0.02	0.02	0.01
NiO	0.15	0.15	0.13	0.15	0.14	0.18	0.16	0.14
Total	84.26	84.73	84.40	84.18	85.03	84.81	84.18	84.99
Mg#	0.98	0.98	0.98	0.98	0.98	0.98	0.98	0.98
Si	33.76	33.61	33.19	32.89	34.27	33.71	33.80	34.12
Ti	0.01	0.00	0.01	0.03	0.02	0.00	0.02	0.00
Al	1.09	1.13	1.29	1.37	0.48	1.01	1.11	1.12
Cr	0.25	0.15	0.28	0.41	0.04	0.10	0.03	0.02
Fe*	0.89	0.96	1.15	1.12	0.73	0.94	0.95	0.74
Mn	0.00	0.01	0.02	0.01	0.00	0.03	0.01	0.01
Mg	45.45	45.78	45.98	46.26	45.82	45.83	45.57	45.21
Ca	0.00	0.02	0.00	0.00	0.00	0.00	0.00	0.00
Na	0.02	0.01	0.01	0.00	0.00	0.01	0.02	0.00
K	0.02	0.02	0.02	0.01	0.02	0.02	0.02	0.01
Ni	0.09	0.10	0.09	0.09	0.09	0.11	0.10	0.09
Total	81.58	81.77	82.03	82.20	81.46	81.75	81.63	81.32
XAl	0.14	0.14	0.16	0.17	0.06	0.13	0.14	0.14
Mg/Si	1.35	1.36	1.39	1.41	1.34	1.36	1.35	1.33
Mg+Fe	46.34	46.74	47.12	47.38	46.55	46.77	46.53	45.95

Table 3 continued

Sample	194898B		
Type	atg	atg	atg
Position	blades	gmass	blades
EPMA Point	1	3	
SiO_2	42.66	42.59	43.01
TiO_2	0.00	0.02	0.01
Al_2O_3	1.11	1.59	1.98
Cr_2O_3	0.05	0.05	0.04
FeO*	2.28	2.33	2.89
MnO	0.06	0.04	0.04
MgO	38.19	38.12	38.26
CaO	0.00	0.01	0.00
Na_2O	0.02	0.00	0.02
K_2O	0.00	0.02	0.02
NiO	0.28	0.29	0.27
Total	84.63	85.07	86.53
Mg#	0.97	0.97	0.96
Si	33.80	33.58	33.424
Ti	0.00	0.01	0.008
Al	1.04	1.48	1.813
Cr	0.03	0.03	0.025
Fe*	1.51	1.54	1.878
Mn	0.04	0.03	0.023
Mg	45.07	44.77	44.286
Ca	0.00	0.00	0.002
Na	0.02	0.00	0.026
K	0.00	0.02	0.015
Ni	0.18	0.19	0.170
Total	81.68	81.66	81.670
XAl	0.13	0.18	0.23
Mg/Si	1.33	1.33	1.325
Mg+Fe	46.57	46.31	46.16

Table 4. Major-element mineral chemistry of lizardites from Lens B metadunites.

Sample	194897			194903			
Type	liz	liz	liz	liz	liz	liz	liz
Position	vein	vein	vein	vein	vein	vein	vein
EPMA Point	2	12	4	6b	7b	1	7
SiO_2	39.09	40.00	38.36	39.26	41.99	39.80	37.45
TiO_2	0.00	0.00	0.00	0.00	0.00	0.00	0.00
Al_2O_3	0.01	0.00	0.00	0.01	0.00	0.02	0.00
Cr_2O_3	0.00	0.00	0.00	0.00	0.00	0.00	0.00
FeO*	2.04	1.35	2.34	1.76	0.85	1.98	2.32
MnO	0.00	0.06	0.06	0.07	0.02	0.03	0.06
MgO	39.40	39.88	39.59	40.68	40.48	39.86	40.39
CaO	0.00	0.00	0.00	0.00	0.00	0.01	0.00
Na_2O	0.01	0.00	0.00	0.00	0.00	0.03	0.00
K_2O	0.02	0.01	0.00	0.01	0.01	0.01	0.01
NiO	0.47	0.26	0.38	0.45	0.43	0.35	0.63
Total	81.04	81.56	80.73	82.24	83.77	82.09	80.85
Mg#	0.97	0.98	0.97	0.98	0.99	0.97	0.97
Si	32.63	32.95	32.24	32.29	33.51	32.74	31.58
Ti	0.00	0.00	0.00	0.00	0.00	0.00	0.00
Al	0.01	0.00	0.00	0.01	0.00	0.02	0.00
Cr	0.00	0.00	0.00	0.00	0.00	0.00	0.00
Fe*	1.42	0.93	1.64	1.21	0.56	1.36	1.63
Mn	0.00	0.04	0.04	0.05	0.01	0.02	0.04
Mg	48.98	48.94	49.57	49.84	48.12	48.84	50.73
Ca	0.00	0.00	0.00	0.00	0.00	0.01	0.00
Na	0.01	0.00	0.00	0.00	0.00	0.05	0.00
K	0.02	0.01	0.00	0.01	0.01	0.01	0.02
Ni	0.31	0.17	0.26	0.30	0.28	0.23	0.43
Total3	83.39	83.05	83.76	83.71	82.49	83.29	84.43
XAl	0.00	0.00	0.00	0.00	0.00	0.00	0.00
Mg/Si	1.50	1.49	1.54	1.54	1.44	1.49	1.61
Mg+Fe	50.41	49.88	51.22	51.06	48.69	50.21	52.37

Normalized to 116 oxygens

Table 4 continued

Sample	194904							194905	
Type	liz	liz	liz	liz	liz	liz	liz	liz	liz
Position	vein	vein	vein	vein	vein	vein	vein	vein	vein
EPMA Point	8b	9b	14b	19b	22b	23b	18	16	5
SiO_2	38.36	38.72	37.76	39.96	41.37	38.60	40.31	40.01	40.13
TiO_2	0.00	0.00	0.00	0.00	0.00	0.00	0.00	0.00	0.00
Al_2O_3	0.01	0.00	0.00	0.00	0.00	0.00	0.02	0.00	0.00
Cr_2O_3	0.00	0.01	0.00	0.00	0.00	0.00	0.00	0.00	0.00
FeO*	2.55	2.74	2.15	2.16	1.13	1.91	1.59	1.48	1.66
MnO	0.07	0.04	0.08	0.10	0.04	0.08	0.04	0.03	0.04
MgO	39.98	40.12	40.91	40.72	40.93	41.86	40.17	40.62	41.20
CaO	0.00	0.01	0.00	0.01	0.00	0.02	0.00	0.00	0.00
Na_2O	0.01	0.01	0.00	0.01	0.01	0.01	0.01	0.01	0.00
K_2O	0.01	0.02	0.01	0.01	0.01	0.01	0.01	0.02	0.02
NiO	0.37	0.32	0.42	0.28	0.33	0.36	0.31	0.77	0.36
Total	81.36	82.01	81.33	83.24	83.82	82.85	82.45	82.93	83.40
Mg#	0.97	0.96	0.97	0.97	0.98	0.98	0.98	0.98	0.98
Si	32.06	32.12	31.58	32.48	33.10	31.63	32.90	32.59	32.47
Ti	0.00	0.00	0.00	0.00	0.00	0.00	0.00	0.00	0.00
Al	0.01	0.00	0.00	0.00	0.00	0.00	0.02	0.00	0.00
Cr	0.00	0.01	0.00	0.00	0.00	0.00	0.00	0.00	0.00
Fe*	1.78	1.90	1.51	1.47	0.76	1.31	1.08	1.01	1.12
Mn	0.05	0.03	0.06	0.07	0.03	0.06	0.03	0.02	0.03
Mg	49.78	49.57	50.98	49.30	48.78	51.10	48.84	49.28	49.66
Ca	0.00	0.01	0.00	0.01	0.00	0.02	0.00	0.00	0.00
Na	0.02	0.02	0.00	0.01	0.02	0.01	0.01	0.02	0.00
K	0.01	0.02	0.01	0.01	0.01	0.01	0.01	0.02	0.02
Ni	0.25	0.22	0.28	0.18	0.21	0.24	0.21	0.50	0.23
Total3	83.95	83.90	84.42	83.53	82.91	84.38	83.10	83.43	83.54
XAl	0.00	0.00	0.00	0.00	0.00	0.00	0.00	0.00	0.00
Mg/Si	1.55	1.54	1.61	1.52	1.47	1.62	1.48	1.51	1.53
Mg+Fe	51.56	51.47	52.49	50.76	49.54	52.40	49.93	50.28	50.79

Table 4 continued

Sample	194906			194896CPL	
Type	liz	liz	liz	liz	liz
Position	vein	vein	vein	vein	vein
EPMA Point	2	3	8	2(2)	26
SiO_2	40.90	38.96	38.17	39.63	41.56
TiO_2	0.01	0.00	0.00	0.00	0.03
Al_2O_3	0.00	0.09	0.00	0.00	0.22
Cr_2O_3	0.00	0.04	0.00	0.00	0.05
FeO*	1.09	2.10	1.77	1.30	1.42
MnO	0.06	0.08	0.04	0.02	0.03
MgO	40.46	40.09	41.18	40.00	39.32
CaO	0.00	0.00	0.00	0.00	0.00
Na_2O	0.00	0.01	0.00	0.00	0.00
K_2O	0.00	0.01	0.02	0.02	0.01
NiO	0.33	0.33	0.32	0.40	0.27
Total	82.85	81.70	81.49	81.37	82.91
Mg#	0.99	0.97	0.98	0.98	0.98
Si	33.10	32.29	31.75	32.77	2.03
Ti	0.01	0.00	0.00	0.00	0.00
Al	0.00	0.09	0.00	0.00	0.01
Cr	0.00	0.02	0.00	0.00	0.00
Fe*	0.74	1.45	1.23	0.90	0.06
Mn	0.04	0.06	0.03	0.02	0.00
Mg	48.78	49.51	51.02	49.27	2.85
Ca	0.00	0.00	0.00	0.00	0.00
Na	0.00	0.02	0.00	0.00	0.00
K	0.00	0.01	0.02	0.02	0.00
Ni	0.22	0.22	0.21	0.27	0.01
Total	82.89	83.67	84.26	83.24	4.97
XAl	0.00	0.01	0.00	0.00	0.00
Mg/Si	1.47	1.53	1.61	1.50	1.41
Mg+Fe	49.52	50.96	52.25	50.17	2.91

Table 5. Major-element mineral chemistry of titanian chondrodite (Ti-Chn) and titanian clinohumite (Ti-Chu) from Lens B metadunites.

Ti-Chn				
Sample	194904			
Point	13-bb	14-b	16-b	
SiO_2	32.77	33.65	32.47	33.27
TiO_2	8.64	7.72	9.22	8.39
Al_2O_3	0.03	0.05	0.03	0
Cr_2O_3	0.1	0	0.15	0.02
FeO*	2.34	2.94	2.28	2.98
MnO	0.32	0.26	0.27	0.24
MgO	47.81	47.94	47.87	49.7
CaO	0.04	0.08	0.08	0
Na_2O	0.03	0.04	0.01	0.02
K_2O	0.03	0.05	0.05	0.03
NiO	0.1	0.1	0.07	0.23
F	0.03	0	0	0
Total	95.12	95.99	95.27	97.99
a.f.u.				
Si	2.03	2.07	2.01	2
Ti	0.4	0.36	0.43	0.38
Al	0	0	0	0
Cr	0	0	0.01	0
Fe^{2+}	0.12	0.15	0.12	0.15
Mn	0.02	0.01	0.01	0.01
Mg	4.41	4.39	4.41	4.45
Ca	0	0.01	0.01	0
Na	0	0	0	0
K	0	0.01	0.01	0
Ni	0.01	0.01	0	0.01
F	0.01	0	0	0
TOTAL	7	7	7	7
XMg	0.97	0.97	0.97	0.97
XTi	0.4	0.36	0.43	0.38
M/Si	2.44	2.38	2.48	2.5
Mg+Fe+Mn+Ni	4.56	4.56	4.55	4.62
XF (F/2)	0	0	0	0

Normalized to 7 cations

Table 5 continued

	Ti-Chu									
Sample	194906		194903							194901
Point	5-b	11-b	29-b	34-b	35-b	36-b	37-b	1	18	40-b
SiO_2	37.51	37.11	36.59	38.5	36.82	35.93	36.63	37.29	36.94	35.65
TiO_2	4.92	4.66	4.11	2.42	3.35	5.18	4.03	4.06	3.95	5.86
Al_2O_3	0	0.01	0	0	0	0	0.01	0	0	0
Cr_2O_3	0.02	0	0	0	0	0.02	0	0	0	0.01
FeO*	2.42	2.5	3.28	2.8	3.48	3.68	3.19	3.33	2.16	2.45
MnO	0.25	0.26	0.17	0.14	0.15	0.22	0.12	0.14	0.12	0.21
MgO	52.63	50.93	51.25	52.22	51.16	50.34	50.9	52.09	53.55	51.21
CaO	0	0	0.05	0.06	0.06	0.05	0.06	0	0	0.07
Na_2O	0	0.03	0	0.01	0	0.01	0	0	0	0
K_2O	0.03	0.03	0.04	0.05	0.04	0.03	0.06	0	0.01	0.07
NiO	0.26	0.28	0.23	0.22	0.21	0.26	0.2	0.27	0.26	0.25
F	0.11	0.16	0	0	0	0	0.03	0	0	0
Total	99.81	97.61	97.53	98.65	97.26	97.29	97.05	97.19	96.99	97.19
a.f.u.										
Si	3.98	4.03	3.99	4.14	4.02	3.94	4.01	4.09	4.04	3.89
Ti	0.39	0.38	0.34	0.2	0.28	0.43	0.33	0.34	0.33	0.48
Al	0	0	0	0	0	0	0	0	0	0
Cr	0	0	0	0	0	0	0	0	0	0
Fe^{2+}	0.21	0.23	0.3	0.25	0.32	0.34	0.29	0.31	0.2	0.22
Mn	0.02	0.02	0.02	0.01	0.01	0.02	0.01	0.01	0.01	0.02
Mg	8.33	8.25	8.33	8.37	8.33	8.23	8.31	8.52	8.74	8.34
Ca	0	0	0.01	0.01	0.01	0.01	0.01	0	0	0.01
Na	0	0	0	0	0	0	0	0	0	0
K	0.01	0.01	0.01	0.01	0.01	0.01	0.01	0	0	0.01
Ni	0.02	0.02	0.02	0.02	0.02	0.02	0.02	0.02	0.02	0.02
F	0.04	0.05	0	0	0	0	0.01	0	0	0
TOTAL	13	13	13	13	13	13	13	13	13	13
XMg	0.97	0.97	0.97	0.97	0.96	0.96	0.97	0.97	0.98	0.97
XTi	0.39	0.38	0.34	0.2	0.28	0.43	0.33	0.34	0.33	0.48
M/Si	2.26	2.21	2.26	2.14	2.23	2.29	2.23	2.25	2.3	2.33
Mg+Fe+Mn+Ni	8.58	8.52	8.66	8.65	8.69	8.62	8.63	8.86	8.97	8.6
XF (F/2)	0.02	0.03	0	0	0	0	0	0	0	0

Normalized to 13cations

Table 6. Major-element mineral chemistry of spinels from Lens B metadunites.

Sample	194905		
EPMA point	27	28	29
Position	core	mid	rim
SiO_2	0.00	0.01	0.00
TiO_2	1.20	1.03	0.08
Al_2O_3	11.44	0.71	0.02
Cr_2O_3	49.67	43.17	0.37
FeO*	25.68	43.78	89.51
MnO	1.32	2.25	0.10
MgO	8.60	4.70	1.08
CaO	0.01	0.00	0.00
Na_2O	0.03	0.04	0.03
K_2O	0.00	0.00	0.00
NiO	0.10	0.55	1.59
Total	98.05	96.23	92.77
Mg#	0.43	0.26	0.06
Cr#	0.74	0.98	0.93
Si	0.00	0.00	0.00
Ti	0.03	0.03	0.00
Al	0.45	0.03	0.00
Cr	1.32	1.26	0.01
Fe3+	0.15	0.63	1.96
Fe2+	0.57	0.72	0.92
Mn	0.04	0.07	0.00
Mg	0.43	0.26	0.06
Ca	0.00	0.00	0.00
Na	0.00	0.00	0.00
K	0.00	0.00	0.00
Ni	0.00	0.02	0.05
Total	3.01	3.01	3.01
Cr/	0.69	0.66	0.01
Al/	0.24	0.02	0.00
Fe3+/3+	0.08	0.33	0.99

Normalized to 4 oxygens

Table 7. Major-element mineral chemistry of magnesite and stichtite from Lens B metadunites.

Sample	194896			194904	194903	194906	194904
Mineral	magnesite	magnesite	magnesite	magnesite	magnesite	stichtite	stichtite
EPMA point	9	27	8	2	22	23	3
SiO_2	0.06	0.00	0	0.00	2.85	0	0.11
TiO_2	0.00	0.00	0.027	0.00	0.01	0	0.00
Al_2O_3	0.00	0.01	0	0.00	0.15	0.389	2.36
Cr_2O_3	0.00	0.00	0.117	0.00	0.00	20.347	16.54
FeO	0.62	1.31	87.047	0.74	1.56	2.007	2.89
MnO	0.41	0.25	0.113	0.17	0.36	0.015	0.05
MgO	38.80	38.51	1.504	38.56	39.23	37.403	36.54
CaO	0.04	0.04	0	0.05	0.15	0	0.00
Na_2O	0.00	0.00	0.01	0.01	0.00	0.018	0.01
K_2O	0.02	0.01	0.025	0.01	0.03	0.013	0.01
NiO	0.03	0.04	2.322	0.01	0.04	0.426	0.08
Total	39.99	40.16	91.165	39.54	44.38	60.618	58.586

Table 8. Major-element mineral chemistry of spinels from Lens A dunitic rocks.

Sample	208278			208278	208279			
Position	core	core	core	rim	core	core	mid	mid
EPMA Point	1	10	11	2	4	33	5	34
SiO_2	0.05	0.06	0.01	0.00	0.02	0.04	0.00	0.03
TiO_2	0.63	0.50	2.55	2.32	0.46	0.34	1.71	1.10
Al_2O_3	12.15	12.52	0.15	0.56	12.22	12.09	0.51	1.33
Cr_2O_3	50.05	49.14	22.72	41.61	49.04	49.31	37.37	43.81
FeO*	29.74	29.47	65.48	49.36	30.11	30.45	54.48	46.34
MnO	0.47	0.43	0.38	0.61	0.54	0.51	0.63	0.67
MgO	5.35	5.25	0.99	1.67	4.91	4.82	1.56	1.92
CaO	0.00	0.01	0.13	0.00	0.01	0.00	0.00	0.00
Na_2O	0.03	0.03	0.00	0.00	0.04	0.02	0.03	0.03
K_2O	0.00	0.00	0.00	0.00	0.00	0.00	0.00	0.00
NiO	0.11	0.09	0.71	0.40	0.11	0.09	0.49	0.24
Total	98.58	97.50	93.11	96.52	97.45	97.65	96.78	95.45
Mg#	0.27	0.27	0.06	0.09	0.25	0.25	0.09	0.11
Cr#	0.73	0.72	0.99	0.98	0.73	0.73	0.98	0.96
Si	0.00	0.00	0.00	0.00	0.001	0.001	0.000	0.001
Ti	0.02	0.01	0.07	0.07	0.012	0.009	0.048	0.031
Al	0.49	0.51	0.01	0.02	0.499	0.493	0.022	0.059
Cr	1.35	1.34	0.69	1.23	1.345	1.351	1.101	1.307
Fe3+	0.12	0.12	1.20	0.64	0.124	0.130	0.796	0.574
Fe2+	0.73	0.73	0.91	0.90	0.749	0.752	0.902	0.888
Mn	0.01	0.01	0.01	0.02	0.016	0.015	0.020	0.021
Mg	0.27	0.27	0.06	0.09	0.254	0.249	0.086	0.108
Ca	0.00	0.00	0.01	0.00	0.000	0.000	0.000	0.000
Na	0.00	0.00	0.00	0.00	0.002	0.001	0.002	0.002
K	0.00	0.00	0.00	0.00	0.000	0.000	0.000	0.000
Ni	0.00	0.00	0.02	0.01	0.003	0.002	0.015	0.007
Total3	3.00	3.00	2.98	2.99	3.005	3.004	2.993	2.999
Column4								
Cr/	0.69	0.68	0.36	0.65	0.68	0.68	0.57	0.67
Al/	0.25	0.26	0.00	0.01	0.25	0.25	0.01	0.03
Fe3+/3+	0.06	0.06	0.63	0.34	0.06	0.07	0.41	0.30

Normalized to 4 oxygens

Table 8 continued

Sample	208279		208282	
Position	rim	rim	rim	core
EPMA Point	6	35	39	38
SiO_2	0.00	0.00	0.00	0.16
TiO_2	0.85	0.30	1.02	0.35
Al_2O_3	0.07	0.00	0.06	11.58
Cr_2O_3	15.02	3.69	10.11	48.66
FeO*	75.44	85.15	77.72	30.92
MnO	0.24	0.07	0.16	0.51
MgO	0.71	0.32	0.54	4.27
CaO	0.00	0.00	0.00	0.00
Na_2O	0.00	0.00	0.02	0.05
K_2O	0.00	0.00	0.00	0.00
NiO	0.77	0.84	0.87	0.02
Total	93.10	90.36	90.49	96.53
Mg#	0.04	0.02	0.03	0.22
Cr#	0.99	1.00	0.99	0.74
Si				
Ti	4	4	4	4
Al	0.000	0.000	0.000	0.006
Cr	0.025	0.009	0.031	0.009
Fe3+	0.003	0.000	0.003	0.480
Fe2+	0.459	0.116	0.317	1.354
Mn	1.496	1.861	1.632	0.135
Mg	0.942	0.970	0.947	0.775
Ca	0.008	0.002	0.005	0.015
Na	0.041	0.019	0.032	0.224
K	0.000	0.000	0.000	0.000
Ni	0.000	0.000	0.001	0.003
Total3	0.000	0.000	0.000	0.000
Column4	0.024	0.027	0.028	0.001
Cr/	2.997	3.003	2.995	3.002
Al/				
Fe3+/3+	0.23	0.06	0.16	0.69
SiO_2	0.00	0.00	0.00	0.24
TiO_2	0.76	0.94	0.84	0.07

Table 9. Major-element mineral chemistry of olivine from Lens A dunitic rocks.

Sample	208278						
Mineral	olivine	olivine	olivine	olivine	olivine	olivine	olivine
Position	core	rim	core	core	core	core	core
EPMA Point	5	6	12	13	14	16	17
SiO_2	40.66	40.66	40.38	40.14	40.63	40.80	40.42
TiO_2	0.00	0.00	0.01	0.02	0.01	0.00	0.00
Al_2O_3	0.01	0.00	0.02	0.00	0.08	0.10	0.00
Cr_2O_3	0.00	0.02	0.00	0.01	0.08	0.06	0.01
FeO*	9.34	9.24	8.38	8.71	9.12	7.90	8.83
MnO	0.13	0.11	0.11	0.12	0.16	0.10	0.13
MgO	50.06	49.89	50.42	49.66	49.19	50.18	49.05
CaO	0.00	0.00	0.02	0.02	0.05	0.20	0.07
Na_2O	0.00	0.00	0.02	0.00	0.00	0.00	0.00
K_2O	0.00	0.00	0.00	0.00	0.00	0.00	0.00
NiO	0.50	0.51	0.46	0.48	0.51	0.43	0.50
Total	100.69	100.43	99.82	99.15	99.82	99.78	99.01
Mg#	0.91	0.91	0.91	0.91	0.91	0.92	0.91
Si	0.99	0.99	0.99	0.99	1.00	1.00	1.00
Ti	0.00	0.00	0.00	0.00	0.00	0.00	0.00
Al	0.00	0.00	0.00	0.00	0.00	0.00	0.00
Cr	0.00	0.00	0.00	0.00	0.00	0.00	0.00
Fe*	0.19	0.19	0.17	0.18	0.19	0.16	0.18
Mn	0.00	0.00	0.00	0.00	0.00	0.00	0.00
Mg	1.82	1.81	1.84	1.83	1.80	1.82	1.81
Ca	0.00	0.00	0.00	0.00	0.00	0.01	0.00
Na	0.00	0.00	0.00	0.00	0.00	0.00	0.00
K	0.00	0.00	0.00	0.00	0.00	0.00	0.00
Ni	0.01	0.01	0.01	0.01	0.01	0.01	0.01
Total	3.01	3.01	3.01	3.01	3.00	3.00	3.00

Table 9 continued

Sample	208279								
Mineral	olivine	olivine	olivine	olivine	olivine	olivine	olivine	olivine	olivine
Position	core	core	rim	core	core	core	rim	core	rim
EPMA Point	50	51	52	64	65	68	69	72	73
SiO_2	40.89	40.96	40.36	40.60	40.14	40.79	40.47	40.78	40.59
TiO_2	0.00	0.01	0.00	0.00	0.01	0.02	0.00	0.00	0.01
Al_2O_3	0.00	0.00	0.00	0.10	0.16	0.02	0.07	0.05	0.06
Cr_2O_3	0.02	0.00	0.00	0.01	0.01	0.00	0.02	0.00	0.00
FeO*	7.62	7.74	9.64	8.79	9.63	8.42	9.53	9.28	9.75
MnO	0.13	0.10	0.17	0.13	0.12	0.12	0.15	0.18	0.13
MgO	49.92	50.70	49.51	49.67	48.84	50.53	49.44	49.17	49.50
CaO	0.05	0.02	0.01	0.03	0.00	0.03	0.05	0.18	0.02
Na_2O	0.00	0.00	0.00	0.01	0.01	0.01	0.01	0.00	0.00
K_2O	0.00	0.00	0.00	0.00	0.00	0.00	0.01	0.00	0.00
NiO	0.45	0.52	0.55	0.48	0.57	0.49	0.55	0.50	0.56
Total	99.09	100.06	100.25	99.82	99.48	100.43	100.28	100.13	100.62
Mg#	0.92	0.92	0.90	0.91	0.90	0.91	0.90	0.90	0.90
Si	1.00	1.00	0.99	0.99	0.99	0.99	0.99	1.00	0.99
Ti	0.00	0.00	0.00	0.00	0.00	0.00	0.00	0.00	0.00
Al	0.00	0.00	0.00	0.00	0.00	0.00	0.00	0.00	0.00
Cr	0.00	0.00	0.00	0.00	0.00	0.00	0.00	0.00	0.00
Fe*	0.16	0.16	0.20	0.18	0.20	0.17	0.20	0.19	0.20
Mn	0.00	0.00	0.00	0.00	0.00	0.00	0.00	0.00	0.00
Mg	1.82	1.84	1.81	1.81	1.80	1.83	1.80	1.79	1.80
Ca	0.00	0.00	0.00	0.00	0.00	0.00	0.00	0.00	0.00
Na	0.00	0.00	0.00	0.00	0.00	0.00	0.00	0.00	0.00
K	0.00	0.00	0.00	0.00	0.00	0.00	0.00	0.00	0.00
Ni	0.01	0.01	0.01	0.01	0.01	0.01	0.01	0.01	0.01
Total	3.00	3.00	3.01	3.00	3.01	3.01	3.01	3.00	3.01

Table 9 continued

Sample	208279		208282					
Mineral	olivine	olivine	olivine	olivine	olivine	olivine	olivine	olivine
Position	rim	rim	core	rim	rim	core	core	core
EPMA Point	74	75	3	4	19	20	37	41
SiO_2	40.64	40.63	40.22	39.91	40.20	40.54	40.19	40.27
TiO_2	0.00	0.02	0.00	0.02	0.00	0.00	0.00	0.00
Al_2O_3	0.04	0.10	0.01	0.00	0.00	0.02	0.00	0.01
Cr_2O_3	0.02	0.01	0.05	0.04	0.00	0.00	0.03	0.00
FeO*	9.54	9.53	9.35	10.98	10.74	9.33	9.29	10.01
MnO	0.14	0.14	0.13	0.17	0.18	0.16	0.11	0.13
MgO	49.50	49.33	48.90	47.94	47.87	49.14	48.65	47.43
CaO	0.04	0.05	0.06	0.02	0.01	0.03	0.09	0.02
Na_2O	0.00	0.01	0.00	0.00	0.00	0.00	0.00	0.01
K_2O	0.00	0.00	0.00	0.00	0.00	0.00	0.00	0.00
NiO	0.49	0.55	0.51	0.61	0.54	0.51	0.50	0.49
Total	100.41	100.37	99.23	99.67	99.54	99.72	98.85	98.37
Mg#	0.90	0.90	0.90	0.89	0.89	0.90	0.90	0.89
Si	0.99	0.99	0.99	0.99	1.00	1.00	1.00	1.01
Ti	0.00	0.00	0.00	0.00	0.00	0.00	0.00	0.00
Al	0.00	0.00	0.00	0.00	0.00	0.00	0.00	0.00
Cr	0.00	0.00	0.00	0.00	0.00	0.00	0.00	0.00
Fe*	0.19	0.19	0.19	0.23	0.22	0.19	0.19	0.21
Mn	0.00	0.00	0.00	0.00	0.00	0.00	0.00	0.00
Mg	1.80	1.80	1.80	1.77	1.77	1.80	1.80	1.77
Ca	0.00	0.00	0.00	0.00	0.00	0.00	0.00	0.00
Na	0.00	0.00	0.00	0.00	0.00	0.00	0.00	0.00
K	0.00	0.00	0.00	0.00	0.00	0.00	0.00	0.00
Ni	0.01	0.01	0.01	0.01	0.01	0.01	0.01	0.01
Total	3.01	3.00	3.00	3.01	3.00	3.00	3.00	2.99

Table 10. Major-element mineral chemistry of clinopyroxene from Lens A dunitic rocks.

Sample	208279									208282
EPMA Point	9	28	31	58	61	62	63	70	79	5
SiO_2	54.76	55.13	53.44	54.86	52.57	54.50	55.15	54.63	54.39	53.99
TiO_2	0.01	0.00	0.01	0.00	0.00	0.00	0.00	0.01	0.00	0.00
Al_2O_3	0.10	0.00	0.18	0.14	0.01	0.01	0.01	0.10	0.18	0.00
Cr_2O_3	0.18	0.06	0.62	0.16	0.38	0.11	0.22	0.71	0.08	0.02
FeO*	1.17	1.09	2.45	1.11	1.94	1.11	1.08	1.58	1.36	1.47
MnO	0.03	0.01	0.06	0.03	0.00	0.02	0.01	0.00	0.05	0.03
MgO	19.27	18.35	20.37	18.49	19.43	18.19	17.84	17.88	19.65	19.56
CaO	23.52	24.90	23.10	24.23	22.88	24.97	25.02	24.69	23.93	24.06
Na_2O	0.07	0.03	0.10	0.13	0.05	0.08	0.11	0.08	0.00	0.04
K_2O	0.00	0.01	0.00	0.00	0.00	0.00	0.00	0.00	0.00	0.00
NiO	0.08	0.06	0.06	0.06	0.08	0.05	0.06	0.06	0.06	0.07
Total	99.19	99.63	100.39	99.20	97.33	99.03	99.48	99.74	99.69	99.25
Mg#	0.97	0.97	0.94	0.97	0.95	0.97	0.97	0.95	0.96	0.96
O=?	6.00	6.00	6.00	6.00	6.00	6.00	6.00	6.00	6.00	7.00
Si	1.99	2.00	1.94	2.00	1.96	1.99	2.01	1.99	1.97	2.30
Ti	0.00	0.00	0.00	0.00	0.00	0.00	0.00	0.00	0.00	0.00
Al	0.00	0.00	0.01	0.01	0.00	0.00	0.00	0.00	0.01	0.00
Cr	0.01	0.00	0.02	0.00	0.01	0.00	0.01	0.02	0.00	0.00
Fe*	0.04	0.03	0.07	0.03	0.06	0.03	0.03	0.05	0.04	0.05
Mn	0.00	0.00	0.00	0.00	0.00	0.00	0.00	0.00	0.00	0.00
Mg	1.04	0.99	1.10	1.00	1.08	0.99	0.97	0.97	1.06	1.24
Ca	0.92	0.97	0.90	0.94	0.91	0.98	0.97	0.96	0.93	1.10
Na	0.00	0.00	0.01	0.01	0.00	0.01	0.01	0.01	0.00	0.00
K	0.00	0.00	0.00	0.00	0.00	0.00	0.00	0.00	0.00	0.00
Ni	0.00	0.00	0.00	0.00	0.00	0.00	0.00	0.00	0.00	0.00
Total	4.01	4.00	4.05	4.00	4.03	4.01	4.00	4.00	4.02	4.70
Cr#	0.55	0.97	0.70	0.43	0.96	0.84	0.95	0.83	0.24	1.00
Wo	45.88	48.56	43.27	47.66	44.50	48.82	49.37	48.61	45.71	45.87
En	52.28	49.76	53.06	50.59	52.55	49.47	48.95	48.96	52.19	51.89
Fs	1.84	1.68	3.67	1.75	2.95	1.71	1.68	2.43	2.10	2.24

Table 11. Whole-rock major-element geochemistry (anhydrous) of Lens B samples determined by XRF.

Sample name	Rock type	SiO_2	TiO_2	Al_2O_3	Fe_2O_3	MnO	MgO	CaO	Na_2O	K_2O	P_2O_5	LOI	Total
		wt%	wt%	wt%	wt%	wt%	wt%	wt%	wt%	wt%	wt%	wt%	wt%
194905	mdun	41.95	0.04	0.69	7.50	0.16	49.57	0.06	0.02	0.00	0.01	8.01	100.00
194906	mdun	42.77	0.05	1.06	9.46	0.08	46.47	0.07	0.03	0.00	0.01	10.94	100.00
194903	mdun	41.33	0.04	0.63	7.75	0.15	49.99	0.06	0.03	0.00	0.01	9.06	100.00
194907	mdun	42.19	0.10	1.59	11.00	0.10	44.87	0.09	0.05	0.00	0.02	12.18	100.00
194902	mdun	40.42	0.04	0.56	10.03	0.14	48.70	0.07	0.03	0.00	0.01	8.60	100.00
194901	mdun	40.89	0.04	0.61	9.50	0.14	48.72	0.07	0.02	0.00	0.01	8.90	100.00
194904	mdun	40.66	0.04	0.58	10.13	0.14	48.34	0.07	0.03	0.00	0.01	9.55	100.00
194896B	serp	44.49	0.05	0.76	4.56	0.06	49.98	0.06	0.03	0.00	0.01	12.36	100.00
194897	serp	43.25	0.05	0.68	10.89	0.04	44.99	0.06	0.03	0.00	0.01	13.05	100.00
194900B	serp	43.20	0.05	0.78	9.39	0.04	46.45	0.06	0.02	0.00	0.01	13.04	100.00
194898A	serp	43.90	0.14	1.54	10.55	0.07	43.57	0.19	0.03	0.00	0.02	12.51	100.00
194899	serp	43.34	0.10	1.42	18.51	0.14	35.20	1.26	0.03	0.00	0.01	11.34	100
194910B-a	carb	45.63	0.04	1.52	13.75	0.04	38.92	0.06	0.03	0.00	0.00	12.41	100
194910B-b	carb	45.15	0.04	1.37	13.21	0.06	40.07	0.07	0.03	0.00	0.00	12.74	100

Table 12. Whole-rock trace-element geochemistry of Lens B samples determined by XRF.

Sample name		V	Cr	Co	Ni	Cu	Zn	Rb	Y	Ba	Pb	Ce	Th
		ppm	ppm	ppm	ppm	ppm	ppm	ppm	ppm	ppm	ppm	ppm	ppm
194905	mdun	21.09	961.11	110.90	3428.60	5.24	46.43	2.34		6.10	3.53	2.71	
194906	mdun	31.94	4522.38	90.40	2588.55	7.73	54.74	2.32	2.42	8.04	2.22		0.40
194903	mdun	19.29	1048.85	111.74	3820.43	3.30	46.53	2.36	2.74	14.63	2.47	1.36	0.17
194907	mdun	42.76	5704.53	92.54	2219.68	7.10	81.99	2.36	4.89	7.49	2.77		0.50
194902	mdun	20.50	954.91	114.97	3512.75	2.88	43.06	2.07	2.87	8.10	2.16	3.33	0.32
194901	mdun	22.26	1201.48	124.37	3708.94	2.29	46.18	1.95	3.10	10.65	1.65	1.17	0.04
194904	mdun	23.75	2457.28	130.04	3226.95	4.29	53.84	2.61	2.25	12.08	4.54		
194896B	serp	21.42	1183.49	77.27	2840.51	5.00	34.63	2.10	2.95	7.27	0.90	0.37	0.16
194897	serp	23.25	1100.46	102.30	2857.38	4.33	33.62	1.97	2.51	6.51	0.82	1.77	0.41
194900B	serp	21.12	897.49	105.22	3135.51	2.90	39.92	2.13	2.92	6.46	1.92	0.90	0.57
194898A	serp	46.25	900.18	97.36	3193.59	0.88	54.55	1.60	2.83	5.66	1.97	3.33	0.81
194899	serp	51.69	4955.54	126.84	1933.20	102.57	63.17	1.91	3.06	9.79	1.13	28.80	0.20
194910B-a	carb	38.07	1457.94	113.06	2785.72		77.30	1.44	2.35	10.47	0.78	0.46	0.13
194910B-b	carb	32.67	1287.24	110.28	2475.60		74.67	1.60	2.54	8.28	0.69	3.38	0.15

mdun-metadunites

serp-seprentinites

carb-near carbonate margin